

<sup>1</sup> SEARCH FOR EXOTIC HIGGS DECAYS TO LIGHT  
<sup>2</sup> NEUTRAL SCALARS IN FINAL STATES WITH  
<sup>3</sup> BOTTOM QUARKS AND TAU LEPTONS

<sup>4</sup> KA YU STEPHANIE KWAN

<sup>5</sup> A DISSERTATION  
<sup>6</sup> PRESENTED TO THE FACULTY  
<sup>7</sup> OF PRINCETON UNIVERSITY  
<sup>8</sup> IN CANDIDACY FOR THE DEGREE  
<sup>9</sup> OF DOCTOR OF PHILOSOPHY

<sup>10</sup> NOT YET RECOMMENDED FOR ACCEPTANCE  
<sup>11</sup> BY THE DEPARTMENT OF PHYSICS  
<sup>12</sup> ADVISER: ISOBEL OJALVO

<sup>13</sup> MAY 2024

<sup>14</sup>

© Copyright by Ka Yu Stephanie Kwan, 2024.

<sup>15</sup>

All Rights Reserved

## Abstract

Open questions in particle physics may be addressed by the existence of an extended Higgs sector beyond the Standard Model Higgs boson with mass 125 GeV, which was discovered in 2012 at the Large Hadron Collider (LHC) by the CMS and ATLAS experiments. Many properties of a potential extended Higgs sector remain unconstrained by current measurements, making direct searches of exotic Higgs decays a powerful probe of new physics. The decay of the 125 GeV Higgs boson into two light neutral scalar particles ( $h \rightarrow aa$ ) is allowed in extensions of the Standard Model, such as Two Higgs Doublet Models extended with a scalar singlet (2HDM+S). We present a search at CMS for exotic decays of the 125 GeV Higgs boson to two light neutral scalars, which decay to two bottom quarks and two tau leptons ( $h \rightarrow aa \rightarrow bb\tau\tau$ ). This analysis is combined with a different search where the light scalars decay to two bottom quarks and two muons. The results from the  $bb\tau\tau$  analysis and the combined analyses are interpreted in 2HDM+S scenarios. In a different extension of the Standard Model, the Two Real Singlet Model (TRSM), the 125 GeV Higgs boson can decay to two light scalars with unequal mass ( $h \rightarrow a_1a_2$ ). This decay has not been searched for to date at CMS. We present ongoing work on a search for  $h \rightarrow a_1a_2$ , where the  $a_2$  decays into two  $a_1$ , resulting in four bottom quarks and two tau leptons in the final state, in the  $\mu\tau_h$  channel of the  $\tau\tau$  decay. Such searches for rare processes will directly benefit from the increased datasets that will be generated by the High-Luminosity LHC (HL-LHC), which is scheduled to increase the LHC's number of simultaneous proton-proton collisions by a factor of five to seven. To contribute to the performance of the CMS Level-1 Trigger in selecting collisions with interesting physics, this thesis presents an upgraded algorithm for reconstructing electrons and photons in the barrel calorimeter, which will use information with higher spatial granularity to distinguish genuine electrons and photons from background.

<sup>42</sup>

## Acknowledgements

<sup>43</sup> Placeholder acknowledgements.



# <sup>45</sup> Contents

<sup>46</sup>	Abstract . . . . .	iii
<sup>47</sup>	Acknowledgements . . . . .	iv
<sup>48</sup>	List of Tables . . . . .	xi
<sup>49</sup>	List of Figures . . . . .	xiii
<sup>50</sup>	<b>1 Introduction</b>	<b>1</b>
<sup>51</sup>	1.1 History of the Standard Model . . . . .	1
<sup>52</sup>	1.2 The Standard Model as a gauge theory . . . . .	3
<sup>53</sup>	1.3 The Higgs Mechanism . . . . .	6
<sup>54</sup>	1.4 Two-Higgs Doublet Models . . . . .	8
<sup>55</sup>	1.5 Two Real Singlet Model . . . . .	11
<sup>56</sup>	<b>2 The Large Hadron Collider and the CMS Experiment</b>	<b>15</b>
<sup>57</sup>	2.1 The Large Hadron Collider . . . . .	16
<sup>58</sup>	2.2 Luminosity and pile-up . . . . .	17
<sup>59</sup>	2.3 The High-Luminosity LHC . . . . .	20
<sup>60</sup>	2.4 The CMS Detector . . . . .	21
<sup>61</sup>	2.5 Sub-detectors of CMS . . . . .	23
<sup>62</sup>	2.5.1 Inner tracking system . . . . .	23
<sup>63</sup>	2.5.2 ECAL . . . . .	24
<sup>64</sup>	2.5.3 HCAL . . . . .	25

65	2.5.4 Muon detectors . . . . .	27
66	2.5.5 The Level-1 Trigger . . . . .	28
67	2.5.6 The High-Level Trigger . . . . .	32
68	2.5.7 Particle reconstruction . . . . .	33
69	2.5.8 Data storage and computational infrastructure . . . . .	33
70	<b>3 The Phase-2 Upgrade of CMS</b>	<b>35</b>
71	3.1 The High-Luminosity LHC . . . . .	35
72	3.2 The Phase-2 Level-1 Trigger . . . . .	36
73	3.3 Standalone Barrel Calorimeter electron/photon reconstruction . . . . .	39
74	3.3.1 Electron/photon standalone barrel procedure . . . . .	39
75	3.3.2 Electron/photon standalone barrel results . . . . .	44
76	<b>4 Datasets and Monte Carlo samples</b>	<b>48</b>
77	4.1 Datasets used . . . . .	48
78	4.2 Monte Carlo samples . . . . .	49
79	4.3 Embedded samples . . . . .	50
80	<b>5 Object reconstruction and corrections applied</b>	<b>53</b>
81	5.1 Object reconstruction . . . . .	54
82	5.1.1 Taus . . . . .	54
83	5.1.2 Muons . . . . .	57
84	5.1.3 Electrons . . . . .	58
85	5.1.4 Jets . . . . .	60
86	5.1.5 B-flavored jets . . . . .	61
87	5.2 Reconstruction of the $\tau\tau$ mass . . . . .	62
88	5.2.1 Original SVFit “standalone”: maximum likelihood . . . . .	63
89	5.2.2 “Classic SVFit” with matrix element . . . . .	64
90	5.2.3 FastMTT: optimized SVFit . . . . .	64

91	5.3 Corrections applied to simulation . . . . .	65
92	5.3.1 Tau energy scale . . . . .	66
93	5.3.2 Muon energy scale . . . . .	67
94	5.3.3 Electron energy scale . . . . .	67
95	5.3.4 $\tau_h$ identification efficiency . . . . .	67
96	5.3.5 Trigger efficiencies . . . . .	68
97	5.3.6 Tau trigger efficiencies . . . . .	69
98	5.3.7 Single muon trigger efficiencies . . . . .	70
99	5.3.8 Single electron trigger efficiencies . . . . .	71
100	5.3.9 $e\mu$ cross-trigger efficiencies . . . . .	72
101	5.3.10 Electrons and muons faking $\tau_h$ : energy scales . . . . .	73
102	5.3.11 Electrons and muons faking $\tau_h$ : misidentification efficiencies .	74
103	5.3.12 Electron ID and tracking efficiency . . . . .	75
104	5.3.13 Muon ID, isolation, and tracking efficiencies . . . . .	75
105	5.3.14 Recoil corrections . . . . .	77
106	5.3.15 Drell-Yan corrections . . . . .	78
107	5.3.16 Pile-up reweighing . . . . .	78
108	5.3.17 Pre-firing corrections . . . . .	79
109	5.3.18 Top $p_T$ spectrum reweighing . . . . .	79
110	5.3.19 B-tagging efficiency . . . . .	79
111	5.3.20 Jet energy resolution and jet energy smearing . . . . .	80
112	<b>6 Event selection</b>	<b>81</b>
113	6.1 General procedure for all channels . . . . .	81
114	6.2 Event selection in the $\mu\tau_h$ channel . . . . .	83
115	6.3 Event selection in the $e\tau_h$ channel . . . . .	85
116	6.4 Event selection in the $e\mu$ channel . . . . .	87
117	6.5 Extra lepton vetoes in all channels . . . . .	88

118	<b>7 Background estimation</b>	<b>91</b>
119	7.1 Z+jets . . . . .	91
120	7.2 W+jets . . . . .	92
121	7.3 $t\bar{t}$ + jets . . . . .	92
122	7.4 Single top . . . . .	93
123	7.5 Diboson . . . . .	93
124	7.6 Standard Model Higgs . . . . .	93
125	7.7 Jet faking $\tau_h$ . . . . .	94
126	7.8 QCD multijet background . . . . .	95
127	<b>8 Systematic uncertainties</b>	<b>97</b>
128	8.1 Uncertainties in the lepton energy scales . . . . .	98
129	8.2 Uncertainties from other lepton corrections . . . . .	99
130	8.3 Uncertainties from jet energy scale and resolution . . . . .	100
131	8.4 Uncertainties from b-tagging scale factors . . . . .	101
132	8.5 Uncertainties from MET . . . . .	101
133	8.6 Uncertainties associated with samples used . . . . .	101
134	8.7 Other uncertainties . . . . .	102
135	8.8 Pulls and impacts . . . . .	103
136	<b>9 Event categorization and signal extraction</b>	<b>105</b>
137	9.1 B-tag jet multiplicity . . . . .	105
138	9.2 DNN-based event categorization . . . . .	106
139	9.3 Methodology for signal extraction . . . . .	108
140	9.3.1 Model building and parameter estimation . . . . .	109
141	9.3.2 Hypothesis testing . . . . .	111
142	9.3.3 Confidence intervals . . . . .	112
143	9.3.4 Profile likelihood ratio . . . . .	113

<sup>144</sup>	9.3.5 Modified frequentist method: $CL_S$	115
<sup>145</sup>	<b>10 Results</b>	<b>116</b>
<sup>146</sup>	10.1 Results from $bb\tau\tau$	116
<sup>147</sup>	10.2 Combination with $bb\mu\mu$ final state	118
<sup>148</sup>	<b>11 Asymmetric exotic Higgs decays</b>	<b>129</b>
<sup>149</sup>	11.1 Signal masses	129
<sup>150</sup>	11.2 Cascade scenario signal studies	130
<sup>151</sup>	11.3 Current control plots for $\mu\tau_h$ channel	132
<sup>152</sup>	<b>12 Conclusion and outlook</b>	<b>136</b>

# <sup>153</sup> List of Tables

<sup>154</sup>	4.1	Expected event composition after selecting two muons in the embedded technique, before additional cuts (i.e. inclusive), and after adding a requirement on the di-muon mass $m_{\mu\mu} > 70$ GeV, or a requirement on the number of b-tag jets in the event. . . . .	52
<sup>155</sup>			
<sup>156</sup>			
<sup>157</sup>			
<sup>158</sup>	5.1	Energy scales applied to genuine hadronic tau decays $\tau_h$ by data-taking year/era and decay mode, along with systematic errors. . . . .	66
<sup>159</sup>			
<sup>160</sup>	5.2	Energy scales and systematic errors applied to genuine muons. . . . .	67
<sup>161</sup>			
<sup>162</sup>	5.3	Energy scales and systematic errors applied to electrons in embedded samples by data-taking year/era. . . . .	67
<sup>163</sup>			
<sup>164</sup>	5.4	Tau ID efficiency for the DeepTau vs. jet medium working point, with central, up, and down values for 2018, binned in the tau $p_T$ . . . . .	68
<sup>165</sup>			
<sup>166</sup>	5.5	Energy scales and up/down systematic uncertainties applied to electrons misidentified as hadronic taus. . . . .	73
<sup>167</sup>			
<sup>168</sup>	5.6	Tau mis-identification efficiency for the DeepTau Tight and Very Loose (VLoose) working points vs. muons in 2018. . . . .	74
<sup>169</sup>			
<sup>170</sup>	5.7	Tau mis-identification efficiency for the DeepTau Tight and Very Loose (VLoose) working points vs. electrons in 2018. . . . .	74

171	6.1	Trigger thresholds used for the leptons in the $bb\mu\mu$ analysis and the 172 $bb\tau\tau$ analysis (the focus of this work). The thresholds for the three $bb\tau\tau$ 173           channels ( $e\mu$ , $e\tau_h$ , and $\mu\tau_h$ ) are listed separately, with some channels 174           and years taking the logical OR of two triggers with different thresholds. . . . .	83
175	6.2	Summary of requirements applied to the leptons in the $bb\mu\mu$ analysis 176           and the $bb\tau\tau$ analysis (the focus of this work). $\Delta R = \sqrt{(\Delta\eta)^2 + (\Delta\phi)^2}$ 177           is a measure of spatial separation. Relative isolation is defined in 178           Eqn. 5.2Muonsequation.5.1.2 and Section 5.1.2Muonssubsection.5.1.2. 179           The b-tag jets are required to pass the listed DeepFlavour working 180           points (WP), which are described in Section 5.1.5B-flavored jetssub- 181           section.5.1.5. In the $bb\tau\tau$ analysis, the required $ \eta $ of the hadronic 182           taus are listed for the single and cross triggers respectively. The $bb\mu\mu$ 183           analysis requires two b-tag jets in all events, while the $bb\tau\tau$ analysis 184           only requires one. . . . .	84
185	6.3	High-Level Trigger (HLT) paths used to select data and simulation 186           events in 2016 for the three $\tau\tau$ channels. . . . .	88
187	6.4	High-Level Trigger (HLT) paths used to select data and simulation 188           events in 2017 for the three $\tau\tau$ channels. . . . .	89
189	6.5	High-Level Trigger (HLT) paths used to select data and simulation 190           events in 2018 for the three $\tau\tau$ channels. In 2018 a HLT trigger path 191           using the hadron plus strips (HPS) tau reconstruction algorithm be- 192           came available. . . . .	90
193	9.1	Event categorization based on DNN scores for events with exactly 1 194           b-tag jet (1bNN), for the three $\tau\tau$ channels and three eras. . . . .	108
195	9.2	Event categorization based on DNN scores for events with 2 b-tag jets 196           (2bNN), for the three $\tau\tau$ channels and three eras. . . . .	109

# <sup>197</sup> List of Figures

<sup>198</sup> 1.1	Table of Standard Model particles showing the grouping of the fermions into three generations of matter and the bosons, responsible for carrying the three fundamental forces in the Standard Model. The masses, charges, and spins of the particles are shown. The antimatter counter- parts of the fermions are not shown. The possible interactions between the fermions and gauge bosons are highlighted. . . . .	3
<sup>204</sup> 1.2	An illustration of the Higgs potential. . . . .	8
<sup>205</sup> 1.3	Branching ratios of a singlet-like pseudoscalar in Type II 2HDM+S for $\tan \beta = 0.5$ (left) and $\tan \beta = 5$ (right). . . . .	11
<sup>207</sup> 1.4	Benchmark plane BP1 for benchmark scenario 1, for the decay signa- ture $h_{125} \rightarrow h_1 h_2$ with $h_{125} \equiv h_3$ , defined in the $(M_1, M_2)$ plane. . . .	14
<sup>209</sup> 2.1	Aerial view of the Large Hadron Collider (LHC). . . . .	18
<sup>210</sup> 2.2	Distribution of the mean number of inelastic collisions per bunch cross- ing (pile-up) in data, for proton-proton collisions in 2016-2018 . . .	20
<sup>212</sup> 2.3	Sketch of particle trajectories of muons, electrons, charged and neutral hadrons, and photons in a transverse cross-section of the CMS detector.	22
<sup>214</sup> 2.4	Cross section of the current Phase-1 CMS tracker. . . . .	24
<sup>215</sup> 2.5	Longitudinal view of the CMS detector showing the hadron calorimeter barrel (HB), endcap (HE), outer (HO), and forward (HF) calorimeters.	26

217	2.6	Layout of the CMS barrel muon drift tube (DT) chambers in one of the five wheels. . . . .	28
219	2.7	Dataflow for the Phase-1 Level-1 Trigger. . . . .	29
220	2.8	Schematic of the calorimeter trigger after Long Shutdown 2. The Layer-1 calorimeter trigger is implemented in CTP7 cards, which send time-multiplexed outputs to the Layer-2 MP7 cards. The Layer-2 cards handle the data in a round-robin style and the outputs are de- multiplexed, producing one output data stream to the Global Trigger.	31
224			
225	3.1	Functional diagram of the CMS L1 Phase-2 upgraded trigger design. .	37
226	3.2	Summary of the links between the trigger primitives, the trigger ob- jects, the Level-1 algorithms, and the physics channels in the Phase-2 menu. . . . .	40
227			
229	3.3	Schematic of the geometry of the Phase-2 ECAL barrel in the Regional Calorimeter Trigger (RCT), showing the division of the barrel region into 36 Regional Calorimeter Trigger (RCT) cards ( <i>red</i> ). Each card spans $17 \times 4$ towers in $\eta \times \phi$ ( <i>green</i> ), and each tower is $5 \times 5$ in single crystals in $\eta \times \phi$ . Towers in the overlap region ( <i>shaded yellow</i> ) are read out to both the barrel and endcap. . . . .	41
231			
232			
234			
235	3.4	Schematic of two example RCT cards in the negative eta ( <i>top left</i> ) and positive eta ( <i>bottom left</i> ) regions of the ECAL barrel. Each RCT card is divided into six regions: five regions are of size $3 \times 4$ towers in $\eta \times \phi$ ( <i>top right</i> ), and a sixth smaller overlap region of size $2 \times 4$ towers ( <i>bottom right</i> ). Each tower is $5 \times 5$ ( $\eta \times \phi$ ) in crystals. . . . .	42
236			
237			
238			
239			



261	3.7	Efficiencies of the current and previous emulators of the standalone barrel $e/\gamma$ algorithm for the Phase-2 Level-1 Trigger, evaluated in a simulated sample containing electrons, as a function of the electron’s generator-level transverse momentum $p_T$ . The standalone working point (WP) is defined as the logical OR of the isolation flag and shower shape flag. The efficiencies with and without requiring the standalone WP, are shown for the current emulator (labeled “Phase 2”, <i>black, red</i> ) and the previous emulator (labeled “TDR”, <i>dark blue, grey</i> ). . . . .	45
269	3.8	Rates in kHz of the current Phase-2 and previous (“TDR”) emulators of the standalone barrel $e/\gamma$ algorithm for the Phase-2 Level-1 Trigger, evaluated on a minimum bias (MinBias) sample with 200 pile-up (PU), measured as a function of the minimum energy ( $E_T$ ) required of the reconstructed $e/\gamma$ object in each event. The standalone working point (standalone WP) is defined to be the logical OR of the isolation flag and the shower shape flag. The rates with and without requiring the standalone WP, are shown for the current emulator (labeled “Phase 2”, <i>black, red</i> ) and the previous emulator (labeled “TDR”, <i>dark blue,</i> <i>grey</i> ). . . . .	47
279	4.1	Cumulative delivered and recorded luminosity versus time for 2015- 2018 at CMS, in proton-proton collision data only, at nominal center- of-mass energy. . . . .	49
282	4.2	Schematic view of the four main steps of the embedding technique for $\tau$ leptons. . . . .	51
284	5.1	Distributions of $m_{\tau\tau}$ reconstructed by the classic SVFit algorithm, and masses of visible tau decay products (before SVFit). . . . .	65
286	5.2	Electron/photon energy scale factors and uncertainties for 2018. . . .	68

287	5.3 Hadronic tau leg efficiency of the cross-triggers for $\mu\tau_h$ ( <i>left</i> ) and $e\tau_h$ ( <i>right</i> ) triggers as a function of offline tau $p_T$ for 2016, 2017, and 2018.	70
288		
289	5.4 Trigger efficiencies in data ( <i>top panels</i> ) and ratio of efficiencies af- ter/before a HLT muon reconstruction update ( <i>bottom panels</i> ) for the muon in the isolated single muon trigger with threshold $p_T > 24$ GeV in the data-taking year 2018, as functions of the muon $p_T$ ( <i>left</i> ) and muon $ \eta $ ( <i>right</i> ). . . . .	71
290		
291		
292		
293		
294	5.5 Trigger efficiencies in data and the data/MC ratio for the electron in the single electron trigger with threshold $p_T > 32$ GeV in the data- taking year 2018, as functions of the electron $p_T$ ( <i>left</i> ) and electron $ \eta $ ( <i>right</i> ). . . . .	72
295		
296		
297		
298	5.6 Efficiencies of the electron leg vs. $p_T$ ( <i>left</i> ) and the muon log vs. $\eta$ ( <i>right</i> ), for the HLT path with online thresholds of 12 GeV for the electron and 23 GeV for the muon, with the data-taking years 2016 through 2018 overlaid. . . . .	73
299		
300		
301		
302	5.7 Efficiencies in data ( <i>top panels</i> ) and the ratio of efficiencies in data/MC ( <i>bottom panels</i> ), for the electron multivariate analysis (MVA) identifi- cation ( <i>left</i> ) and for the Gaussian-sum filter (GSF) tracking ( <i>right</i> ). . .	75
303		
304		
305	5.8 Muon identification efficiencies in 2015 data and MC as a function of the muon $p_T$ for the loose ID ( <i>left</i> ) and tight ID ( <i>right</i> ) working points.	76
306		
307	5.9 Muon isolation efficiencies in Run-2 data as a function of the muon $p_T$ ( <i>left</i> ) and $ \eta $ ( <i>right</i> ). . . . .	77
308		
309	5.10 Muon tracking efficiencies as a function of $ \eta $ for standalone muons in Run-2 data ( <i>black</i> ) and Drell-Yan ( <i>blue</i> ) MC simulation. . . . .	78
310		
311	7.1 Leading-order Feynman diagrams of Higgs production. . . . .	94

312	8.1 Top sixty pulls and impacts for the combination of all channels and	
313	years. . . . .	104
314	9.1 Schematic of the Neyman construction for confidence intervals. . . . .	114
315	10.1 Postfit final observed and expected $m_{\tau\tau}$ distributions in the $\mu\tau_h$ chan-	
316	nel, for the 1 b-tag jet and 2 b-tag jet signal and control regions. . . . .	120
317	10.2 Postfit final observed and expected $m_{\tau\tau}$ distributions in the $e\tau_h$ chan-	
318	nel, for the 1 b-tag jet and 2 b-tag jet signal and control regions. . . . .	121
319	10.3 Postfit final observed and expected $m_{\tau\tau}$ distributions in the $e\mu$ channel.	122
320	10.4 Observed 95% CL exclusion limits ( <i>black, solid lines</i> ) and expected 95%	
321	CL and 68% CL limits ( <i>shaded yellow and green</i> ) on the branching	
322	fraction $B(h \rightarrow aa \rightarrow bb\tau\tau)$ in percentages, assuming the Standard	
323	Model production for the 125 GeV Higgs ( $h$ ). Limits are shown for the	
324	$\mu\tau_h$ channel ( <i>top left</i> ), the $e\tau_h$ channel ( <i>top right</i> ), and the $e\mu$ channel	
325	( <i>bottom left</i> ), and lastly the combination of all three channels ( <i>bottom</i>	
326	<i>right</i> ) The dataset corresponds to $138 \text{ fb}^{-1}$ of data collected in the	
327	years 2016-2018 at a center-of-mass energy 13 TeV. . . . .	123
328	10.5 Observed 95% CL upper limits on $B(h \rightarrow aa)$ in %, for the $bb\tau\tau$ final	
329	state ( <i>left</i> ) and $bb\mu\mu$ final state ( <i>right</i> ) using the full Run 2 integrated	
330	luminosity of $138 \text{ fb}^{-1}$ in 2HDM+S type I ( <i>blue</i> ), type II with $\tan\beta =$	
331	$2.0$ ( <i>orange dashed</i> ), type III with $\tan\beta = 2.0$ ( <i>dotted green</i> ), and type	
332	IV with $\tan\beta = 0.6$ ( <i>red dashed</i> ). . . . .	124

333	10.6 Observed 95% CL upper limits on the branching fraction of the 125	
334	GeV Higgs boson to two pseudoscalars, $B(h \rightarrow aa)$ , in percentages,	
335	as a function of the pseudoscalar mass $m_a$ , in 2HDM+S type I ( <i>blue</i> ),	
336	type II with $\tan\beta = 2.0$ ( <i>orange dashed</i> ), type III with $\tan\beta = 2.0$	
337	( <i>dotted green</i> ), and type IV with $\tan\beta = 0.6$ ( <i>red dashed</i> ), for the	
338	combination of $bb\mu\mu$ and $bb\tau\tau$ channels using the full Run 2 integrated	
339	luminosity of $138 \text{ fb}^{-1}$ . . . . .	125
340	10.7 Observed 95% CL upper limits on $\mathcal{B}(h \rightarrow aa)$ in %, for the combination	
341	of $bb\mu\mu$ and $bb\tau\tau$ channels using the full Run 2 integrated luminosity	
342	of $138 \text{ fb}^{-1}$ for Type II ( <i>left</i> ), Type III ( <i>middle</i> ), and Type IV ( <i>right</i> )	
343	2HDM+S in the $\tan\beta$ vs. $m_a$ phase space. . . . .	126
344	10.8 Summary plot of current observed and expected 95% CL limits on the	
345	branching ratio of the 125 GeV Higgs boson to two pseudoscalars, nor-	
346	malized to the Standard Model Higgs production cross-section, $\frac{\sigma(h)}{\sigma_{\text{SM}}} \times$	
347	$B(h \rightarrow aa)$ , in the 2HDM+S type I scenario, obtained at CMS with	
348	data collected at 13 TeV. . . . .	126
349	10.9 Summary plot of current observed and expected 95% CL limits on the	
350	branching ratio of the 125 GeV Higgs boson to two pseudoscalars, nor-	
351	malized to the Standard Model Higgs production cross-section, $\frac{\sigma(h)}{\sigma_{\text{SM}}} \times$	
352	$B(h \rightarrow aa)$ , in the 2HDM+S type II scenario with $\tan\beta = 2.0$ , ob-	
353	tained at CMS with data collected at 13 TeV. . . . .	127
354	10.10 Summary plot of current observed and expected 95% CL limits on the	
355	branching ratio of the 125 GeV Higgs boson to two pseudoscalars, nor-	
356	malized to the Standard Model Higgs production cross-section, $\frac{\sigma(h)}{\sigma_{\text{SM}}} \times$	
357	$B(h \rightarrow aa)$ , in the 2HDM+S type III scenario with $\tan\beta = 2.0$ , ob-	
358	tained at CMS with data collected at 13 TeV. . . . .	128

359	11.1 Generator-level b-flavor jet transverse momenta $p_T$ , for $h \rightarrow a_1 a_2$ cas-	
360	cade scenario in the $4b2\tau$ final state, for mass hypotheses $(m_{a_1}, m_{a_2}) =$	
361	$(100, 15)$ GeV ( <i>left</i> ) and $(40, 20)$ GeV ( <i>right</i> ). In each plot the generator-	
362	level $p_T$ of the leading ( <i>black</i> ), sub-leading ( <i>red</i> ), third ( <i>blue</i> ), and	
363	fourth ( <i>light green</i> ) are overlaid. . . . .	131
364	11.2 Distributions (arbitrary units) of transverse momentum $p_T$ resolution	
365	and $\Delta R$ between the two closest generator-level $b$ jets, treated as one	
366	object, and the nearest reconstructed AK4 jet, for two different $h \rightarrow$	
367	$a_1 a_2$ mass hypotheses $(m_{a_1}, m_{a_2}) = (100, 15)$ GeV ( <i>top left, top right</i> )	
368	and $(40, 20)$ GeV ( <i>bottom left, bottom right</i> ) in the ggH production of	
369	the 125 GeV $h$ . In the $(40, 20)$ GeV mass point, the longer $p_T$ resolution	
370	tail ( <i>bottom left</i> ) indicates that the reconstructed jet underestimates	
371	the generator b-flavor jets' energy, and the significant fraction of events	
372	with larger $\Delta R$ values ( <i>bottom right</i> ) indicate worse matching. . . . .	132
373	11.3 Kinematic properties of the leading muon and $\tau_h$ in the $\mu\tau_h$ channel: $p_T$	
374	( <i>top row</i> ), $\eta$ ( <i>second row</i> ), and $\phi$ ( <i>third row</i> ). The visible 4-momenta	
375	of the muon and $\tau_h$ are summed, giving the visible di-tau mass $m_{\text{vis}}$	
376	and transverse momentum $p_{T,\text{vis}}$ . The errors shown in the figures only	
377	include statistical errors and only several of the full set of systematic	
378	errors (only those associated with the lepton energy scales and $\tau_h$ iden-	
379	tification efficiency). . . . .	134
380	11.4 Kinematic properties of the leading and sub-leading b-tag jets in the	
381	$\mu\tau_h$ final state: jet $p_T$ ( <i>top row</i> ), $\eta$ ( <i>second row</i> ), $\phi$ ( <i>third row</i> ), as well	
382	as the missing transverse energy magnitude and azimuthal direction	
383	( <i>bottom row</i> ). The errors shown in the figures only include statistical	
384	errors and only several of the full set of systematic errors (only those	
385	associated with the lepton energy scales and $\tau_h$ identification efficiency).	135

# <sup>386</sup> Chapter 1

## <sup>387</sup> Introduction

<sup>388</sup> The Standard Model is the current prevailing theoretical framework that encompasses  
<sup>389</sup> all known elementary particles to date and describes their interactions, yet falls short  
<sup>390</sup> of describing open problems in physics. Here, we describe the history of the Standard  
<sup>391</sup> Model and its particle content (Section 1.1), and provide a mathematical motivation of  
<sup>392</sup> the SM as a gauge theory (Section 1.2). We introduce the Higgs mechanism (Section  
<sup>393</sup> 1.3), and outline two groups of theoretical extensions to the Standard Model that  
<sup>394</sup> feature extended Higgs sectors (Sections 1.4 and 1.5).

### <sup>395</sup> 1.1 History of the Standard Model

<sup>396</sup> The building blocks of our modern-day understanding of particle physics were estab-  
<sup>397</sup> lished over the course of many decades by experimental discoveries and theoretical  
<sup>398</sup> advances, culminating in the development of a theoretical framework known as the  
<sup>399</sup> Standard Model (SM). In the 1880s, the electron was the first subatomic particle to  
<sup>400</sup> be identified, through measurements of particles produced by ionizing gas. By the  
<sup>401</sup> 1930s, atoms were known to consist mostly of empty space, with protons and neutrons  
<sup>402</sup> concentrated at the center and orbited by electrons. Spurred by advances in parti-  
<sup>403</sup> cle accelerator technology, the experimental discoveries of the positron, the muon,

and the pion, painted an increasingly complicated picture of particle physics that could not be described solely with atomic physics [1]. Quantum field theory (QFT) began to be developed in the early 20th century as an extension of the conceptual framework of quantum mechanics to electromagnetic fields [2]. In 1927, Dirac coined the name quantum electrodynamics (QED), which was the first part of QFT that was developed. QED quantized the electromagnetic field and supplied a relativistic theory of the electron, and could be applied to concrete physical processes such as the scattering of high-frequency photons by free electrons (Compton scattering), and the production of electron-positron pairs by photons [2]. In the 1940s the QED-only picture was challenged by the realization that the four-fermion theory of weak interactions had infinities at higher orders of perturbation theory which could not be removed via the technique of renormalization [3], i.e. shifting divergences into parts of the theory that do not influence empirical measurements [2].

In the 1950s and 1960s, QFT was extended to describe not only the electromagnetic force, but also the strong and weak force, with the final picture forming the Standard Model. This took place in the development and maturation of three principles: the quark model, the idea of gauge (or local) symmetry, and spontaneously broken symmetry [3]. In the fully fledged QFT, Lagrangians had to be formed that contained new classes of quantum fields, or particles [2].

The particle content of the Standard Model is summarized in Fig. 1.1. Particles are grouped into fermions, which comprise all known matter, and bosons, which mediate the interactions between particles. Fermions consist of quarks and leptons, and are grouped into three generations. For example, the electron belongs to the first generation of leptons. The second and third generation counterparts of the electron are the muon and the tau lepton, and are over 200 and 30,000 times heavier than the electron respectively. The quarks are also organized into three generations (top and bottom quarks, charm and strange quarks, and up and down quarks), and

431 carry fractional electric charge. Bosons are force carriers; the interaction of fermions  
 432 with bosons corresponds to fundamental forces. The Standard Model describes the  
 433 electromagnetic force, the strong nuclear force, and the weak nuclear force. Through  
 434 the strong force, quarks can form composite particles known as hadrons. Familiar  
 435 examples of hadrons are the protons and neutrons in the nucleus of an atom.

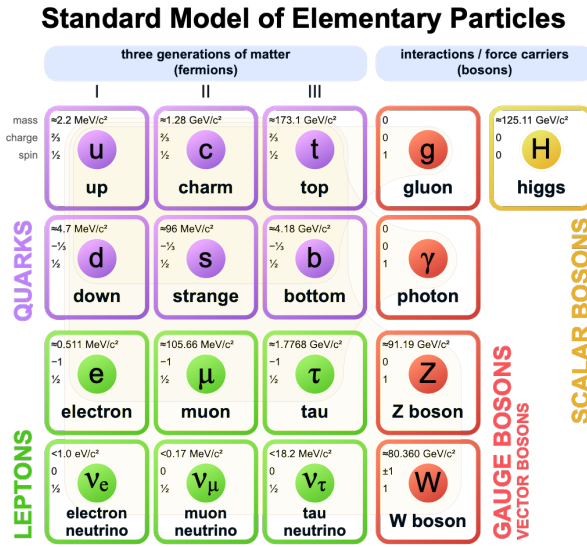


Figure 1.1: Table of Standard Model particles showing the grouping of the fermions into three generations of matter and the bosons, responsible for carrying the three fundamental forces in the Standard Model. The masses, charges, and spins of the particles are shown. The antimatter counterparts of the fermions are not shown. The possible interactions between the fermions and gauge bosons are highlighted.

## 436 1.2 The Standard Model as a gauge theory

437 In this section we lay the theoretical foundations of the Standard Model as a gauge  
 438 theory, starting from the principle of gauge invariance (gauge symmetry), with local  
 439 gauge symmetries giving rise to interactions between particles.

440 Gauge theories of elementary particle interactions originate from a freedom of  
 441 choice in the mathematical description of particle fields which has no effect on the  
 442 particles' physical states [4]. The existence and form of the particles' interactions,

443 can be deduced from the existence of physically indeterminate, gaugable quantities.

444 An example of this gauge invariance is classical physics is the electromagnetic  
445 interaction, where the fundamental field is the four-vector potential  $A^\mu$  [4]. The  
446 physical electromagnetic fields and Maxwell's equations arise from the elements of  
447 the tensor  $F_{\mu\nu}(x) = \partial_\mu A_\nu(x) - \partial_\nu A_\mu(x)$ . Any two choices of  $A^\mu$  that are related by a  
448 transformation of the form

$$A_\mu \rightarrow A_\mu + \partial_\mu \alpha \quad (1.1)$$

449 for any real, differentiable function  $\alpha(x)$ , describe the same physical configuration,  
450 and has no effect on Maxwell's equations. This "redundancy" in the choice of gauge  
451 in Eqn. 1.1 is called a gauge symmetry.

452 One important consequence of gauge symmetry comes from the application of  
453 Noether's theorem, which states that for every global transformation under which the  
454 Lagrangian density is invariant, there exists a conserved quantity. If  $\mathcal{L}(\Psi(x), \partial_\mu \Psi(x))$   
455 is invariant under the transformation of the wave function  $\Psi(x) \rightarrow \Psi'(x)$ , where  
456  $\Psi'(x) = \Psi(x) + \delta\Psi(x)$ , then there exists a conserved current

$$\partial_\mu \left( \frac{\partial \mathcal{L}(x)}{\partial (\partial_\mu \Psi(x))} \delta\Psi(x) \right) = 0 \quad (1.2)$$

457 In classical mechanics, the conservation of linear momentum, angular momentum,  
458 and energy follows from translational invariance, rotational variance, and invariance  
459 under translations in time [4]. Likewise, charge conservation can be shown to arise  
460 from the invariance of the Dirac Lagrangian density  $\mathcal{L}_{\text{Dirac}} = \bar{\Psi}(i\gamma^\mu \partial_\mu - m)\Psi$  under the  
461 particle wavefunction's phase transformation,  $\Psi'(x) = \exp(i\epsilon\chi)\Psi(x)$ . Thus Noether's  
462 theorem establishes a correspondence between a gauge symmetry and a conserved  
463 internal property (e.g. charge or momentum).

464 Interactions between particles arise if we modify the wave function with a phase

<sup>465</sup> transformation  $\Psi'(x) = \exp(ie\chi)\Psi(x)$ , and allow the phase  $\chi$  to be a function of  
<sup>466</sup> spacetime [4]. A wave function of the form

$$\Psi'(x) = \exp(ie\chi(x))\Psi(x) \quad (1.3)$$

<sup>467</sup> can be verified to *not* be a solution to the Dirac equation for free particles:  $(i\gamma^\mu\partial_\mu -$   
<sup>468</sup>  $m)\Psi(x) = 0$ . This necessitates a modified Dirac equation, where the derivative takes  
<sup>469</sup> into account that the vector field  $V(x)$  needs to be compared at two displaced space-  
<sup>470</sup> time points in a curvilinear coordinate system:

$$\mathcal{D}_\mu \equiv \lim_{\Delta x^\mu \rightarrow 0} \frac{V_{||}(x + \Delta x) - V(x)}{\Delta x^\mu} \quad (1.4)$$

<sup>471</sup> We define a covariant derivative,

$$D_\mu = \partial_\mu + ieA_\mu \quad (1.5)$$

<sup>472</sup> where  $A_\mu(x)$  is a 4-vector potential. Thus the modified Dirac equation reads:

$$(i\gamma^\mu\mathcal{D}_\mu - m)\Psi(x) = 0 \quad (1.6)$$

<sup>473</sup> The simultaneous gauge transformation  $A'_\mu(x) = A_\mu(x) - \partial_\mu\chi(x)$  and wavefunction  
<sup>474</sup> transformation  $\Psi'(x) = \exp(ie\chi(x))\Psi(x)$  leaves the covariant-derivative form of the  
<sup>475</sup> Dirac equation (Eqn 1.1) invariant.

<sup>476</sup> The generalization of this result is as follows: if a theory is invariant for unitary  
<sup>477</sup> transformations  $U$  of the particle states according to

$$\Psi' = U\Psi \quad (1.7)$$

478 One must define a derivative of the form

$$D^\mu = \partial^\mu + igB^\mu \quad (1.8)$$

479 to keep the theory invariant under Eqn. 1.7. The four-potential  $B^\mu$  represents the  
480 interacting four-potential which must be added to keep the theory invariant.

481 In the case of the Standard Model, the theory is built around the gauge trans-  
482 formations  $G = SU(3) \times SU(2) \times U(1)$ .  $SU(3)$  is associated to the strong force  
483 (subscripted  $C$ );  $SU(2)$  is associated to the weak force (subscripted  $L$ ); and  $U(1)$  is  
484 hypercharge (subscripted  $Y$ ). The gauge-covariant derivative is

$$\mathcal{D}_\mu = \partial_\mu - ig'B_\mu \frac{Y}{2} - igW_\mu^\alpha \frac{\tau_a}{2} - ig_s G_\mu^k \frac{\lambda_k}{2} \quad (1.9)$$

485 • In the  $U(1)_Y$  term,  $B_\mu$  is the weak hypercharge field.

486 • In the  $SU(2)_L$  term,  $W_\mu(x) = (W_\mu^1(x), W_\mu^2(x), W_\mu^3(x))$  are a triplet of four-  
487 potentials.  $\tau/2$  are the Pauli matrices, generators of the  $SU(2)$  transformation.

488 • In the  $SU(3)_C$  term, the gluon (color) field is  $G_\mu$ .  $\lambda_k$  are the Gell-Man matrices,  
489 generators of the  $SU(3)$  transformation.

490 The invariance of the Standard Model under  $SU(3)_C \times SU(2)_L \times U(1)_Y$  requires  
491 massless fermions and massless force carriers.

### 492 1.3 The Higgs Mechanism

493 To introduce mass into the theory, i.e. to change the propagation of the gauge par-  
494 ticles and all the fermions, the physical vacuum cannot have all the symmetries of  
495 the Standard Model Lagrangian [4]. The symmetries of the physical vacuum must  
496 be spontaneously broken, without affecting gauge invariance in the Lagrangian. The

497 Higgs mechanism proposes the existence of a scalar field, or fields, with nonzero vac-  
 498 um expectation values, which reduce the gauge symmetries of the physical vacuum  
 499 from  $SU(3)_C \times SU(2)_L \times U(1)_Y$  down to  $SU(3)_C \times U(1)_{EM}$ .

500 The Higgs field interacts with the gauge bosons and fermions throughout space,  
 501 impeding their free propagation. The resulting broken symmetry correctly predicts  
 502 the mass ratio of the neutral (Z) and charged (W) massive electroweak bosons, and  
 503 predicts that at least one physical degree of freedom in the Higgs field is a particle  
 504 degree of freedom, called the Higgs boson. The location of the minimum of the Higgs  
 505 potential can be constrained from previously measured Standard Model parameters,  
 506 but the shape of the mass distribution of the Higgs boson must be experimentally  
 507 measured.

508 The minimal choice of Higgs field comes from the breaking of  $SU(2)_L \times U(1)_Y$   
 509 down to  $U(1)_{EM}$ . The smallest  $SU(2)$  multiplet is the doublet. The existence of three  
 510 massive electroweak bosons leads the Higgs sector to have at least three degrees of  
 511 freedom. The minimal single-doublet complex scalar Higgs field is

$$\Phi(x) = \begin{pmatrix} \phi^+(x) \\ \phi^0(x) \end{pmatrix} = \frac{1}{\sqrt{2}} \begin{pmatrix} \phi_1^+(x) + i\phi_2^+(x) \\ \phi_1^0(x) + i\phi_2^0(x) \end{pmatrix} \quad (1.10)$$

512 where  $\phi_1^+$ ,  $\phi_2^+$ ,  $\phi_1^0$ , and  $\phi_2^0$  are real (four degrees of freedom). By convention, the  
 513 nonzero vacuum expectation value is assigned to  $\phi_1^0$ .

514 The minimal self-interacting Higgs potential that is invariant under  $SU(2)_L \times$   
 515  $U(1)_Y$  is given by

$$V(\Phi^\dagger \Phi) = -\mu^2 \Phi^\dagger \Phi + \lambda (\Phi^\dagger \Phi)^2, \quad \mu^2 > 0, \lambda > 0 \quad (1.11)$$

516 where  $\lambda$  is the coupling strength of the four-point Higgs interaction. The potential

517 energy is minimized at

$$\Phi_{\min} = \frac{1}{\sqrt{2}} \begin{pmatrix} 0 \\ v \end{pmatrix}, \text{ where } v = \sqrt{\mu^2/\lambda} \quad (1.12)$$

518 Choosing a fixed orientation of  $\langle \Phi \rangle$  out of a continuous set of possible ground states  
519 spontaneously breaks the symmetry of the physical vacuum, as illustrated in Fig 1.2.

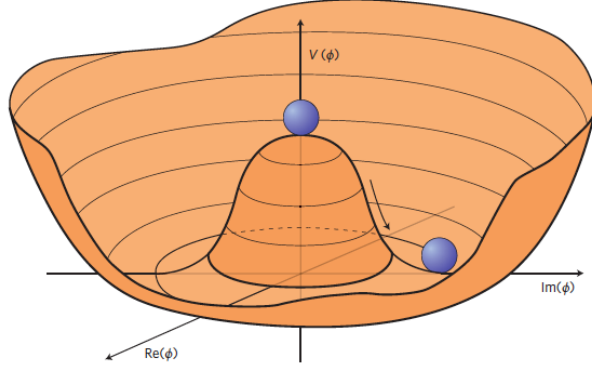


Figure 1.2: An illustration of the Higgs potential [5]. Choosing any of the points at the bottom of the potential breaks spontaneously the rotational  $U(1)$  symmetry.

520 The excitations of the Higgs field with respect to the minimum  $\Phi_{\min}$  are parameterized by

$$\Phi(x) = \exp(i\xi(x) \cdot \tau) \frac{1}{\sqrt{2}} \begin{pmatrix} 0 \\ v + H(x) \end{pmatrix} \quad (1.13)$$

522 Three degrees of freedom are coupled directly to the electroweak gauge bosons; this  
523 is often referred to as the gauge bosons “eating” the Goldstone bosons to form the  
524 longitudinal polarizations of the massive spin-1 boson states. The  $H(x)$  excitation is  
525 in the radial direction and corresponds to the free particle state of the Higgs boson.

## 526 1.4 Two-Higgs Doublet Models

527 One of the simplest possible extensions to the Standard Model is adding a doublet  
528 to the minimal Higgs sector of the Standard Model, which is a  $SU(2)_L$  doublet  $H$

529 with hypercharge  $Y = +\frac{1}{2}$ , denoted here as  $H \sim 2_{+1/2}$ . These extensions are found  
 530 in several theories such as supersymmetry. A general 2HDM can be extended with a  
 531 light scalar (2HDM+S) to obtain a rich set of exotic Higgs decays [6].

The charges of the Higgs fields are chosen to be  $H_1 \sim 2_{-1/2}$  and  $H_2 \sim 2_{+1/2}$ , which acquire vacuum expectation values  $v_{1,2}$  which are assumed to be real and aligned [6]. Expanding about the minima yields two complex and four real degrees of freedom:

$$H_1 = \frac{1}{\sqrt{2}} \begin{pmatrix} v_1 + H_{1,R}^0 + iH_{1,I}^0 \\ H_{1,R}^- + iH_{1,I}^- \end{pmatrix} \quad (1.14)$$

$$H_2 = \frac{1}{\sqrt{2}} \begin{pmatrix} H_{2,R}^+ + iH_{2,I}^+ \\ v_2 + H_{2,R}^0 + iH_{2,I}^0 \end{pmatrix} \quad (1.15)$$

532 The charged scalar and pseudoscalar mass matrices are diagonalized by a rotation  
 533 angle  $\beta$ , defined as  $\tan \beta = v_2/v_1$ . One charged (complex) field and one neutral  
 534 pseudoscalar combination of  $H_{1,2,I}^0$  are eaten by the SM gauge bosons after electroweak  
 535 symmetry breaking [6]. The other complex field yields two charged mass eigenstates  
 536  $H^\pm$ , which are assumed to be heavy. The remaining three degrees of freedom yield  
 537 one neutral pseudoscalar mass eigenstate

$$A = H_{1,I}^0 \sin \beta - H_{2,I}^0 \cos \beta \quad (1.16)$$

538 and two neutral scalar mass eigenstates (where  $-\pi/2 \leq \alpha \leq \pi/2$ )

$$\begin{pmatrix} h \\ H^0 \end{pmatrix} = \begin{pmatrix} -\sin \alpha & \cos \alpha \\ \cos \alpha & \sin \alpha \end{pmatrix} \begin{pmatrix} H_{1,R}^0 \\ H_{2,R}^0 \end{pmatrix} \quad (1.17)$$

539 We assume that the 2HDM is near or in the decoupling limit:  $\alpha \rightarrow \pi/2 - \beta$ , where the  
 540 lightest state in the 2HDM is  $h$ , which we identify as the 125 GeV Higgs particle [6].  
 541 In this limit, the fermion couplings of  $h$  become identical to the Standard Model

542 Higgs, while the gauge boson couplings are very close to Standard Model-like for  
543  $\tan \beta \gtrsim 5$ . All of the properties of  $h$  can be determined by just two parameters:  $\tan \beta$   
544 and  $\alpha$ , and the fermion couplings to the two Higgs doublets.

545 2HDM can be extended by a scalar singlet (2HDM+S) [6]:

$$S = \frac{1}{\sqrt{2}}(S_R + iS_I) \quad (1.18)$$

546 If this singlet only couples to the Higgs doublets  $H_{1,2}$  and has no direct Yukawa  
547 couplings, all of its couplings to SM fermions result from mixing with  $H_{1,2}$ . Under  
548 these simple assumptions, exotic Higgs decays  $h \rightarrow ss \rightarrow X\bar{X}Y\bar{Y}$  or  $h \rightarrow aa \rightarrow$   
549  $X\bar{X}Y\bar{Y}$ , and  $h \rightarrow aZ \rightarrow X\bar{X}Y\bar{Y}$  are permitted, where  $s(a)$  is a (pseudo)scalar mass  
550 eigenstate mostly composed of  $S_R(S_I)$ , and  $X, Y$  are Standard Model fermions or  
551 gauge bosons. There are two pseudoscalars in the 2HDM+S, and the mostly singlet-  
552 like pseudoscalar can be chosen to be the one lighter than the SM-like Higgs. For  
553  $m_a < m_h - m_Z \sim 35$  GeV, the exotic Higgs decay  $h \rightarrow Za$  is possible, and for  
554  $m_a < m_h/2 \approx 63$  GeV, the exotic Higgs decay  $h \rightarrow aa$  is possible.

555 In 2HDM, and by extension 2HDM+S, there are four types of fermion couplings  
556 commonly discussed in the literature that forbid flavor-changing neutral currents at  
557 tree level [6]. These are referred to as Type I (all fermions couple to  $H_2$ ), Type II  
558 (MSSM-like,  $d_R$  and  $e_R$  couple to  $H_1$ ,  $u_R$  to  $H_2$ ), Type III (lepton-specific, leptons  
559 and quarks couple to  $H_1$  and  $H_2$  respectively) and Type IV (flipped, with  $u_R$ ,  $e_R$   
560 coupling to  $H_2$  and  $d_R$  to  $H_1$ ). The exact branching ratios of the pseudoscalars to  
561 Standard Model particles vary depending on the 2HDM+S model and the value of  
562  $\tan \beta$  (e.g. Fig. 1.3).

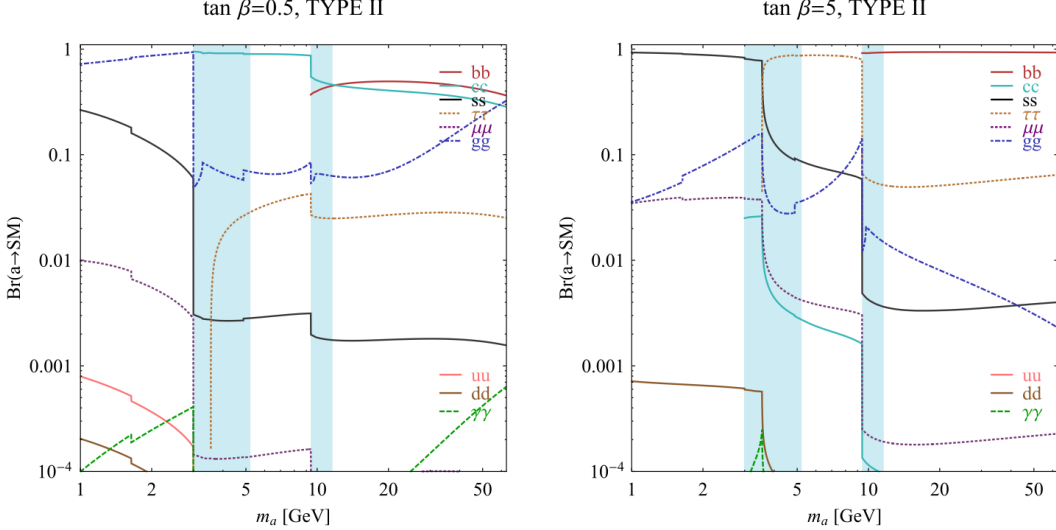


FIG. 7 (color online). Branching ratios of a singletlike pseudoscalar in the 2HDM + S for type-II Yukawa couplings. Decays to quarkonia likely invalidate our simple calculations in the shaded regions.

Figure 1.3: Branching ratios of a singlet-like pseudoscalar in Type II 2HDM+S for  $\tan\beta = 0.5$  (left) and  $\tan\beta = 5$  (right) from [6], showing the dependence of the branching ratios on  $\tan\beta$ , as well as the prominence of the branching ratios to  $bb$  and  $\tau\tau$ , the channels searched for in the analysis presented here.

## 1.5 Two Real Singlet Model

The two real singlet model (TRSM) adds two real singlet degrees of freedom to the Standard Model. These are written as two real singlet fields  $S$  and  $X$ . Depending on the vacuum expectation values acquired by the scalars, different phases of the model can be realized [7]. To reduce the number of free parameters, two discrete  $\mathbb{Z}_2$  symmetries are introduced. The fields are decomposed as

$$\Phi = \begin{pmatrix} 0 \\ \frac{\phi_h + v}{\sqrt{2}} \end{pmatrix}, S = \frac{\phi_S + v_S}{\sqrt{2}}, X = \frac{\phi_X + v_X}{\sqrt{2}} \quad (1.19)$$

To achieve electroweak-breaking symmetry,  $v = v_{SM} \sim 246$  GeV is necessary. If the vacuum expectation values  $v_S, v_X \neq 0$  the  $\mathbb{Z}_2$  are spontaneously broken, and the fields  $\phi_{h,S,X}$  mix into three physical scalar states. This is called the broken phase and leads to the most interesting collider phenomenology.

573        The mass eigenstates  $h_{1,2,3}$  are related to the fields  $\phi_{h,S,X}$  through a  $3 \times 3$  orthogonal  
574        mixing matrix denoted  $R$ . The mass eigenstates are assumed to be ordered  $M_1 \leq$   
575         $M_2 \leq M_3$ .  $R$  is parameterized by the three mixing angles  $\theta_{hS}$ ,  $\theta_{hX}$ ,  $\theta_{SX}$ . The nine  
576        parameters of the scalar potential can be expressed in terms of the three physical  
577        Higgs masses, the three mixing angles, and the three vacuum expectation values.

578        After fixing one of the Higgs masses to the mass of the observed Higgs boson, and  
579        fixing the Higgs doublet vacuum expectation value to its Standard Model value, there  
580        are seven remaining free parameters of the TRSM [7].

581        In one benchmark scenario of TRSM [7], the heaviest scalar state  $h_3$  is identified  
582        with the 125 GeV Higgs,  $h_{125}$ , and it can decay asymmetrically  $h_{125} \rightarrow h_1 h_2$ , which  
583        we also denote  $h \rightarrow a_1 a_2$  to highlight the similarity with the symmetric decay  $h \rightarrow aa$   
584        typically interpreted in 2HDM+S as discussed. The parameter values in TRSM are  
585        chosen such that the coupling of  $h_3$  to Standard Model particles are nearly identical  
586        to the Standard Model predictions.

587        In benchmark scenario 1 (benchmark plane 1, or BP1) (Fig. 1.4) [7], the maximal  
588        branching ratios for  $h_3 \rightarrow h_1 h_2$  reach up to 7 – 8% which translates into a signal  
589        rate of around 3 pb. These maximal branching ratios are reached in the intermediate  
590        mass state for  $h_2$ ,  $M_2 \sim 60 – 80$  GeV. For  $M_2 < 40$  GeV, although phase space opens  
591        up significantly for light decay products, the branching ratio becomes smaller.

592        If the decay channel  $h_2 \rightarrow h_1 h_1$  is kinematically open (i.e.  $M_2 > 2M_1$ ), it is the  
593        dominant decay mode leading to a significant rate for the  $h_1 h_1 h_1$  final state, in a  
594        “cascade” decay. In BP1,  $BR(h_2 \rightarrow h_1 h_1) \simeq 100\%$  above the red line in Fig. 1.4. If,  
595        in addition,  $M_1 \gtrsim 10$  GeV, the  $h_1$  decays dominantly to  $b\bar{b}$  leading to a sizable rate  
596        for the  $b\bar{b}b\bar{b}b\bar{b}$  final state as shown in Fig. 1.4 (*bottom right*).

597        If the  $h_2 \rightarrow h_1 h_1$  decay is kinematically closed (i.e.  $M_2 < 2M_1$ ), both scalars decay  
598        directly to Standard Model particles, with branching ratios identical to a Standard  
599        Model-like Higgs boson, i.e. with the  $b\bar{b}b\bar{b}$  final state dominating, as shown in Fig. 1.4

600 (*bottom left*), while at smaller masses, combinations with  $\tau$  leptons and eventually  
601 final states with charm quarks and muons become relevant [7].

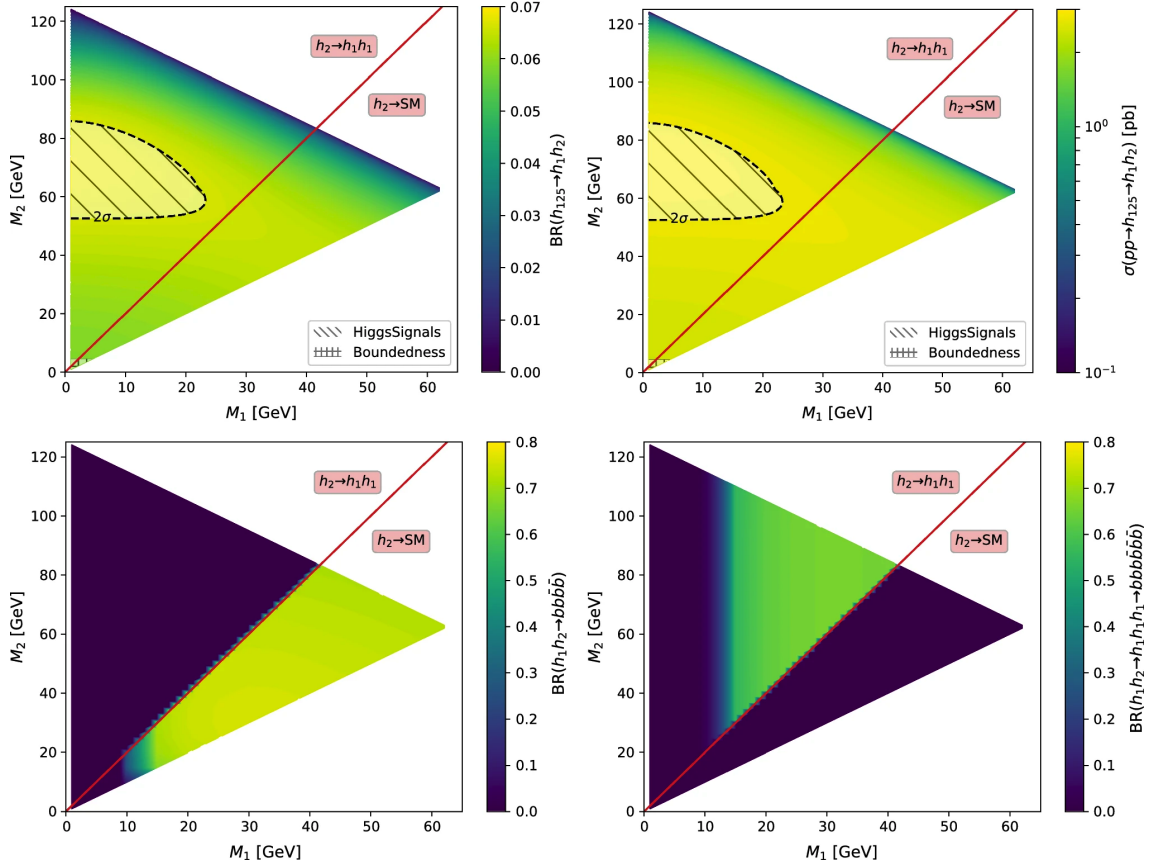


Figure 1.4: Benchmark plane BP1 for benchmark scenario 1 from [7], for the decay signature  $h_{125} \rightarrow h_1 h_2$  with  $h_{125} \equiv h_3$ , defined in the  $(M_1, M_2)$  plane. The color code shows  $\text{BR}(h_3 \rightarrow h_1 h_2)$  (*top left*) and the 13 TeV LHC signal rate for  $pp \rightarrow h_3 \rightarrow h_1 h_2$  (*top right*). The red line separates the region  $M_2 > 2M_1$ , where  $\text{BR}(h_2 \rightarrow h_1 h_1) \sim 100\%$ , from the region  $M_2 < 2M_1$ , where  $\text{BR}(h_2 \rightarrow F_{SM}) \sim 100\%$ . The *bottom left* and *right* show the branching ratio of the  $h_1 h_2$  into (respectively)  $b\bar{b}b\bar{b}$ , and through a  $h_2 \rightarrow h_1 h_1$  cascade to  $b\bar{b}b\bar{b}b\bar{b}$ . The hatched region indicates where the decay rate slightly exceeds the  $2\sigma$  upper limit inferred from the LHC Higgs rate measurements, though the region depends on the parameter choices and experimental searches should cover the whole mass range.

602 **Chapter 2**

603 **The Large Hadron Collider and the**  
604 **CMS Experiment**

605 This chapter introduces the key aspects of the CERN Large Hadron Collider (LHC)  
606 and the Compact Muon Solenoid (CMS) experiment where the work for this thesis was  
607 conducted. Section 2.1 describes the history of accelerator developments at CERN  
608 that led to the construction of the LHC, the current LHC configuration, and the  
609 largest experiments located at the LHC. The concepts of beam luminosity and pile-  
610 up, which are critical for understanding and measuring high-energy particle collisions,  
611 are described in Section 2.2 and discussed in the context of the High-Luminosity  
612 LHC (HL-LHC) upgrade in Section 2.3. Lastly, Section 2.4 describes the design  
613 and function of CMS and its subdetectors, and terminates in a description of data  
614 processing at CMS, beginning from online event filtering in the Level-1 Trigger, to  
615 processing in the High-Level Trigger, to offline particle reconstruction, and finally  
616 long-term storage and processing of measured events.

## 617 2.1 The Large Hadron Collider

618 CERN, the European Organization for Nuclear Research, is an international organiza-  
619 tion based in Meyrin, Switzerland which operates the world's largest particle physics  
620 laboratory, and is the site of the Large Hadron Collider (LHC) [8]. The very first  
621 accelerator built at CERN was the 600 MeV Synchrocyclotron (SC), which initially  
622 provided beams for CERN's first experiments. The newer and more powerful Proton  
623 Synchrotron (PS), which could accelerate particles to an energy of 28 GeV, began op-  
624 erations in 1959 and is still in use today. The first hadron collider at CERN was the  
625 Intersecting Storage Rings (ISR), which consisted of two interlaced rings each with a  
626 diameter of 200. The ISR collided protons at a center-of-mass energy of 62 GeV and  
627 began measuring collisions in 1971. In 1968 CERN began to accelerate heavy ions  
628 in the Super Proton Synchrotron (SPS), which is 7 kilometers in circumference and  
629 was the first of CERN's giant underground rings to be built. The SPS became the  
630 forefront of CERN's particle physics program in 1976, and in 1981 was converted into  
631 a proton-antiproton collider. The final and largest underground ring constructed at  
632 CERN was the Large Electron-Positron (LEP) collider, which was commissioned in  
633 July 1989 and hosted 5176 magnets and 128 accelerating cavities located around a  
634 27-kilometer circumference. Over 11 years of research, four detectors, ALEPH, DEL-  
635 PHI, L3, and OPAL measured the collisions, with collision energies reaching up to  
636 209 GeV in the year 2000. In November 2000, LEP was closed down to make way for  
637 the construction of the LHC in the same tunnel.

638 In its current configuration, the LHC accelerator complex at CERN is a suc-  
639 cession of machines that accelerate particles in stages until they reach their final energy  
640 of 6.5 TeV per beam [9] [10]. In Linear accelerator 4 (Linac4), negative hydrogen  
641 ions (hydrogen atoms with an additional electron) are accelerated to 160 MeV, and  
642 stripped of their two electrons, leaving only protons, before entering the Proton Syn-  
643 chrotron Booster (PSB). These protons are accelerated to 2 GeV, then to 26 GeV in

644 the Proton Synchrotron (PS), and 450 GeV in the Super Proton Synchrotron (SPS).  
645 The protons are transferred to the two beam pipes of the Large Hadron Collider  
646 (LHC). The LHC is a 27-kilometer ring of superconducting magnets, inside which  
647 one beam circulates clockwise and the other counterclockwise. Each LHC ring takes  
648 4 minutes and 20 seconds to fill, and it takes about 20 minutes for the protons to  
649 reach their maximum energy. During normal operating conditions, beams circulate  
650 for many hours inside the LHC ring.

651 The beams of particles in the LHC are made to collide at a center-of-mass energy  
652 of up to 14 TeV, at four positions at particle detector experiments located around  
653 the ring: ATLAS, CMS, ALICE, and LHCb. An aerial view of the four major  
654 experiments' locations is shown in Fig. 2.1 [11]. ATLAS and CMS are the two  
655 general-purpose detectors with broad physics programmes spanning Standard Model  
656 measurements and searches for signatures of new physics [12] [13]. The two experi-  
657 ments use different technical solutions and different magnet system designs. ALICE  
658 is a general-purpose detector dedicated to measuring LHC heavy-ion collisions, and  
659 is designed to address the physics of strongly interacting matter, and the properties  
660 of quark-gluon plasma [14]. The LHCb experiment specializes in investigating CP vi-  
661 olation through measuring the differences in matter and antimatter, by using a series  
662 of subdetectors to detect mainly forward particles close to the beam direction [15].

## 663 2.2 Luminosity and pile-up

664 In order to search for rare processes, such as those resulting from a Higgs, W, or Z  
665 boson, a large number of parton interactions per second are required at the LHC.  
666 The number of events generated per second by the LHC collisions is given by

$$N_{event} = \mathcal{L} \cdot \sigma_{event} \quad (2.1)$$

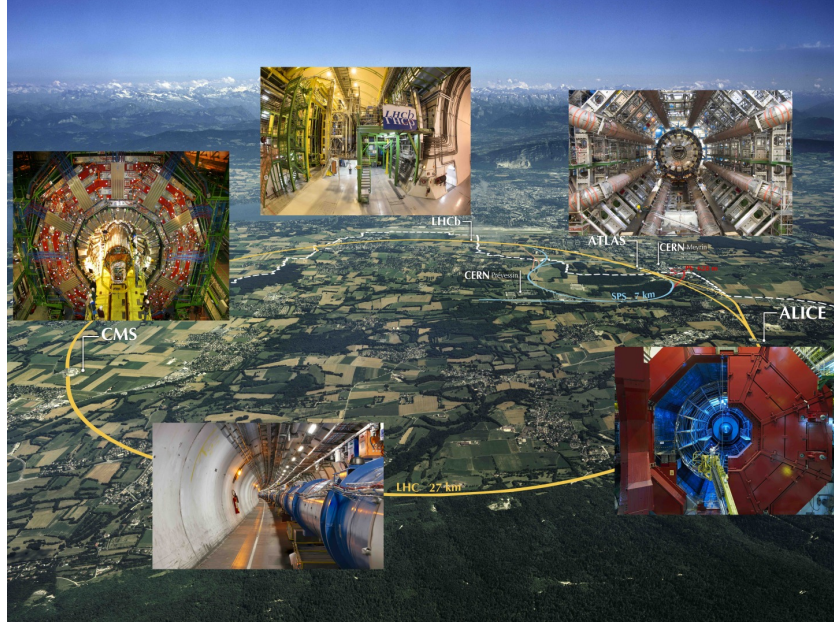


Figure 2.1: Aerial view of the Large Hadron Collider (LHC) spanning the border of France and Switzerland, and the four major experiments located around the ring: CMS (Compact Muon Solenoid), LHCb (LHC beauty), ATLAS (A Toroidal LHC Apparatus), and ALICE (A Large Ion Collider Experiment) [11].

where  $\sigma_{event}$  is the cross-section for the event under study, and  $\mathcal{L}$  the instantaneous luminosity. The instantaneous luminosity is measured in units of  $\text{cm}^{-2} \text{ s}^{-1}$ , and depends only on the beam parameters, and can be written for a Gaussian beam distribution as:

$$\mathcal{L} = \frac{N_b^2 n_b f_{rev} \gamma_r}{4\pi \epsilon_n \beta^*} F \quad (2.2)$$

where the parameters are as defined, along with some example typical nominal values in Phase-1 of the LHC [16] [17]:

- $N_b$  is the number of particles per bunch ( $N_b \approx 1.15 \times 10^{11}$  protons per bunch)
- $n_b$  is the number of bunches per beam (maximum 2808),
- $f_{rev}$  is the revolution frequency ( $\approx 11 \text{ kHz}$ ),
- $\gamma_r$  is the relativistic gamma factor,

- $\epsilon_n$  is the normalized transverse beam emittance (area in a transverse plane occupied by the beam particles),
- $\beta^*$  is the beta function at the collision point ( $\beta^* = 0.55$  m),
- and  $F$  is the geometric luminosity reduction factor due to the crossing angle at the interaction points ( $F \approx 0.84$  for Phase-1. Note that complete overlap would give  $F = 1$ ).

Peak luminosity at interaction points 1 and 5 reach values of  $\sim 1.0 \times 10^{34} \text{ cm}^{-2} \text{ s}^{-1}$ , with peak luminosity per bunch crossing reaching  $\sim 3.56 \times 10^{34} \text{ cm}^{-2} \text{ s}^{-1}$ .

Per Eqn. 2.1, the integrated luminosity over time is proportional to the number of events produced, and the size of LHC datasets is commonly presented in terms of integrated luminosity. Collider operation aims to optimize the integrated luminosity. Thus the exploration of rare events in the LHC collisions requires both high beam energies and high beam intensities.

The interaction vertex corresponding to the hard scattering of the protons is called the primary interaction vertex, or primary vertex (PV). The LHC's nominal beam luminosities are sufficiently large for multiple proton-proton collisions to occur in the same time window of 25 nanoseconds in which proton bunches collide [18]. To measure a proton-proton collision, the primary vertices must be separated from overlapping collisions, called “pile-up” collisions.

The pile-up is defined as the average number of  $pp$  collisions per bunch crossing, and can be estimated from the inelastic  $pp$  cross section of  $\sigma_{\text{inel}} = 68.6$  millibarns at a center-of-mass energy of  $\sqrt{s} = 13$  TeV [19]:

$$\text{Pile-up} = \frac{\mathcal{L} \times \sigma_{\text{inel}}}{n_b \cdot f} \sim 22 \quad (2.3)$$

A distribution of pile-up in the data-taking years 2016-2018 is shown in Fig. 2.2.

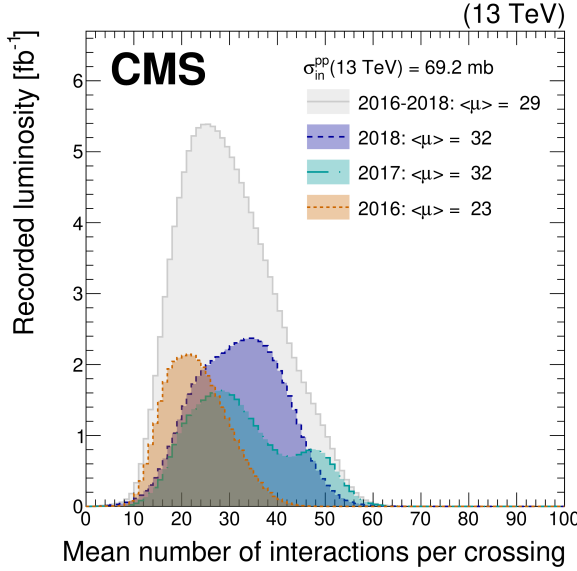


Figure 2.2: Distribution of the mean number of inelastic collisions per bunch crossing (pile-up) in data [18], for proton-proton collisions in 2016 (*dotted orange*), 2017 (*dotted light blue*), 2018 (*dotted dark blue*), and integrated over 2016-2018 (*solid grey*). A cross-section of inelastic proton-proton collisions of 69.2 mbarns is assumed. In the running conditions of the High-Luminosity LHC, pile-up will reach unprecedented levels of up to 200 per bunch crossing [20].

These multiple collisions will lead to higher occupancies in the detector, and particles originating from the pile-up interactions can be confused with those originating from the primary vertex. Thus, higher luminosities create more intense pile-up conditions, posing a greater challenge to detector performance and particle reconstruction and identification.

## 2.3 The High-Luminosity LHC

The High-Luminosity LHC (HL-LHC) is a major upgrade of the LHC scheduled to take place in the late 2020s, that will increase the instantaneous luminosity by a factor of five beyond the original design value, and the integrated luminosity by a factor of ten [20]. This will be accomplished through accelerator technological advances: for instance, reduction of the interaction point  $\beta^*$  from 0.55 m down to 0.15

711 m by installation of new final-focusing magnets, and improvements in the geometric  
712 luminosity loss factor  $F \approx 1$  through the installation of crab cavities that optimize  
713 the orientation of colliding bunches. A further discussion of the HL-LHC upgrades  
714 for the CMS detector follows in Chapter 3.

## 715 2.4 The CMS Detector

716 We give a brief overview of the Compact Muon Solenoid (CMS) experiment here  
717 and discuss each of the subdetectors in more detail in the following sections. The  
718 CMS experiment was conceived to study proton-proton and lead-lead collisions at  
719 a center-of-mass energy of 14 TeV (5.5 TeV nucleon-nucleon) and at luminosities up  
720 to  $10^{34} \text{ cm}^{-2} \text{ s}^{-1}$  ( $10^{27} \text{ cm}^{-2} \text{ s}^{-1}$ ) [21] [22]. Starting from the beam interaction region  
721 at the center of the CMS detector, particles first pass through a silicon pixel and  
722 strip tracker, in which charged-particle trajectories (tracks) and origins (vertices)  
723 are reconstructed from signals (hits) in the sensitive layers. The tracker, electro-  
724 magnetic calorimeter (ECAL), and hadronic calorimeter (HCAL) are immersed in a  
725 high-magnetic-field superconducting solenoid that bends the trajectories of charged  
726 particles. After passing through the tracker, electrons and photons are then absorbed  
727 in the electromagnetic calorimeter (ECAL) comprised of lead-tungstate scintillating-  
728 crystals. The corresponding electromagnetic showers are detected as clusters of energy  
729 recording in neighboring cells, from which the direction and energy of the particles can  
730 be determined. Charged and neutral hadrons may initiate a hadronic shower in the  
731 ECAL as well, which is then fully absorbed in the hadron calorimeter (HCAL). The  
732 resulting clusters are used to estimate their direction and energies. Muons and neu-  
733 trinos pass through the calorimeters with little to no interactions. Neutrinos escaped  
734 undetected; muons produce hits in additional gas-ionization chamber muon detectors  
735 housed in the iron yoke of the flux-return. A sketch of example particle interactions

in a transverse slice of the CMS detector is shown in Fig. 2.3. The collision data is recorded with the use of the Level-1 (L1) trigger (discussed in greater detail in 2.5.5), the High-Level Trigger (HLT), and data acquisition systems ensuring high efficiency in selecting physics events of interest.

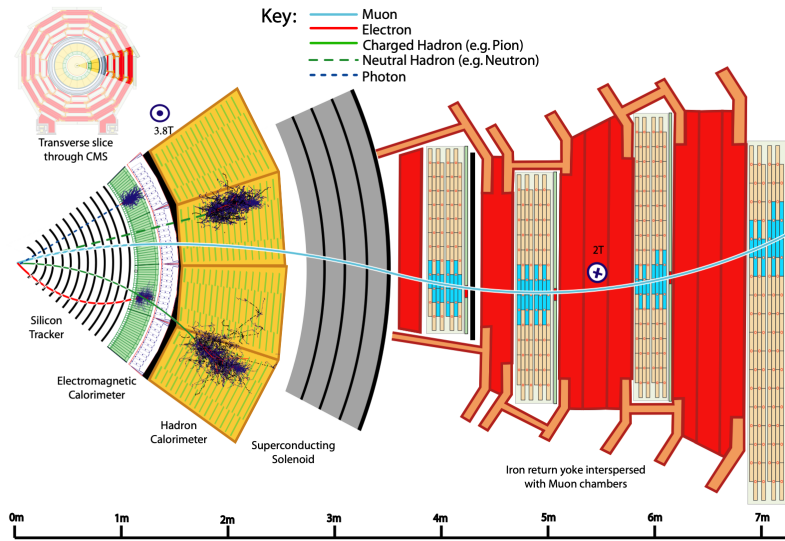


Figure 2.3: Sketch of particle trajectories of muons, electrons, charged and neutral hadrons, and photons in a transverse cross-section of the CMS detector [22].

CMS uses a right-handed coordinate system [21]. The origin is centered at the nominal collision point inside the experiment. The  $x$  axis points towards the center of the LHC, and the  $y$  axis points vertically upwards. The  $z$  axis points along the beam direction. The azimuthal angle,  $\phi$ , is measured from the  $x$  axis in the  $x$ - $y$  plane, and the radial coordinate in this plane is denoted by  $r$ . The polar angle,  $\theta$ , is measured from the  $z$  axis. The pseudorapidity,  $\eta$ , is defined as  $\eta = -\ln \tan(\theta/2)$ . The momentum and energy transverse to the beam direction, denoted by  $p_T$  and  $E_T$  respectively, are computed from the  $x$  and  $y$  components. The momentum imbalance in the transverse plane is called the missing transverse momentum, and its magnitude is denoted by  $E_T^{\text{miss}}$ .

## 750 2.5 Sub-detectors of CMS

751 This section details the sub-detectors of CMS that operate to identify and precisely  
752 measure muons, electrons, photons, and jets over a large energy range.

### 753 2.5.1 Inner tracking system

754 The CMS Tracker performs robust tracking and detailed vertex reconstruction in the  
755 4 T magnetic field of the superconducting solenoidal magnet. The primary sensors  
756 used in the tracker are  $p^+$  on  $n$ -bulk devices, which allow high voltage operation and  
757 are radiation-resistant [23] [24]. The active envelope of the CMS Tracker extends to a  
758 radius of 115 cm, over a length of approximately 270 cm on each side of the interaction  
759 point [23]. Charged particles in the region  $|\eta| \lesssim 1.6$  benefit from the full momentum  
760 measurement precision. In this region, a charged particle with  $p_T$  of 1000 GeV has a  
761 sagitta of  $\sim 195$   $\mu\text{m}$ . The Tracker acceptance extends further to  $|\eta| = 2.5$ , with a  
762 reduced radius of approximately 50 cm.

763 The high magnetic field of CMS causes low  $p_T$  charged particles to travel in helical  
764 trajectories with small radii. The majority of events contain particles with a steeply  
765 falling  $p_T$  spectrum, resulting in a track density which rapidly decreases at higher  
766 radii.

767 A schematic view of the current Phase-1 CMS tracker [25], including the pixel  
768 detector, is shown in Fig. 2.4. The Phase-1 pixel detector consists of three barrel  
769 layers (BPIX) at radii of 4.4 cm, 7.3 cm, and 10.2 cm, and two forward/backward disks  
770 (FPIX) at longitudinal positions of  $\pm 34.5$  cm and  $\pm 46.5$  cm, and extending in radius  
771 from about 6 cm to 15 cm. These pixelated detectors produce 3D measurements along  
772 the paths of charged particles with single hit resolutions between 10-20  $\mu\text{m}$ .

773 After the pixel and on their way out of the tracker, particles pass through the  
774 silicon strip tracker which reaches out to a radius of 130 cm (Fig. 2.4). The sensor el-

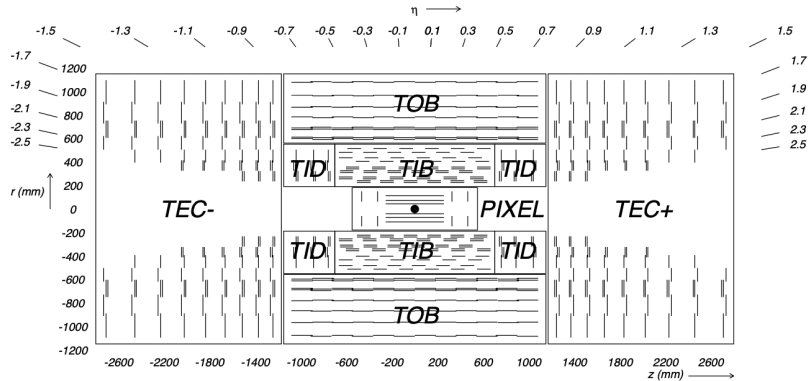


Figure 2.4: Cross section of the current Phase-1 CMS tracker [25]. Each line represents a detector module. Double lines indicate back-to-back modules which deliver two-dimensional (stereo) hits in the strip tracker.

ments in the strip tracker are single-sided  $p$ -on- $n$  type silicon micro-strip sensors [21]. The silicon strip detector consists of four inner barrel (TIB) layers assembled in shells, with two inner endcaps (TID), each composed of three small discs. The outer barrel (TOB) consists of six concentric layers. Two endcaps (TEC) close off the tracker on either end.

### 2.5.2 ECAL

The electromagnetic calorimeter (ECAL) of CMS measures electromagnetic energy deposits with high granularity. One of the driving criteria in the design was the capability of detecting the Standard Model Higgs boson decay to two photons (in fact, the channel in which the 125 GeV Higgs boson was discovered at CMS). ECAL is a hermetic homogeneous calorimeter comprised of 61,200 lead tungstate ( $\text{PbWO}_4$ ) crystals mounted in the central barrel, with 7,324 crystals in each of the two endcaps [21]. A preshower detector is located in front of the endcap crystals. Avalanche photodiodes (APDs) are used as photodetectors in the barrel and vacuum phototriodes (VPTs) in the endcaps.

The design of the ECAL is driven by the behaviour of high-energy electrons, which

predominantly lose energy in matter via bremsstrahlung, and high-energy photons by  $e^+e^-$  pair production. The characteristic amount of matter traversed for these interactions is the radiation length  $X^0$ , usually measured in units of g cm $^{-2}$ . The radiation length is also the mean distance over which a high-energy electron loses all but  $1/e$  of its energy via bremsstrahlung [26]. Thus high granularity in  $\eta$  and  $\phi$ , and the length of the ECAL crystals, is designed to capture the shower of  $e/\gamma$  produced by electrons and photons.

The barrel part of the ECAL (EB) covers the pseudorapidity range  $|\eta| < 1.479$  [21]. The barrel granularity is 360-fold in  $\phi$  and  $(2 \times 85)$ -fold in  $\eta$ . The crystal cross-section corresponds to approximately  $0.0174 \times 0.0174$  in  $\eta - \phi$  or  $22 \times 22$  mm $^2$  at the front face of the crystal, and  $26 \times 26$  mm $^2$  at the rear face. The crystal length is 230 mm, corresponding to  $25.8 X_0$ .

The ECAL read-out acquires the signals of the photodetectors [21]. At each bunch crossing, digital sums representing the energy deposit in a trigger tower, comprising  $5 \times 5$  crystals in  $\eta \times \phi$ , are generated and sent to the Level-1 trigger system (detailed in Section 2.5.5).

### 2.5.3 HCAL

The hadronic calorimeter (HCAL) of CMS measures hadronic energy, which is key to characterizing the presence of apparent missing transverse energy which could arise from hadron jets and neutrinos or exotic particles [21]. A schematic of the components of HCAL are shown in Fig. 2.5. The HCAL barrel (HB) and endcaps (HE) are located outside of the tracker and the ECAL, spanning a radius of 1.77 m (outer extent of ECAL) up to 2.95 m (inner extent of the magnet coil). An outer hadron calorimeter (HO) is placed outside the solenoid to complement the barrel calorimeter. Beyond  $|\eta| = 3$ , the forward hadron calorimeter (HF) at 11.2 m from the interaction point extend the pseudorapidity coverage to  $|\eta| = 5.2$ .

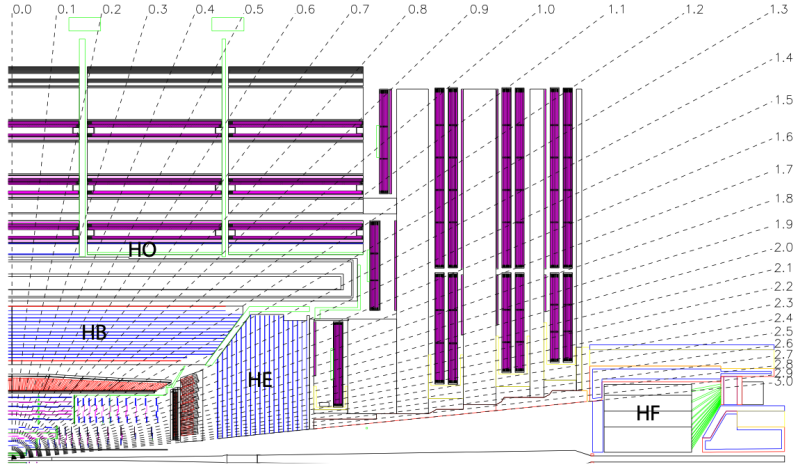


Figure 2.5: Longitudinal view of the CMS detector showing the hadron calorimeter barrel (HB), endcap (HE), outer (HO), and forward (HF) calorimeters from [21].

817     The HB is a sampling calorimeter covering the pseudorapidity range  $|\eta| < 1.3$  [21].  
 818     It consists of 36 identical azimuthal wedges which form two half-barrels (HB+ and HB-  
 819     ), with a segmentation of  $(\Delta\eta, \Delta\phi) = (0.087, 0.087)$ . The HE covers pseudorapidity  
 820      $1.3 < |\eta| < 3$ . The HB and endcap HE calorimeters are sampling calorimeters which  
 821     use brass as the absorber and plastic scintillator as the active material. Light from  
 822     the plastic scintillator is wavelength-shifted and captured in optic fibers which are  
 823     read out by front-end electronics [27].

824     The HF is a Cherenkov calorimeter based on a steel absorber and quartz fibers  
 825     which run longitudinally through the absorber and collect Cherenkov light, primarily  
 826     from the electromagnetic component of showers developed in the calorimeter [27].  
 827     Photomultiplier tubes are used to collect light from the quartz fibers. The HF is  
 828     designed to survive in the harsh radiation conditions and high particle flux of the for-  
 829     ward region. On average, 760 GeV per proton-proton interaction is deposited into the  
 830     two forward calorimeters, compared to only 100 GeV for the rest of the detector [21].  
 831     Furthermore, this energy has a pronounced maximum at the highest rapidities.

832    **2.5.4 Muon detectors**

833    The CMS muon system is designed to have the capability of reconstructing the mo-  
834    mentum and charge of muons over the kinematic range of the LHC, since muons are a  
835    powerful handle on signatures of interesting processes over the high background rate  
836    of the LHC [21]. For instance, the decay of the Standard Model Higgs boson into  
837     $ZZ$ , which in turn decay to 4 leptons, can be reconstructed with high 4-particle mass  
838    resolution if all the leptons are muons, since muons are less affected than electrons  
839    by radiative losses in the tracker material.

840    The muon system consists of a cylindrical barrel section and two planar endcap  
841    regions [21]. The barrel muon detector consists of drift tube (DT) chambers covering  
842    the pseudorapidity region  $|\eta| < 1.2$  (Fig. 2.6). The DTs can be used as tracking  
843    detectors due to the barrel region's characteristic low neutron-induced backgrounds,  
844    low muon rate, and relatively uniform 4T magnetic field contained in the steel yoke.

845    In the two endcap regions, the muon rates and background levels are high and the  
846    magnetic field is large and non-uniform [21]. Here, the muon system uses cathode  
847    strip chambers (CSCs) to identify muons between  $0.9 < |\eta| < 2.4$ . The cathode strips  
848    of each chamber run radially outwards and provide a precision measurement in the  
849     $r - \phi$  bending plane. The anode wires run approximately perpendicular to the strips  
850    and are read out in order to measure  $\eta$  and the beam-crossing time of a muon.

851    In addition to the DT and CSC, a dedicated trigger system consisting of resistive  
852    plate chambers (RPCs) in the barrel and endcap regions provide a fast, independent,  
853    and highly-segmented trigger with a sharp  $p_T$  threshold over a large portion of the  
854    pseudorapidity range ( $|\eta| < 1.6$ ) of the muon system [21]. RPCs have good time  
855    resolution but coarser position resolution compared to the DTs or CSCs. The RPCs  
856    also play a role in resolving ambiguities in reconstructing tracks from multiple hits in  
857    a chamber.

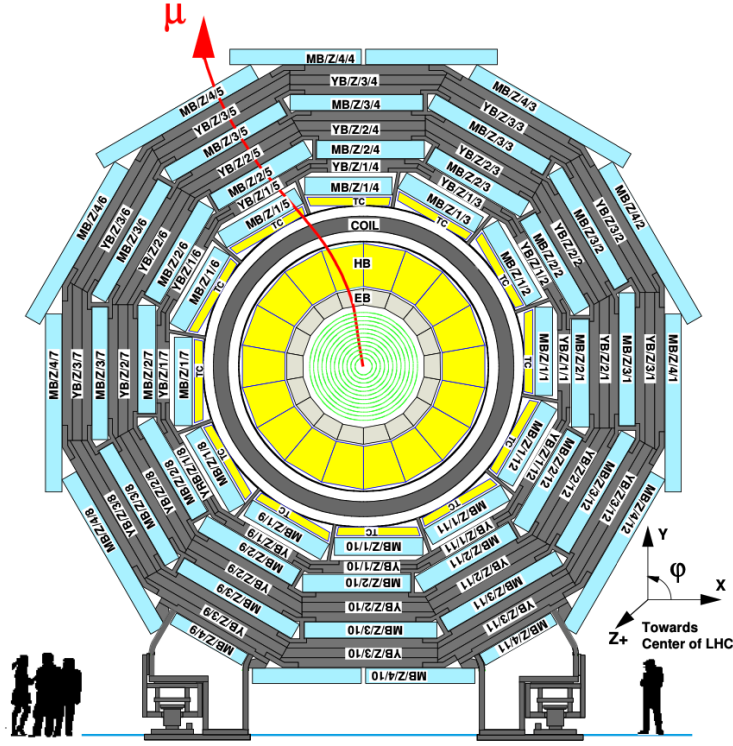


Figure 2.6: Layout of the CMS barrel muon drift tube (DT) chambers in one of the five wheels from [21]. The DTs are organized in 12 sectors of the yoke barrel (YB). In each of the 12 sectors of the yoke, there are 4 muon chambers per wheel (MB1, MB2, MB3, and MB4).

### 2.5.5 The Level-1 Trigger

The design performance of the LHC corresponds to an instantaneous luminosity of  $10^{34} \text{ cm}^{-2} \text{ s}^{-1}$  with a 25 ns bunch crossing rate, giving an average pile-up (number of simultaneous events) of 25 per bunch crossing [28]. However, during Run 2, in 2017 and 2018 the LHC was able to surpass this goal with a mean number of 32 interactions per bunch crossing, and reaching over 50 interactions in short periods (Fig. 2.2). The large number of events from inelastic collisions (minimum bias events) per bunch crossing, combined with the small cross-sections of possible physics discovery signatures, necessitates a sophisticated event selection system for filtering this large event rate, as it is impossible to save all events. This data filtering system is imple-

868 mented by CMS in two stages. The first stage is the Level-1 (L1) Trigger, which is  
 869 deployed in custom electronic hardware systems and is responsible for reducing the  
 870 event rate to around 100 kHz. The second stage is the High-Level Trigger (HLT)  
 871 which is described in Section 2.5.6. This section describes the Phase-1 configuration  
 872 of the Level-1 Trigger.

873 The L1 Trigger data flow of Phase-1 is shown in Fig. 2.7 [28], with organization  
 874 into the L1 calorimeter trigger, the L1 muon trigger, and the L1 Global Trigger (GT).

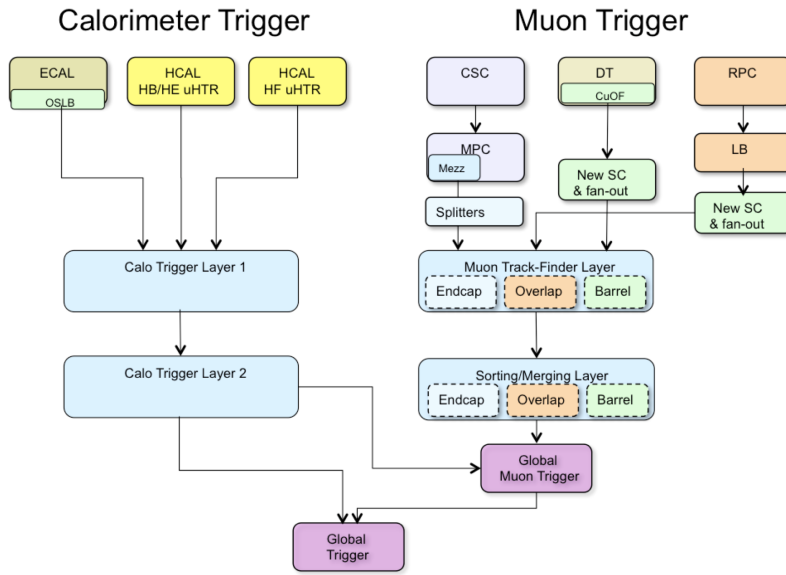


Figure 2.7: Dataflow for the Phase-1 Level-1 Trigger [28], which is implemented in custom hardware and is responsible for reducing the event rate from the LHC bunch crossing frequency of 400 MHz (bunch crossings every 25 ns) to a maximum rate of 100 kHz. In Phase-1, the Level-1 Trigger has access to information from the calorimeter and muon detectors.

875 The L1 calorimeter trigger begins with trigger tower energy sums formed by the  
 876 ECAL, HCAL, and HF Trigger Primitive Generator (TPG) circuits from the indi-  
 877 vidual calorimeter cell energies. In the original configuration, the ECAL energies  
 878 were accompanied by a bit indicating the transverse extent of the electromagnetic  
 879 energy deposits, and the HCAL energies were accompanied by a bit indicating the  
 880 presence of minimum ionizing energy [29]. During Long Shutdowns 1 and 2 (LS1

881 and LS2), HF was upgraded to provide finer granularity information to the trigger,  
882 and the HCAL barrel and endcap front-end electronics were upgraded to provide  
883 high-precision timing information and depth segmentation information.

884 In the original design of the L1 calorimeter trigger, the trigger primitives are pro-  
885 cessed by the Regional Calorimeter Trigger (RCT, upgraded to Calo Layer 1 after  
886 LS2) which finds isolated and non-isolated electron/photon candidates [28]. At this  
887 stage, electrons/photons candidates are treated together since they cannot be defini-  
888 tively distinguished at this stage due to lack of tracking information in the L1 trigger.  
889 The Global Calorimeter Trigger (GCT, upgraded to Calo Layer 2 after LS2) sorts  
890 further the candidate electrons/photons, finds jets (classified as central, forward, and  
891 tau) using the  $E_T$  sums and performs calibration of the clustered jet energies, and  
892 calculates global quantities such as missing  $E_T$ . It sends the top four candidates of  
893 each type to the Global Trigger [28].

894 During LS2 and before Run-2, the legacy calorimeter trigger was upgraded to be  
895 more flexible, maintainable, and performant [30] [31] [32]. These upgrades included  
896 the replacement of legacy VME-based electronics with the microTCA modern tele-  
897 coms standard, and system-wide usage of the latest generation of FPGAs, Xilinx  
898 Virtex 7. Parallel copper links were replaced in almost all cases with serial optical  
899 links, allowing link speeds to increase from 1 Gb/s to 10 Gb/s [30]. A schematic of  
900 the current calorimeter trigger is shown in Fig. 2.8. The calorimeter Layer-1 is imple-  
901 mented in 18 Calorimeter Trigger Processor (CTP7) boards, with each card spanning  
902 4 out of 72 towers in  $\phi$  and all of  $\eta$ . Tower-level operations are performed in Layer-1,  
903 such as the sum of ECAL and HCAL energies, energy calibration, and the compu-  
904 tation of the ratio of HCAL to ECAL energies. The Layer-1 cards each transmit 48  
905 output links at 10 Gb/s to the nine Layer-2 Master Processor cards (MP7) cards,  
906 which host calorimeter algorithms that find particle candidates and compute global  
907 energy sums. Each MP7 takes 72 input links and has access to the whole event at

trigger tower granularity, such that the algorithms are fully pipelined and start processing as soon as the minimum amount of data is received. The trigger candidates are sent to a demultiplexer (demux) board, also a MP7, which formats the data for the upgraded Global Trigger, also called the microGT ( $\mu$ GT).

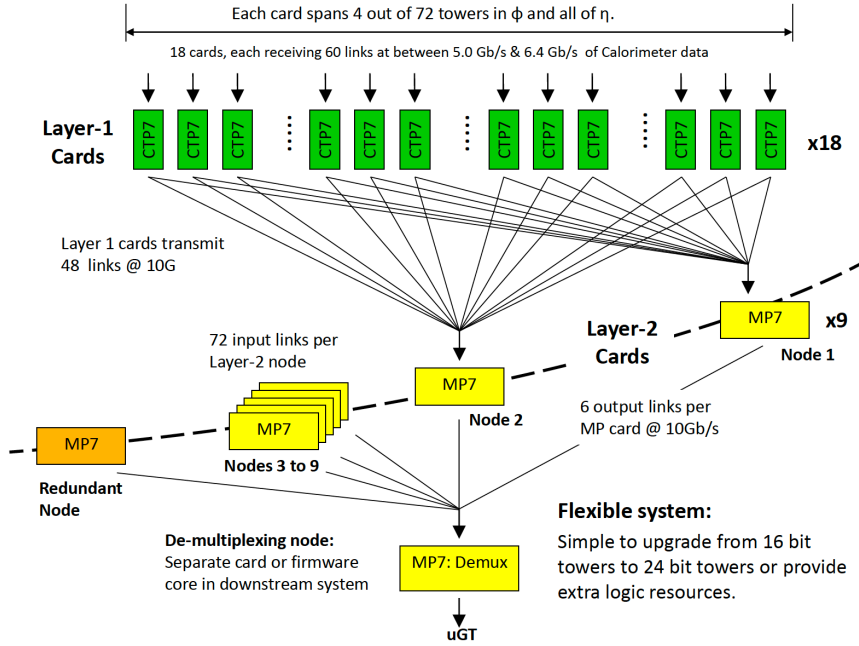


Figure 2.8: Schematic of the calorimeter trigger after Long Shutdown 2 [30]. The Layer-1 calorimeter trigger is implemented in CTP7 cards, which send time-multiplexed outputs to the Layer-2 MP7 cards. The Layer-2 cards handle the data in a round-robin style and the outputs are de-multiplexed, producing one output data stream to the Global Trigger.

Each of the L1 muon triggers has its own trigger logic [29]. The RPC strips are connected to a Pattern Comparator Trigger (PACT), which forms trigger segments that are used to build tracks and calculate  $p_T$ . The RPC logic also provides some hit data to the CSC trigger system to resolve ambiguities caused by two muons in the same CSC. The CSCs form local charged tracks (LCTs) from the cathode strips, which are combined with the anode wire information. LCTs are combined into full muon tracks and assigned  $p_T$  values.

The Global Muon Trigger (GMT) sorts the RPC, DT, and CSC muon tracks,

920 converts these tracks to the same  $\eta$ ,  $\phi$ , and  $p_T$  scale, and validates the muon sign [29].  
921 It improves the trigger efficiency by merging muon candidates that were detected  
922 in two complementary sub-systems (i.e. DT+RPC, or CSC+RPC). The GMT also  
923 contains logic to correlate the found muon tracks with an  $\eta-\phi$  grid of quiet calorimeter  
924 towers to determine if the muons are isolated, as well as logic to remove duplicate  
925 candidates originating in the overlap regions from both DT and CSC systems. The  
926 final collection of muons are sorted based on their initial quality, correlation, and  $p_T$ ,  
927 and the top four muons are sent to the Global Trigger [29].

928 The Global Trigger (GT) receives information from the GCT and GMT, and  
929 makes the Level-1 Accept (L1A) decision to either discard or accept the bunch cross-  
930 ing [29]. This is accomplished by sorting ranked trigger objects that are accompanied  
931 by positional information in  $\eta$  and  $\phi$ , permitting the trigger to applying criteria with  
932 thresholds that can vary based on the location of the trigger objects, and/or to re-  
933 quire trigger objects to be close to or opposite from each other. The GT L1A decision  
934 arrives at the detector front end with a  $3.8\ \mu\text{s}$  latency after the interaction at a rate  
935 which is required to be less than 100 kHz, and triggers a full readout of the detector  
936 for further processing.

### 937 **2.5.6 The High-Level Trigger**

938 The HLT is implemented in software running on a large computer farm of fast com-  
939 mercial processors [33] [34]. The algorithms in HLT have access to full data from  
940 all CMS sub-detectors, including the tracker, with full granularity and resolution.  
941 The HLT reconstruction software is similar to what is used offline for full CMS data  
942 analysis. As a result, the HLT can calculate quantities with a resolution compara-  
943 ble to the final detector resolution, compared to the L1 Trigger. The HLT performs  
944 more computationally-intensive algorithms, such as combining tau-jet candidates in  
945 the calorimeter with high- $p_T$  stubs in the tracker, to form a hadronic tau trigger. The

946 maximum HLT input rate from the L1 Trigger is 100 kHz, and the HLT output rate  
947 is approximately 100 Hz.

948 The HLT contains trigger paths, each corresponding to a dedicated trigger [35].  
949 A path consists of several steps implemented as software modules. Each HLT trigger  
950 path must be seeded by one or more L1 trigger bits: the first module always looks  
951 for a L1 seed, consisting of L1 bit(s) and L1 object(s). Each module performs a well-  
952 defined task such as unpacking (raw to digitized quantities), reconstruction of physics  
953 objects (electrons, muons, jet, missing transverse energy, etc.), making intermediate  
954 decisions that trigger more detailed reconstruction modules, and calculating the final  
955 decision for the trigger path. If an intermediate filter decision is negative, the rest of  
956 the path is not executed, and the trigger rejects the event.

### 957 **2.5.7 Particle reconstruction**

958 To build a description of the physics objects present in the particle collision, the  
959 basic elements from the detector layers (tracks and clusters of energy) are correlated  
960 to identify each particle in the final state. Measurements from different sub-detectors  
961 are combined to reconstruct the particle properties. This approach is called particle-  
962 flow (PF) reconstruction [22]. Key to the success of the PF reconstruction is the  
963 fine spatial granularity of the detector layers. Coarse-grained detectors can cause  
964 the signals from different particles to merge, especially within jets. However, if the  
965 subdetectors are sufficiently segmented to separate individual particles, it becomes  
966 possible to produce a global event description that identifies all physics objects with  
967 high efficiencies and resolution.

### 968 **2.5.8 Data storage and computational infrastructure**

969 The LHC generates over 15 petabytes (15 million gigabytes) of data every year, neces-  
970 sitating a flexible computing system that can be accessed by researchers working at

971 the four main LHC experiments: ALICE, ATLAS, CMS, and LHCb. The Worldwide  
972 LHC Computing Grid (WLCG) [36] is a global collaboration of computer centers that  
973 links thousands of computers and storage systems in over 170 centers across 41 coun-  
974 tries. These centers are arranged in “tiers”, and provide near real-time access to users  
975 processing, analyzing, and storing LHC data. One of the final stages of data analy-  
976 sis at LHC experiments is large-scale data processing taking place over distributing  
977 computing, for instance, with the use of Condor [37], a distributed, scalable, flexible  
978 batch processing system which accepts a computing job, allocates a resource to it,  
979 executes it, and returns the result back to a user transparently.

980 **Chapter 3**

981 **The Phase-2 Upgrade of CMS**

982 This chapter gives an overview of the High-Luminosity LHC upgrade of the LHC in  
983 Section 3.1, and the upgrades for the Phase-2 CMS Level-1 (L1) Trigger in Section  
984 3.2. One of the major upgrades is the new availability of calorimeter crystal-level  
985 information to the L1 calorimeter trigger, compared to the current trigger which only  
986 has access to tower-level information (a tower being 5 by 5 in crystals). To capitalize  
987 on the increased spatial granularity of this information, an upgraded algorithm is  
988 presented which reconstructs and identifies electron and photon candidates in the the  
989 Layer-1 Calorimeter Trigger. A description of the algorithm and a validation of its  
990 performance in Phase-2 conditions is given in Section 3.3.

991 **3.1 The High-Luminosity LHC**

992 In order to sustain and extend the LHC’s physics discovery program and maintain  
993 operability for a decade or more, the LHC is undergoing a major upgrade to the High-  
994 Luminosity LHC (HL-LHC). In its final configuration, the HL-LHC will deliver a peak  
995 luminosity of  $7.5 \times 10^{34} \text{ cm}^{-2} \text{ s}^{-1}$ , potentially leading to total integrated luminosity  
996 of  $4000 \text{ fb}^{-1}$  after ten years of operations, scheduled to begin in 2027 [38]. This  
997 integrated luminosity is about ten times the predicted luminosity reach of the LHC

998 in its initial configuration. To enable the CMS experiment to continue operations and  
999 data-taking and to maximize the discovery potential of the unprecedented amount  
1000 of data, the CMS detector is undergoing Phase-2 upgrades in order to perform high-  
1001 precision measurements and searches for physics beyond the Standard Model in the  
1002 intense running conditions of the HL-LHC.

## 1003 **3.2 The Phase-2 Level-1 Trigger**

1004 To achieve the goals of the HL-LHC program and to ensure the collection of information-  
1005 rich datasets in the HL-LHC, the Phase-2 upgrade of the CMS Level-1 Trigger [38]  
1006 must be upgraded in conjunction with the CMS sub-detectors and their readouts, to  
1007 maintain physics selectivity. The HL-LHC will produce an intense hadronic environ-  
1008 ment corresponding to 200 simultaneous collisions per beam crossing, necessitating  
1009 comprehensive upgrades of the trigger system outlined below.

1010 In order to cope with the increased pile-up and high occupancies of the HL-LHC,  
1011 the latency of the L1 trigger system (time available to produce a L1 Accept signal) will  
1012 be increased significantly from  $3.8 \mu\text{s}$  to  $12.5 \mu\text{s}$ , with an increased maximum output  
1013 bandwidth of 750 kHz [38]. With the increased latency, in addition to information  
1014 from calorimeters and muon detectors (as in the Phase-1 system), information from  
1015 the new tracker and high-granularity endcap calorimeter can also be included at L1  
1016 for the first time. This is illustrated in the functional diagram of the architecture of  
1017 the Phase-2 trigger system in Fig. 3.1.

1018 The key feature of the Phase-2 L1 Trigger is the introduction of a correlator layer,  
1019 where algorithms produce higher-level trigger objects by combining information from  
1020 sub-detectors, with a selectivity approaching that of offline reconstruction in the  
1021 HLT [38]. Four independent data processing paths (grouped together in Fig. 3.1) are  
1022 implemented: tracking, calorimetry, muon systems, and particle-flow techniques:

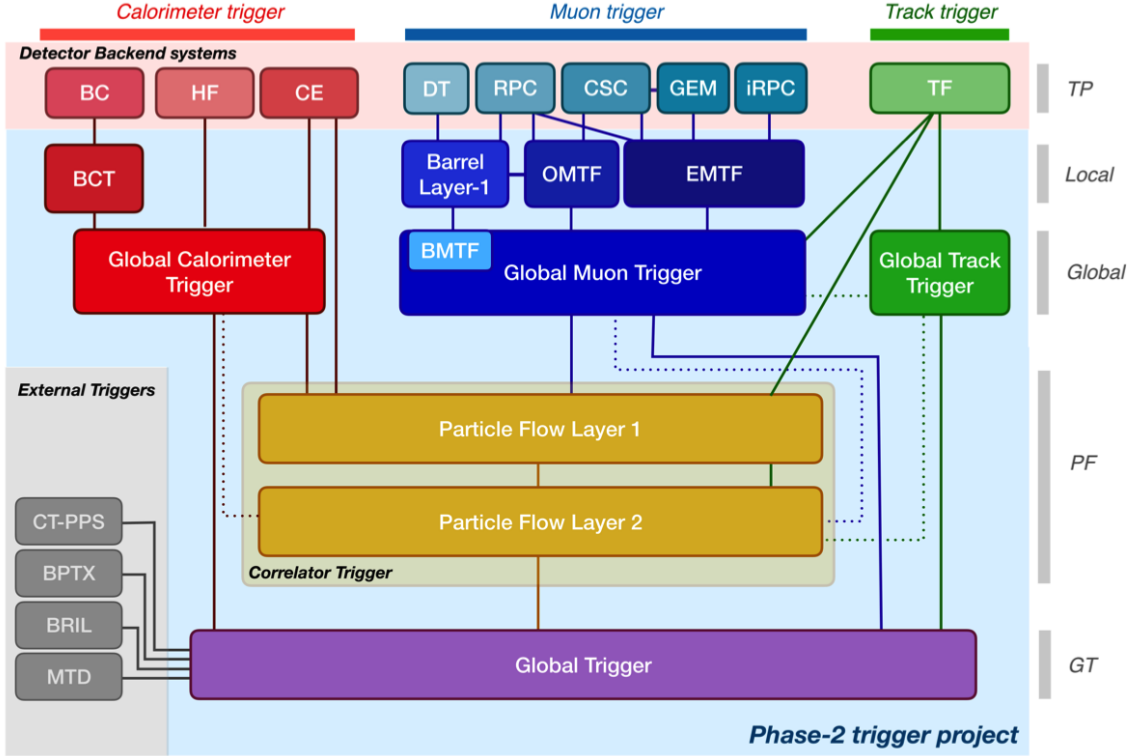


Figure 3.1: Functional diagram of the CMS L1 Phase-2 upgraded trigger design [38], showing the four trigger paths: calorimeter, muon, track, and Particle Flow. For the first time, tracking information will be available as early as the L1 Trigger.

- 1023     • **Calorimeter Trigger path:** (red, Fig. 3.1) A barrel calorimeter trigger (BCT)  
 1024       and the HGCAL backend are used to process crystal-level information from the  
 1025       calorimeters to produce high-resolution clusters and identification variables used  
 1026       for later processing. Outputs from the BCT, HGCAL, and the HF are sent to  
 1027       a global calorimeter trigger (GCT), where calorimeter-only objects such as  $e/\gamma$   
 1028       candidates, hadronically decaying tau lepton candidates, jets, and energy sums  
 1029       are built.
- 1030     • **Track Trigger path:** (green, Fig. 3.1) Tracks from the Outer Tracker are  
 1031       reconstructed in the track finder (TF) processors as part of the detector back-  
 1032       end. A global track trigger (GTT) will reconstruct the primary vertices of the  
 1033       event, along with tracker-only based objects, such as jets and missing transverse  
 1034       momentum.

- **Muon Trigger path:** (*blue*, Fig. 3.1) Trigger primitives are processed by muon track finder algorithms, again separated into the barrel (barrel muon track finder, BMTF), overlap (overlap muon track finder, OMTF), and endcap (endcap muon track finder, EMTF). Standalone muons and stubs containing information such as position, bend angle, and timing, as well as L1 tracks, are sent to the global muon trigger (GMT).
- **Particle-Flow Trigger path:** (*yellow*, Fig. 3.1) The correlator trigger (CT) aims to approach the performance of offline Particle Flow, and is implemented in two layers. “Layer-1” produces the particle-flow candidates from matching calorimeter clusters and tracks. “Layer 2” builds and sorts final trigger objects and applies additional identification and isolation criteria.

The outputs from the above trigger paths are combined in the Global Trigger (GT) (*purple*, Fig. 3.1), which calculates the final trigger decision (Level-1 Accept), transmitting it to the Trigger Control and Distribution System (TCDS), which distributes it to the detector backend systems, initiating the readout to the DAQ. The GT also provides the interface to external triggers (*grey*, Fig. 3.1), such as triggers for the precision proton spectrometer (PPS), beam position and timing monitors (BPTX), and luminosity and beam monitoring (BRIL) detectors [38]. The design of the Phase-2 Level-1 Trigger allows for future inclusion of triggering information, for instance information about minimum ionizing particles (MIPs) from the MIP Timing Detector (MTD) [39].

### **3.3 Standalone Barrel Calorimeter electron/photon reconstruction**

The reconstruction and identification of electrons and photons ( $e/\gamma$ ) begin with the trigger primitives of the barrel ECAL and HCAL detectors and endcap HGCAL calorimeters, covering the pseudorapidity region  $|\eta| < 3$ . The barrel and endcap regions of the detector are intrinsically different enough to warrant different approaches to  $e/\gamma$  reconstruction. This work presents a firmware-based emulator for the standalone  $e/\gamma$  reconstruction in the barrel calorimeter (Fig. 3.2). “Standalone” refers to the fact that the tracker information is not used in this particular reconstruction chain. This firmware-based emulator is based on the parallelized, computational logic that will be deployed in the firmware of the Phase-2 Level-1 trigger. The emulator uses fixed-precision integers to represent all values, such as in the computation of cluster energies, and closely mimics the firmware logic which uses arrays and performs computations in flattened loops. It represents an improved, more realistic understanding of the trigger, compared to the previous emulator which used idealized logic such as vector operations, and floats to represent all values [38].

#### **3.3.1 Electron/photon standalone barrel procedure**

In Phase-2, the upgrade of both on-detector and off-detector electronics of the barrel calorimeters’ trigger primitive generator (TPG) will enable the streaming of single crystal data from the on-detector to the backend electronics. Currently in Phase-1, the ECAL and HCAL TPGs is restricted to providing lower-granularity information of trigger tower sums of  $5 \times 5$  crystals to the Level-1 Trigger [38]. A schematic of the geometry of the ECAL barrel in the Phase-2 Regional Calorimeter Trigger (RCT) is shown in Fig. 3.3. The barrel is spanned by 36 RCT cards, each spanning  $17 \times 4$  towers in  $\eta \times \phi$ . Each RCT card is subdivided into five “regions” as shown in Fig.

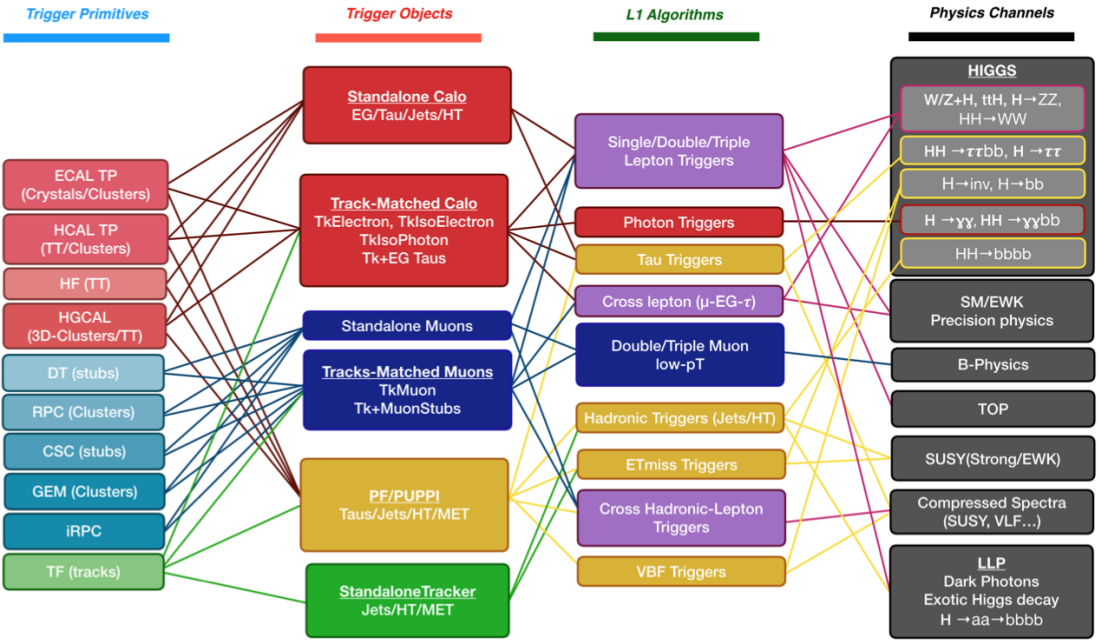


Figure 3.2: Summary of the links between the trigger primitives (*first column*), the trigger objects (*second column*), the Level-1 algorithms used in the menu (*3rd column*), and the physics channels (*4th column*), from [38], where a full description of the Phase-2 L1 algorithms can be found. This work focuses on developments for the Standalone Calorimeter electron and photon ("EG") reconstruction algorithm.

1081     3.4. After initial clustering and processing, the outputs of the RCT card are sent to  
 1082     the Global Calorimeter (GCT) trigger, which is processed in three cards as shown in  
 1083     Fig. 3.5. The reconstruction algorithm is detailed below.

1084     The standalone barrel algorithm for reconstructing and identifying electrons and  
 1085     photons in the Phase-2 Level-1 Trigger takes as input the digitized response of each  
 1086     crystal of the barrel ECAL, with a granularity  $0.0175 \times 0.0175$  in  $\eta \times \phi$ , which is 25  
 1087     times higher than the input to the Phase-1 trigger, which consisted of trigger towers  
 1088     with a granularity of  $0.0875 \times 0.0875$ . In HCAL the tower size of  $0.0875 \times 0.0875$   
 1089     is unchanged. The trigger algorithm is designed to closely reproduce the algorithm  
 1090     used in the offline reconstruction, with limitations and simplifications due to trigger  
 1091     latency.

1092     In the RCT, an initial requirement of  $p_T > 0.5$  GeV is imposed on the input

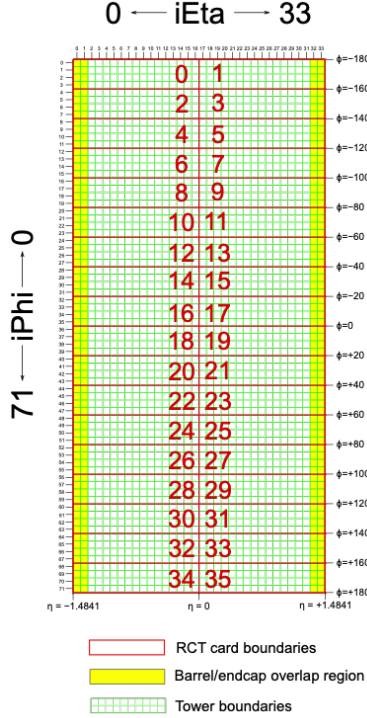


Figure 3.3: Schematic of the geometry of the Phase-2 ECAL barrel in the Regional Calorimeter Trigger (RCT), showing the division of the barrel region into 36 Regional Calorimeter Trigger (RCT) cards (*red*). Each card spans  $17 \times 4$  towers in  $\eta \times \phi$  (*green*), and each tower is  $5 \times 5$  in single crystals in  $\eta \times \phi$ . Towers in the overlap region (*shaded yellow*) are read out to both the barrel and endcap.

trigger primitives (i.e. energies from the ECAL crystals and HCAL towers) to reject contribution from pile-up. In one of the regions inside a RCT card (Fig. 3.4), the crystal containing the highest energy deposit is identified as the seed crystal, as shown in Fig. 3.6. The energy in the crystals in a window of size  $3 \times 5$  in  $\eta \times \phi$  around the seed cluster is added into a cluster. The energy is considered “clustered”. The process is repeated with the remaining “unclustered” energy, until up to four clusters are produced in the region.

To improve  $e/\gamma$  identification and to reduce background contributions, identification and reconstruction algorithms are implemented at this stage:

- Shower shape: The energy deposit sums around the seed crystal is computed in windows of size  $2 \times 5$  and  $5 \times 5$  (Fig. 3.6, *dashed lines*), with true  $e/\gamma$  clusters

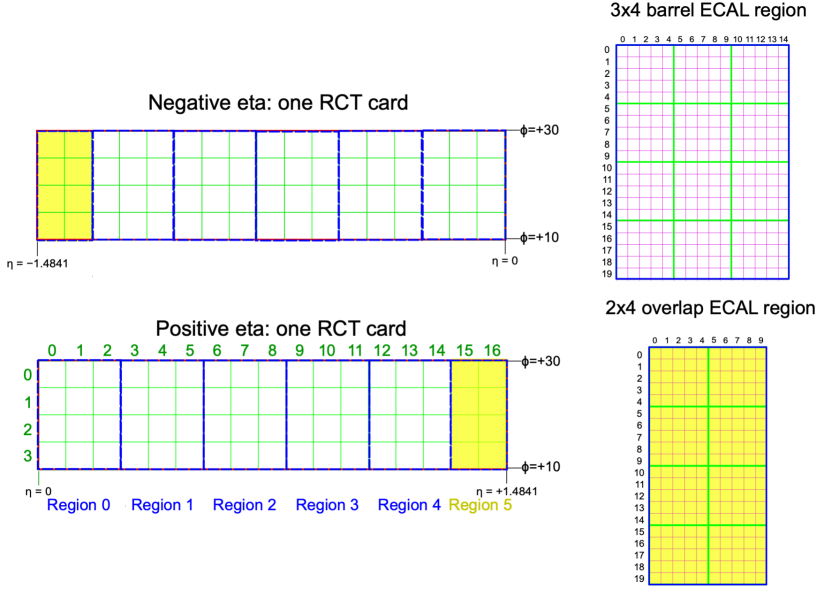


Figure 3.4: Schematic of two example RCT cards in the negative eta (*top left*) and positive eta (*bottom left*) regions of the ECAL barrel. Each RCT card is divided into six regions: five regions are of size  $3 \times 4$  towers in  $\eta \times \phi$  (*top right*), and a sixth smaller overlap region of size  $2 \times 4$  towers (*bottom right*). Each tower is  $5 \times 5$  ( $\eta \times \phi$ ) in crystals.

1104 tending to produce showers that deposit most of their energy in a  $2 \times 5$  region.

- 1105 • Bremsstrahlung recovery:  $e/\gamma$  tend to spread in the  $\phi$  direction due to charged  
 1106 particles being bent by the magnetic field of the CMS solenoid. If sufficient  
 1107 energy comparable to the core  $3 \times 5$  cluster is found in the adjacent  $3 \times 5$   
 1108 windows (Fig. 3.6, *shaded yellow*), the energy is added to the core cluster and  
 1109 no longer considered unclustered energy.

1110 After parallel processing in the regions, the clusters in a RCT card are stitched  
 1111 together if they are located directly along the borders of a region (Fig. 3.3). The  
 1112 remaining unclustered ECAL energy is summed into ECAL towers.

1113 From each RCT card, the twelve highest-energy clusters, as well as any remaining  
 1114 unclustered energy, are sent to the GCT. Since each GCT card has information from  
 1115 sixteen RCT cards (Fig. 3.5), final stitching across the boundaries of the RCT cards  
 1116 is performed. One more identification algorithm is performed at this stage:

## GCT/“Layer 2”

 : one GCT card

 : area that is unique to the GCT card

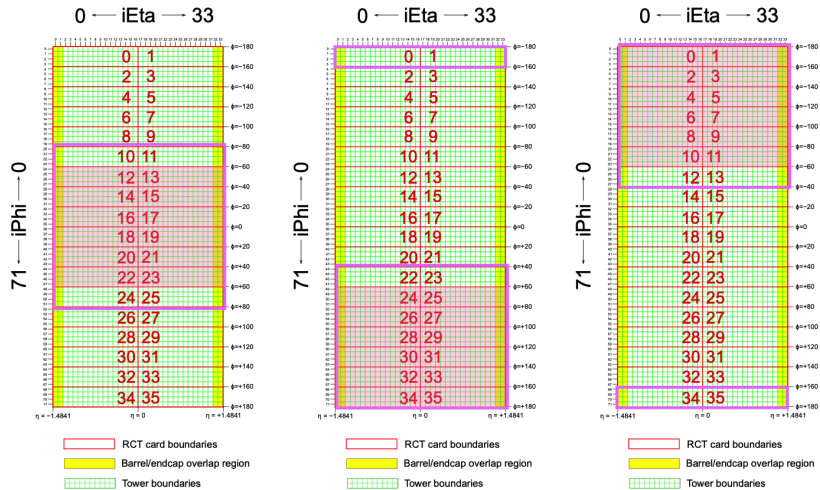


Figure 3.5: Schematic of the Phase-2 ECAL barrel in the Global Calorimeter Trigger (GCT), which will process the outputs of the Regional Calorimeter Trigger (RCT) in three GCT cards (*purple borders*). Each card in the GCT processes the equivalent of sixteen RCT cards, with the center twelve RCT cards being unique to that GCT card (*shaded pink*), and the remaining four RCT cards overlapping with one other GCT card.

- 1117     • Isolation: One handle to reject backgrounds from e.g. pile-up, comes from the
- 1118        tendency for background to be spread more uniformly across a large area in the
- 1119        detector, whereas genuine  $e/\gamma$  are expected to produce showers concentrated in
- 1120        the  $3 \times 5$  crystal window. The energy sum in a large window of  $7 \times 7$  in towers
- 1121        is computed and used to reject background.

1122 Flags that provide discrimination power between genuine  $e/\gamma$  and background, are  
 1123 computed using the relative isolation and shower shape quantities. The standalone  
 1124 working point (WP) is defined as the logical OR of the relative isolation and shower  
 1125 shape flags.

1126        The information of the clusters in the event, including their energies, crystal-level  
 1127 position, the relative isolation flag, the shower shape flag, the standalone WP, and  
 1128 the ratio of the HCAL over ECAL energies, are sent in 64 bits to the Correlator  
 1129 Trigger and the Global Trigger. The towers in the event are computed as the sum  
 1130 of all unclustered energy in the ECAL with the corresponding HCAL energy at each

### 3x4 barrel ECAL region

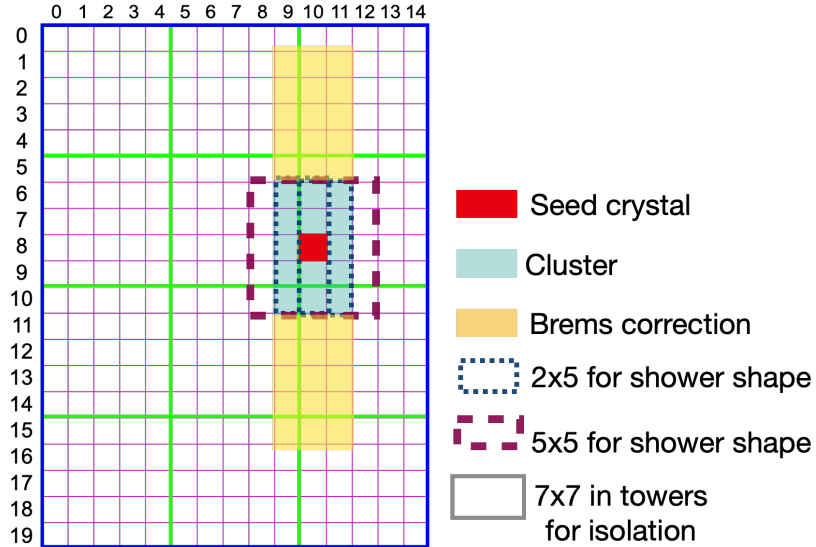


Figure 3.6: Illustration of an example electron/photon ( $e/\gamma$ ) cluster in the Phase-2 Level-1 Trigger standalone barrel  $e/\gamma$  reconstruction, in a region of  $15 \times 20$  crystals ( $3 \times 4$  towers) in  $\eta \times \phi$ . Each small pink square is one crystal, the highest-granularity ECAL trigger primitives available to the L1 Trigger in Phase-2. The core cluster consists of the energy sum in a  $3 \times 5$  window of crystals (*shaded light blue*), centered around the seed crystal (*red*). The presence of energy lost to bremsstrahlung radiation is checked in the adjacent  $3 \times 5$  windows in the  $\phi$  direction (*shaded light yellow*). The ratio of the total energies in windows of size  $2 \times 5$  and  $5 \times 5$  in crystals (*dashed dark blue and dark red*) around the seed crystal, is computed and compared to the core cluster energy to obtain shower shape flags. Lastly, the isolation, defined as the sum of the energy in a large window of size  $7 \times 7$  in towers (not shown in figure) is computed, and compared to the core cluster energy to obtain isolation flags.

<sup>1131</sup> tower location, and their energies are sent to the Correlator Trigger.

#### <sup>1132</sup> 3.3.2 Electron/photon standalone barrel results

<sup>1133</sup> The performance of the current emulator of the standalone barrel  $e/\gamma$  algorithm in  
<sup>1134</sup> Phase-2 conditions is quantified in efficiencies and rates. Efficiency is the fraction of  
<sup>1135</sup> true electrons that the algorithm can reconstruct and identify, and is evaluated in  
<sup>1136</sup> a Monte Carlo simulated sample containing electrons with transverse momentum  $p_T$   
<sup>1137</sup> ranging from 1 to 100 GeV. The efficiencies of the current and previous emulators as

1138 a function of the electron generator-level  $p_T$  are shown in Fig. 3.7.

1139 The rates are the event rates that this reconstruction and identification algorithm  
1140 would obtain if it were deployed in a trigger, assuming that proton-proton collisions  
1141 are occurring at the 40 MHz event rate of the HL-LHC. The rate is reported as a  
1142 function of the minimum energy threshold required by the trigger, and is estimated  
1143 using a simulated sample of minimum bias events, i.e. generic proton-proton colli-  
1144 sions without any specific physics selections. The rates for the current and previous  
1145 emulator are shown in Fig. 3.8.

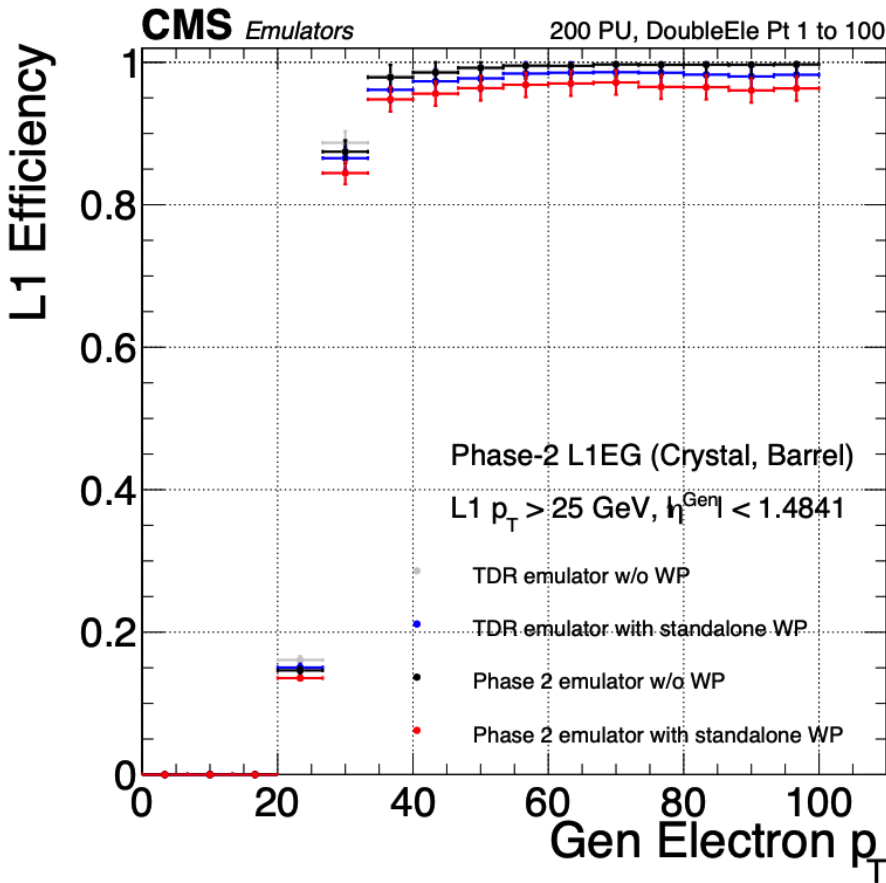


Figure 3.7: Efficiencies of the current and previous emulators of the standalone barrel  $e/\gamma$  algorithm for the Phase-2 Level-1 Trigger, evaluated in a simulated sample containing electrons, as a function of the electron's generator-level transverse momentum  $p_T$ . The standalone working point (WP) is defined as the logical OR of the isolation flag and shower shape flag. The efficiencies with and without requiring the standalone WP, are shown for the current emulator (labeled “Phase 2”, *black, red*) and the previous emulator (labeled “TDR”, *dark blue, grey*).

1146        The current emulator is incorporated into the full Phase-2 L1 menu, allowing an  
1147        estimate of the rates produced by the standalone  $e/\gamma$  barrel trigger path and all  
1148        other algorithms in the L1 Trigger. All rates are estimated with the assumption of  
1149        an average pile-up of 200 and event rate of 40 MHz. The standalone working point  
1150        single  $e/\gamma$  path with requirements on the  $e/\gamma$  candidate to have  $|\eta| < 2.4$ , offline  $p_T$   
1151        to be greater than 51 GeV, and online  $p_T$  to be greater than 41 GeV, is projected to  
1152        have a rate of around 23 kHz. The standalone working point double  $e/\gamma$  path with  
1153        requirements on the two  $e/\gamma$  candidates to have  $|\eta| < 2.4$ , offline  $p_T$  greater than 37  
1154        and 24 GeV, and online  $p_T$  greater than 29 and 18 GeV, is projected to give a rate of  
1155        around 6 kHz. For both paths, the objects efficiency plateau is 99%.

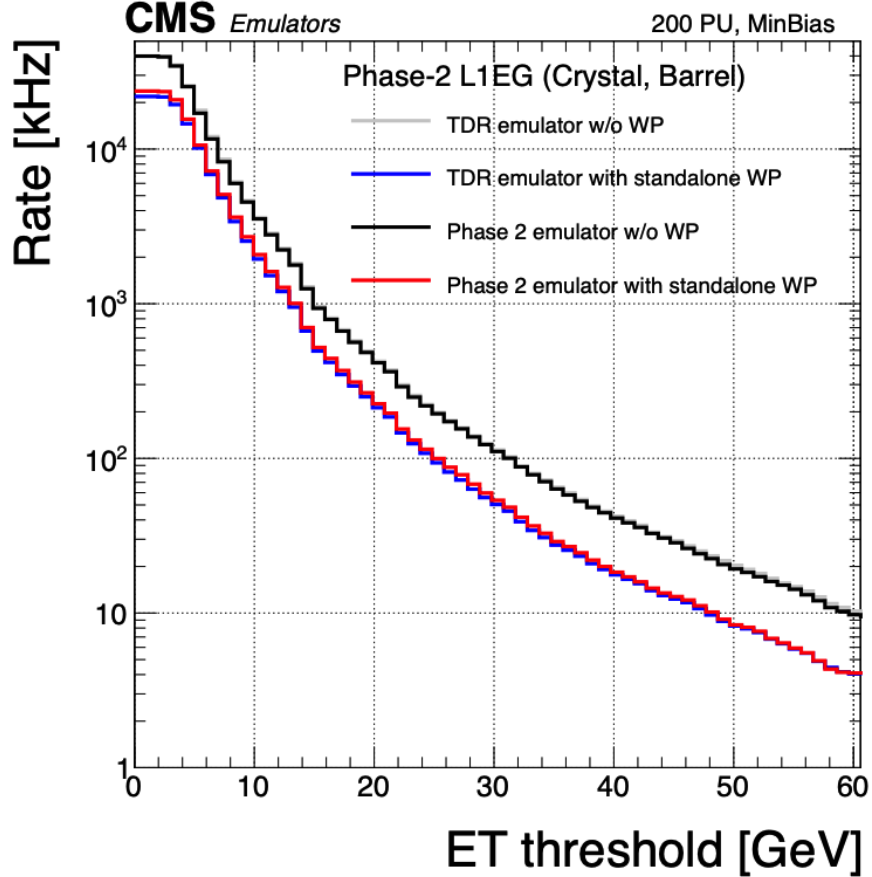


Figure 3.8: Rates in kHz of the current Phase-2 and previous (“TDR”) emulators of the standalone barrel  $e/\gamma$  algorithm for the Phase-2 Level-1 Trigger, evaluated on a minimum bias (MinBias) sample with 200 pile-up (PU), measured as a function of the minimum energy ( $E_T$ ) required of the reconstructed  $e/\gamma$  object in each event. The standalone working point (standalone WP) is defined to be the logical OR of the isolation flag and the shower shape flag. The rates with and without requiring the standalone WP, are shown for the current emulator (labeled “Phase 2”, *black, red*) and the previous emulator (labeled “TDR”, *dark blue, grey*).

1156 **Chapter 4**

1157 **Datasets and Monte Carlo samples**

1158 The search for the exotic decay of the 125 GeV Higgs boson to two light neutral scalars  
1159 decaying to a pair of bottom quarks and a pair of tau leptons ( $h \rightarrow aa \rightarrow bb\tau\tau$ ) is  
1160 based on proton-proton collision data at a center-of-mass energy 13 TeV collected  
1161 in Run-2 of data-taking, spanning the data-taking years 2016, 2017, and 2018. The  
1162 datasets used and the triggers used to collect the data are described in Section 4.1.  
1163 Section 4.2 describes the Monte Carlo simulated samples that are used to model the  
1164  $h \rightarrow aa \rightarrow bb\tau\tau$  signal and background Standard Model processes. Lastly, in order  
1165 to obtain a better description of Standard Model backgrounds that contain two tau  
1166 leptons, a data-Monte Carlo hybrid technique is used to generate embedded samples  
1167 which model processes with genuine  $\tau\tau$  in the final state, as detailed in Section 4.3.

1168 **4.1 Datasets used**

1169 The  $h \rightarrow aa \rightarrow bb\tau\tau$  analysis [40] is based on proton-proton collision data at a center-  
1170 of-mass energy of 13 TeV collected in full Run-2 (2016-18) with the CMS detector.  
1171 The data analyzed corresponds to a total integrated luminosity of  $138 \text{ fb}^{-1}$  ( $36.33 \text{ fb}^{-1}$   
1172 for 2016,  $41.53 \text{ fb}^{-1}$  for 2017, and  $59.74 \text{ fb}^{-1}$  for 2018) [41] [42] [43]. The cumulative  
1173 delivered and recorded luminosity versus time for 2015-2018 is shown in Fig. 4.1.

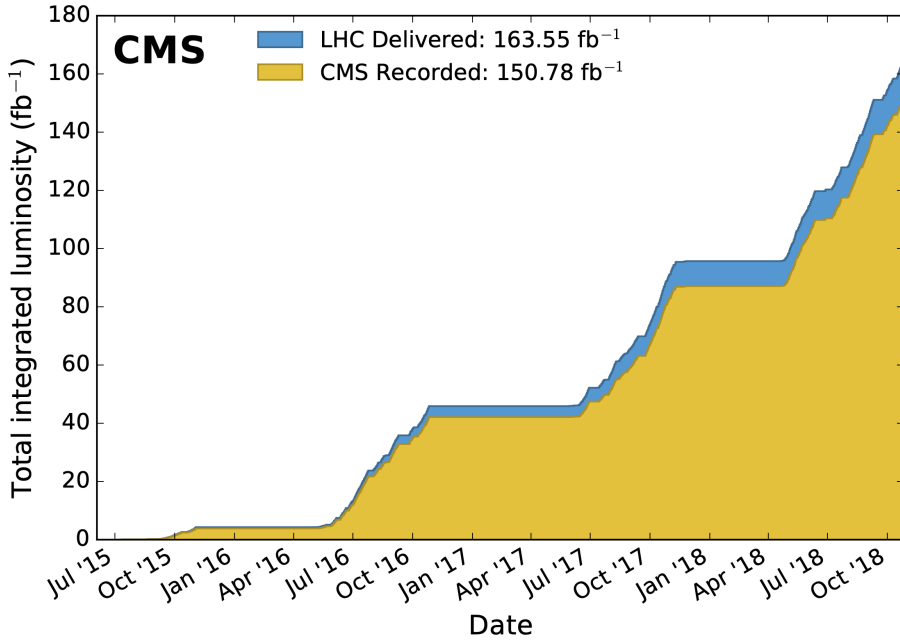


Figure 4.1: Cumulative delivered and recorded luminosity versus time for 2015-2018 at CMS, in proton-proton collision data only, at nominal center-of-mass energy [44].

1174 Data collected with the single muon trigger is used for the  $\mu\tau_h$  channel. For the  
 1175  $e\tau_h$  channel, data collected with the single electron trigger is used; and for the  $e\mu$   
 1176 channel, data collected with the electron + muon trigger is used. A more in-depth  
 1177 discussion of the triggers used follows in a later section.

1178 A full list of samples used can be found in the full documentation [45] [40].

## 1179 4.2 Monte Carlo samples

1180 Modeling and computing observables originating from arbitrary physics processes at  
 1181 the tree level and at next-to-leading order (NLO) is performed by Monte Carlo (MC)  
 1182 event generators, such as Powheg and MadGraph5\\_amCNLO [46] [47]. The informa-  
 1183 tion generated, e.g. the computation of the differential cross sections and kinematics  
 1184 of the final state particles, is saved in a compressed file and used to generate MC sam-

1185    ples that are used in physics analyses. The samples are digitized using GEANT4 [48],  
1186    a platform used at the LHC and other facilities to comprehensively simulate the pas-  
1187    sage of particles through matter. The digitized samples are passed through the same  
1188    detector reconstruction as real data events collected in the detector.

1189    The samples for modeling the signal ( $h \rightarrow aa \rightarrow 2b2\tau$  and  $h \rightarrow a_1a_2$ ) in the  
1190    2HDM+S and TRSM are generated at tree-level, for a range of masses of the light  
1191    neutral scalar  $a$ . For  $h \rightarrow aa$ , the mass hypotheses for the  $a$  range from  $m_a =$   
1192    (12 GeV, 62.5 GeV). For  $h \rightarrow a_1a_2$ , the mass hypotheses for the two light scalars span  
1193    combinations of  $m_{a1}$ ,  $m_{a2}$  ranging from (12 GeV, 62.5 GeV) for the two scalars.

### 1194    4.3 Embedded samples

1195    An important background for Higgs boson studies and searches for additional Higgs  
1196    bosons is the decay of  $Z$  bosons into pairs of  $\tau$  leptons ( $Z \rightarrow \tau\tau$ ). An embedded tech-  
1197    nique was developed in the context of Standard Model Higgs to  $\tau\tau$  measurements, to  
1198    model  $Z \rightarrow \tau\tau$  decays, and was expanded to also model all Standard Model processes  
1199    that contain  $\tau\tau$  [49]. The embedded technique has since been used successfully at  
1200    CMS for the Standard Model  $H \rightarrow \tau\tau$  measurement, as well as searches for minimal  
1201    supersymmetric extensions to the Standard Model (MSSM) [50] [51].

1202    Fig. 4.2 shows a schematic of how embedded samples are produced. Data events  
1203    containing  $Z \rightarrow \mu\mu$  decays are selected. In these events, all energy deposits of the  
1204    recorded muons are removed, and are replaced with simulated tau leptons with the  
1205    same kinematic properties as the removed muons. This results in a hybrid data format  
1206    containing information from both observed and simulated events, as illustrated in Fig.  
1207    4.2 [49].

1208    In the selection step of the embedded technique, events are selected with at least  
1209    one of a set of  $\mu\mu$  trigger paths, which require  $p_T > 17(8)$  GeV for the leading

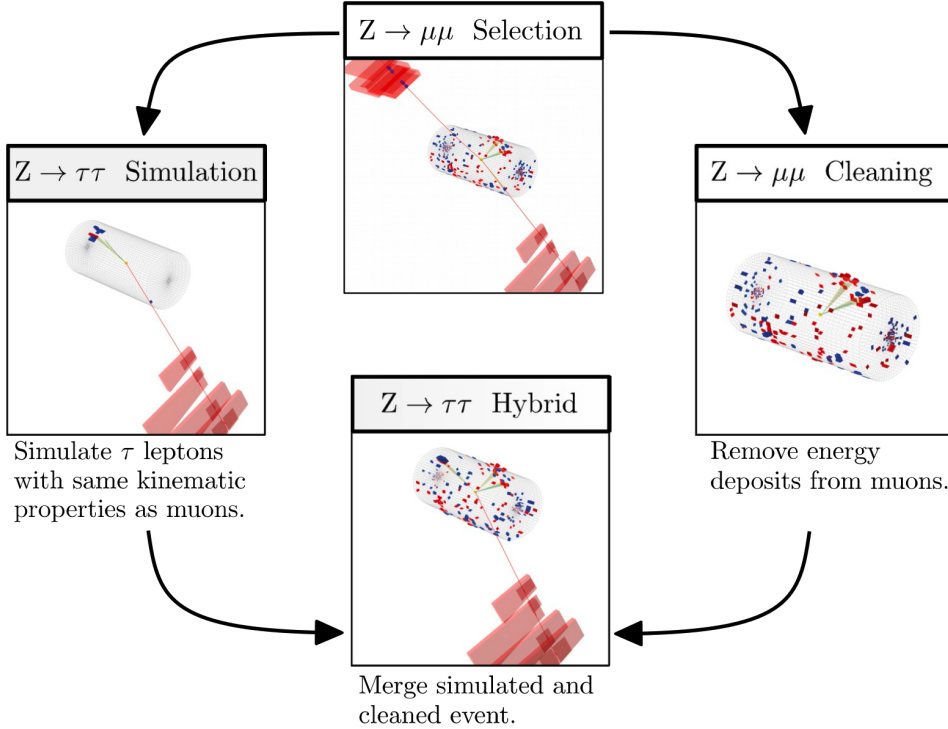


Figure 4.2: Schematic view of the four main steps of the embedding technique for  $\tau$  leptons, as described in Section 4.3 [49]. A  $Z \rightarrow \mu\mu$  event is selected in data ( $Z \rightarrow \mu\mu$  selection), all of the energy deposits associated with the muons are removed ( $Z \rightarrow \mu\mu$  cleaning), and two  $\tau$  leptons and their decays are simulated in an empty detector ( $Z \rightarrow \tau\tau$  simulation). Lastly, all energy deposits of the simulated  $\tau$  decays are combined with the data event ( $Z \rightarrow \tau\tau$  hybrid).

(sub-leading) muons, and a minimum requirement between 3.8 and 8.0 GeV on the invariant di-muon mass  $m_{\mu\mu}$  [49]. The offline reconstructed muons must match the objects at trigger level and also have offline  $p_T > 17(8)$  GeV. They must have  $|\eta| < 2.4$  and be located at a distance  $|d_z| < 0.2$  cm to the primary vertex along the beam axis. To form a  $Z$  boson candidate, each muon is required to originate from a global muon track. The muon pairs must have opposite charges with an invariant mass of  $m_{\mu\mu} > 20$  GeV. If more than two di-muon pairs are found, the pair with the invariant mass closest to the  $Z$  boson mass (91.19 GeV) is chosen.

This selection is designed to be tight enough to ensure a high purity of genuine  $\mu\mu$  events, and also loose enough to minimize biases of the embedded event samples. Isolation requirements are avoided, since they would introduce a bias towards less

hadronic activity in the vicinities of the embedded leptons that will appear more isolated than expected in data. The selection results in an expected mixture of events summarized in Table 4.1 from [49].  $Z \rightarrow \mu\mu$  is the dominant process modeled by the embedded technique, with  $t\bar{t}$ , QCD, and diboson and single top processes becoming more significant when considering events with b-tag jets.

Process	Fraction (%)		
	Inclusive	$m_{\mu\mu} > 70$ GeV	$N(\text{b-tag jets}) > 0$
$Z \rightarrow \mu\mu$	97.36	99.11	69.25
QCD	0.84	0.10	2.08
$t\bar{t}$	0.78	0.55	25.61
$Z \rightarrow \tau\tau$	0.71	0.05	0.57
Diboson, single t	0.17	0.17	2.35
W+jets	0.08	0.02	0.14

Table 4.1: Expected event composition after selecting two muons in the embedded technique [49], before additional cuts (i.e. inclusive, *column 2*), and after adding a requirement on the di-muon mass  $m_{\mu\mu} > 70$  GeV (*column 3*), or a requirement on the number of b-tag jets in the event (*column 4*).

The advantage of the embedded technique is that aspects of the event that are difficult to model and describe are directly taken from data, resulting in a better data description than can be achieved with only the  $Z \rightarrow \tau\tau$  simulation [49]. The simulation must be tuned extensively to accurately model aspects of the data, such as time-dependent pile-up profiles, the production of additional jets, e.g. in multijet and vector boson fusion topologies, the number of reconstructed primary interaction vertices, and the missing transverse momentum  $p_T^{\text{miss}}$ . Since all events with genuine  $\tau\tau$  are estimated with samples made with the embedded technique (referred to as embedded samples from here on), events in Monte Carlo simulation with genuine  $\tau\tau$  are not used, in order to avoid double-counting.

<sup>1236</sup> **Chapter 5**

<sup>1237</sup> **Object reconstruction and**  
<sup>1238</sup> **corrections applied**

<sup>1239</sup> In the data processing workflow, data events and simulated events are analyzed to  
<sup>1240</sup> reconstruct physics objects of interest, and algorithms for distinguishing genuine par-  
<sup>1241</sup> ticle candidates from background, are employed. Section 5.1 describes the physical  
<sup>1242</sup> properties of the most important objects in the  $h \rightarrow aa \rightarrow bb\tau\tau$  analysis: taus,  
<sup>1243</sup> muons, electrons, jets, and jets originating from b-quarks (b-flavor jets), as well as  
<sup>1244</sup> their reconstruction and identification in CMS. In this analysis, the full energy and  
<sup>1245</sup> momentum of the two tau leptons ( $m_{\tau\tau}$ ) is estimated from the measured (i.e. visible)  
<sup>1246</sup> components of the tau leptons using the SVFit/FastMTT algorithm, which is de-  
<sup>1247</sup> scribed in Section 5.2. Corrections are applied to the simulated samples at the object  
<sup>1248</sup> level and the event level to account for known discrepancies between simulations and  
<sup>1249</sup> the data that the simulations are intended to model. These corrections are listed and  
<sup>1250</sup> detailed in Section 5.3.

1251    **5.1 Object reconstruction**

1252    **5.1.1 Taus**

1253    The tau ( $\tau$ ) is the heaviest known lepton. With a rest mass of 1776.86 MeV, it can  
1254    decay to not only electrons and muons, but also hadrons. The mean lifetime of the  $\tau$   
1255    is  $\tau = 290 \times 10^{-15}$  seconds, corresponding to  $c\tau = 87.03 \mu\text{m}$ , which is short enough  
1256    that taus decay in the CMS detector before reaching the detector elements.

1257    In two thirds of the cases,  $\tau$  leptons decay hadronically, typically into one or three  
1258    charged mesons (predominantly  $\pi^+$ ,  $\pi^-$ ), often accompanied by neutral pions (that  
1259    decay  $\pi^0 \rightarrow \gamma\gamma$ ), and a  $\nu_\tau$ . These hadronic decays are denoted  $\tau_h$ . In the remainder of  
1260    the decays, the tau decays to the lighter leptons (electron or muon), termed leptonic  
1261    decays. In all cases, at least one neutrino is produced, resulting in missing transverse  
1262    energy in the CMS detector. The tau's largest decay branching ratios (proportional  
1263    to probability of decay) are listed below [26]:

- 1264        • 17.8% decay to  $e^- \bar{\nu}_e \nu_\tau$
- 1265        • 17.4% decay to  $\mu^- \bar{\nu}_\mu \nu_\tau$
- 1266        • 25.5% decay to  $\pi^- \pi^0 \nu_\tau$  ( $\rho^-$  resonance at 770 MeV)
- 1267        • 10.8% decay to  $\pi^- \nu_\tau$
- 1268        • 9.3% decay to  $\pi^- \pi^0 \pi^0 \nu_\tau$  ( $a_1^-$  resonance at 1200 MeV)
- 1269        • 9.0% decay to  $\pi^- \pi^- \pi^+ \nu_\tau$  ( $a_1^-$  resonance at 1200 MeV)

1270    The neutrinos escape undetected from the CMS detector and are not considered  
1271    in the reconstruction. Charged hadrons leave tracks in the tracking detector before  
1272    being absorbed in the hadronic calorimeter; in CMS tau reconstruction terminology,  
1273    they are often called “prongs”, i.e. the dominant  $\tau_h$  decay modes are termed “1 prong”

1274  $(\pi^\pm)$ , “1 prong +  $\pi^0$ (s)”, and “3-prong”. Neutral pions decay to two photons which  
1275 lose their energy in the electromagnetic calorimeter. Taus that decay to electrons  
1276 and muons, are typically triggered on and reconstructed as electrons and muons  
1277 respectively.

1278 **Hadron plus strips (HPS) reconstruction of  $\tau_h$**

1279 At CMS, hadronically decaying tau leptons are reconstructed with the hadron plus  
1280 strips (HPS) algorithm [52] [53]. The HPS algorithm capitalizes on photon conversions  
1281 in the CMS tracker material, which originate from the neutral pion ( $\pi^0$ ) decaying  
1282 to two photons. The bending of electron/positron tracks due to the CMS solenoid  
1283 magnetic field leads to a spread of the neutral pions’ calorimeter signatures in the  $\phi$   
1284 direction. This motivates the reconstruction of photons in “strips”: objects that are  
1285 built out of PF photons and electrons. The strip reconstruction starts with centering  
1286 a strip on the most energetic electromagnetic particle in a PF jet. Among other  
1287 electromagnetic particles located in a window of size  $\Delta\eta = 0.05$  and  $\Delta\phi = 0.20$   
1288 around the strip center, the most energetic one is associated with the strip and its  
1289 momentum is added to the strip momentum. This is repeated iteratively until no  
1290 further particles can be associated. Lastly, strips satisfying a requirement of  $p_T^{\text{strip}} > 1$   
1291 GeV are combined with charged hadrons to reconstruct individual  $\tau_h$  decay modes,  
1292 where  $h$  stands for both  $\pi$  and  $K$ :

- 1293 • *Single hadron:*  $h^- \nu_\tau$  and  $h^- \pi^0 \nu_\tau$  decay modes, in which the neutral pions have  
1294 too little energy to be reconstructed as strips.
- 1295 • *One hadron + one strip:*  $h^- \pi^0 \nu_\tau$  decay modes, where the photons from the  $\pi^0$   
1296 decay are close together in the calorimeter.
- 1297 • *One hadron + two strips:*  $h^- \pi^0 \nu_\tau$  decay modes, where the photons from the  $\pi^0$   
1298 decay are well separated.

1299       • *Three hadrons:*  $h^- h^+ h^- \nu_\tau$  decay modes. The three charged hadrons are re-

1300           quired to originate from the same secondary vertex.

1301 The  $h^- \pi^0 \pi^0 \nu_\tau$  and  $h^- h^+ h^- \pi^0 \nu_\tau$  decay modes do not have their own treatment are

1302 reconstructed with the above topologies.

1303 In the HPS algorithm, the direction of the reconstructed tau momentum  $\vec{p}^{\tau_h}$

1304 is required to fall within a distance of  $\Delta R = 0.1$  from the original PF jet. All

1305 charged hadrons and strips are required to be contained within a cone of size  $\Delta R =$

1306  $(2.8 \text{ GeV})/p_T^{\tau_h}$ , from the  $\tau_h$  as reconstructed by the HPS.

1307 All charged hadrons are assumed to be pions, and they are required to be consis-

1308 tent with the masses of the intermediate meson resonances (if applicable), with the

1309 following allowed windows for candidates: 50-200 MeV for  $\pi^0$ , 0.3-1.3 GeV for  $\rho$ , and

1310 0.8-1.5 GeV for  $a_1$ . If the  $\tau_h$  decay is compatible with more than one hypothesis, the

1311 one giving the highest  $p_T^{\tau_h}$  is chosen. Lastly, an isolation requirement is applied: aside

1312 from the  $\tau_h$  decay products, no charged hadrons or photons can be present within

1313 an isolation cone of size  $\Delta R = 0.5$  around the direction of the  $\tau_h$ . The outputs of

1314 the HPS algorithm are the reconstructed decay mode and the visible four-momentum

1315 (i.e. the four-momenta of all decay products excluding the neutrinos).

### 1316 DeepTau for identifying $\tau_h$

1317 The identification of  $\tau_h$  candidates in CMS has historically been divided into separate

1318 discriminators against jets, electrons, and muons. Discriminators versus jets and

1319 electrons use information from derived quantities, such as the  $p_T$  sum of particles

1320 near the  $\tau_h$  axis. Building on the previous multivariate analysis (MVA) classifier [54]

1321 based on a boosted decision tree (BDT), DeepTau is a more recent classifier based on a

1322 deep neural network (DNN) that simultaneously discriminates against jets, electrons,

1323 and muons. The DNN uses a combination of high-level inputs, similar to previous

1324 algorithms, and also uses convolutional layers in  $\eta$ - $\phi$  space to process information

1325 from all reconstructed particles near the  $\tau_h$  axis. Convolutional layers are based on  
1326 the principle that an image can be processed independently of its position.

1327 The final DeepTau discriminators against jets, muons, and electrons are given by

$$D_\alpha(y) = \frac{y_\tau}{y_\tau + y_\alpha} \quad (5.1)$$

1328 where  $y_\tau$  ( $y_\alpha$ ) are estimates of the probabilities for the  $\tau_h$  candidate to come from  
1329 a genuine  $\tau_h$  (jet,  $\mu$ ,  $e$ ). Working points for each discriminator with different  $\tau_h$   
1330 identification efficiencies are defined for  $D_e$ ,  $D_\mu$ , and  $D_{\text{jet}}$ , for usage in physics analyses  
1331 and derivation of data-to-simulation corrections [55].

### 1332 5.1.2 Muons

1333 Muons are the next lightest lepton after taus, with a mass of 105.66 MeV and a  
1334 mean lifetime of  $\tau = 2.20 \times 10^{-6}$  seconds, or  $c\tau = 658.64$  m. At CMS, muons are  
1335 identified with requirements on the quality of the track reconstruction and on the  
1336 number of measurements in the tracker and the muon systems [56]. In the standard  
1337 CMS reconstruction, tracks are first reconstructed independently in the inner tracker  
1338 (tracker track) and in the muon system (standalone-muon track). Next, these tracks  
1339 are processed in two different methods.

1340 The first is Global Muon reconstruction (outside-in) [56], which fits combined hits  
1341 from the tracker track and standalone-muon track, using the Kalman-filter technique.  
1342 At large transverse momenta,  $p_T \gtrsim 200$  GeV, the global-muon fit can improve the  
1343 momentum resolution compared to the tracker-only fit.

1344 The second is Tracker Muon reconstruction (inside-out) [56], which starts with  
1345 tracker tracks with  $p_T > 0.5$  GeV and total momentum  $p_T > 2.5$  GeV. These tracks  
1346 are extrapolated outwards to the muon system and matched to detector segments  
1347 there, taking into account the magnetic field, expected energy losses, and multiple

1348 Coulomb scattering in the detector material. Tracker Muon reconstruction is more  
 1349 efficient than the Global Muon reconstruction at low momenta,  $p \lesssim 5$  GeV, because  
 1350 it only requires a single muon segment in the muon system, whereas Global Muon  
 1351 reconstruction typically requires segments in at least two muon stations.

1352 To further suppress fake muons from decay in flight, isolation cuts are used. A  
 1353 relative isolation variable is defined to quantify the energy flow of particles near the  
 1354 muon trajectory. A relative isolation is defined similarly for muons and electrons:

$$I^\ell \equiv \frac{\sum_{\text{charged}} p_T + \max(0, \sum_{\text{neutral}} p_T - \frac{1}{2} \sum_{\text{charged, PU}} p_T)}{p_T^\ell} \quad (5.2)$$

1355 where  $\sum_{\text{charged}} p_T$  is the scalar sum of the  $p_T$  of the charged particles originating from  
 1356 the primary vertex and located in a cone of size  $\Delta R = \sqrt{(\Delta\eta)^2 + (\Delta\phi)^2} = 0.4(0.3)$   
 1357 centered on the direction of the muon (electron). The sum  $\sum_{\text{neutral}} p_T$  is the equivalent  
 1358 for neutral particles. The sum  $\sum_{\text{charged, PU}} p_T$  is the scalar sum of the  $p_T$  of the  
 1359 charged hadrons in the cone originating from pile-up vertices. The factor 1/2 comes  
 1360 from simulation estimations, which find that the ratio of neutral to charged hadron  
 1361 production in the hadronization process of inelastic  $pp$  collisions is 1/2. Thus the  
 1362 subtracted term is intended to subtract contribution from pile-up, from the neutral  
 1363 particle contribution to the isolation sum. Finally, this is divided by the lepton  
 1364 transverse momentum,  $p_T^\ell$ .

### 1365 5.1.3 Electrons

1366 Electrons are the lightest lepton with a mass of 0.511 MeV. At CMS, electrons are  
 1367 reconstructed by associating a track reconstructed in the silicon tracking detector  
 1368 with a cluster of energy in the ECAL. Performance is maximized via a combination  
 1369 of a stand-alone approach and the complementary global particle-flow approach [57].

1370 In the stand-alone approach, the electron energy, which is typically spread over

several crystals of the ECAL, is clustered with the “hybrid” algorithm in the barrel and the “multi- $5 \times 5$ ” in the endcaps [57]. The hybrid algorithm collects energy in a small window in  $\eta$  and an extended window in  $\phi$ . It identifies a seed crystal, and adds arrays of  $5 \times 1$  crystals in  $\eta \times \phi$  in a range of  $N = 17$  crystals in both directions of  $\phi$ , if their energies exceed a minimum threshold, thus forming a supercluster (SC). In the endcap, crystals are not arranged in an  $\eta \times \phi$  geometry; instead clusters are build around seed crystals in clusters of  $5 \times 5$  crystals that can partly overlap. Nearby clusters are grouped into a supercluster, and energy is recovered from associated deposits in the preshower.

In the PF reconstruction [57], PF clusters are reconstructed by aggregating around a seed all contiguous crystals with energies two standard deviations above the electronic noise observed at the beginning of a data-taking run. The energy of a given crystal can be shared among two or more clusters.

The electron track reconstruction is performed in two ways [57]: the ECAL-based seeding, which begins with the SC energy and positioning, and the tracker-based seeding (part of the PF reconstruction algorithm), which uses tracks reconstructed from the general algorithm for charged particles, extrapolated towards the ECAL and matched to an SC. Kalman filter (KF) tracks with a small number of hits or that are not well-fitted, are re-fitted with a dedicated Gaussian sum Filter (GSF).

A global identification variable [57] is defined using a multivariate analysis (MVA) technique that combines information on track observables (kinematics, quality of the KF track and GSF track), the electron PF cluster observables (shape and pattern), and the association between the two (geometric and kinematic observables). For electrons seeded only through the tracker-based approach, a weak selection is applied on this MVA variable. For electrons seeded through both approaches, a logical OR is taken.

Electron isolation, i.e. the presence of energy deposits near the electron trajectory,

1398 is a separate key handle in rejecting significant background. Compared to isolated  
 1399 electrons, electrons from misidentified jets or genuine electrons within a jet resulting  
 1400 from semileptonic decays of  $b$  or  $c$  quarks tend to have significant energy deposits  
 1401 near the primary trajectory [57]. Offline analyses benefit from the PF technique  
 1402 for defining isolation, which sums the PF candidates reconstructed located within a  
 1403 specified isolation cone around the electron candidate, as in Eqn. 5.2.

#### 1404 **5.1.4 Jets**

1405 The vast majority of processes of interest at the LHC contains quarks or gluons in  
 1406 the final state, but these particles cannot be observed directly. In a process called  
 1407 hadronization, they fragment into spatially-grouped collections of particles called jets,  
 1408 which can be detected in the tracking and calorimeter systems. Hadronization and  
 1409 the subsequent decays of unstable hadrons can produce hundreds of nearby particles  
 1410 in the CMS detector. Jets are reconstructed by the PF algorithm (PF jets), or from  
 1411 the sum of the ECAL and HCAL energies deposited in the calorimeter towers (Calo  
 1412 jets). In PF jets, typically used in offline analyses, jets are built using the anti- $k_T$   
 1413 (AK) clustering algorithm [58]. The anti- $k_T$  algorithm iterates over particle pairs and  
 1414 finds the two that are closest in a distance measure  $d$ , and determines whether to  
 1415 combine them:

$$d_{ij} = \min(p_{T,i}^{-2}, p_{T,j}^{-2}) \frac{\Delta_{ij}^2}{R^2}, \text{ combine when } d_{ij} < p_{T,i}^{-2}; \text{ stop when } d_{ij} > p_{T,i}^{-2} \quad (5.3)$$

1416 where  $\Delta_{ij}^2 = (\eta_i - \eta_j)^2 + (\phi_i - \phi_j)^2$  and  $p_{T,i}$ ,  $\eta_i$ ,  $\phi_i$  are the transverse momentum, rapid-  
 1417 ity, and azimuthal angle of particle  $i$ . The power  $-2$  means that higher-momentum  
 1418 particles are clustered first, leading to jets that tend to be centered on the hardest  
 1419 (highest  $p_T$ ) particle.

1420 There are several methods to remove contributions of pile-up collisions from jet

1421 clustering [59]:

- 1422     • Charged hadron subtraction (CHS), which removes all charged hadron candidates associated with a track that is not associated with the primary vertex.
- 1424     • PileUp Per Particle Identification (PUPPI), which weighs input particles based  
1425       on their likelihood of arising from pile-up. QCD particles tend to have a collinear  
1426       structure, compared to soft diffuse radiation coming from pile-up. The local  
1427       shape for charged pile-up, used as a proxy for all pile-up particles, is used on an  
1428       event-by-event basis to calculate a weight for each particle. PUPPI is deployed  
1429       in Run-2 and is more performant than CHS in high pile-up scenarios.

1430 **5.1.5 B-flavored jets**

1431 Jets that arise from bottom-quark hadronization (b-flavor jets) have overwhelming  
1432 background from processes involving jets from gluons (g) and light-flavor quarks (u, d,  
1433 s), and from c-quark fragmentation. The ability to identify b-flavor jets, or b-tagging,  
1434 exploits the b hadrons' relatively large masses, long lifetimes, and daughter particles  
1435 with hard momentum spectra [58].

1436 The impact parameter (IP) of a track is the 3-dimensional distance between the  
1437 track and the primary vertex (PV) at the point of closest approach. The IP is positive  
1438 if the track originates from the decay of particles travelling along the jet axis. The  
1439 resolution of the IP depends on the  $p_T$  and  $\eta$  of the track, motivating the use of the  
1440 impact parameter significance  $S_{\text{IP}}$  (ratio of the IP to its estimated uncertainty) as an  
1441 observable [58].

1442 Because of the large but finite lifetimes of the b hadrons, b hadrons tend to  
1443 travel a short distance before decaying at a secondary vertex (SV), which can be  
1444 measured and reconstructed separately from the primary vertex due to the excellent  
1445 position resolution of the pixel detector [58]. Previous b-tagging algorithms (e.g.

1446 CSV, cMVAv2, and DeepCSV) have capitalized on variables such as the presence of  
1447 a SV, the flight distance and direction (computed from the vector between the PV  
1448 and the SV), and kinematics of the system of associated secondary tracks (e.g. track  
1449 multiplicity, mass, and energy).

1450 The DeepJet (formerly known as DeepFlavour) algorithm [60] is a deep-neural-  
1451 network multi-classification algorithm, which uses 16 properties of up to 25 charged  
1452 and 6 properties of 25 neutral particle-flow jet constituents, as well as 17 properties  
1453 from up to 4 secondary vertices associate with the jet. Compared to the previous clas-  
1454 sifying algorithm DeepCSV, DeepJet has been demonstrated to have higher efficiency  
1455 with lower misidentification probability in Phase-1 data [61].

## 1456 5.2 Reconstruction of the $\tau\tau$ mass

1457 The final signal extraction is done to the total  $\tau\tau$  mass, which is estimated from the  
1458 visible  $\tau\tau$  mass using the FastMTT algorithm [62]. FastMTT is based on the SVFit  
1459 algorithm, originally developed for the Standard Model  $H \rightarrow \tau\tau$  analysis [63]. Both  
1460 the SVFit algorithms, and the FastMTT algorithm, are described below, to give a  
1461 complete picture of how tau decays are parameterized.

1462 To specify a hadronic  $\tau$  decay, six parameters are needed [63]: the polar and  
1463 azimuthal angles of the visible decay product system in the  $\tau$  rest frame, the three  
1464 boost parameters from the  $\tau$  rest frame to the laboratory frame, and the invariant  
1465 mass  $m_{\text{vis}}$  of the visible decay products. For a leptonic  $\tau$  decay, two neutrinos are  
1466 produced, and a seventh parameter, the invariant mass of the two-neutrino system, is  
1467 necessary. The unknown parameters are constrained by four observables that are the  
1468 components of the four-momentum of the system formed by the visible decay products  
1469 of the  $\tau$  lepton, measured in the laboratory frame. The remaining unconstrained  
1470 parameters for hadronic and leptonic  $\tau$  decays are thus:

- 1471     • The fraction of the  $\tau$  energy in the laboratory frame carried by the visible decay  
 1472         products,
- 1473     •  $\phi$ , the azimuthal angle of the  $\tau$  direction in the laboratory frame,
- 1474     •  $m_{\nu\nu}$ , the invariant mass of the two-neutrino system in leptonic  $\tau$  decays (for  
 1475         hadronic  $\tau$  decays,  $m_{\nu\nu}$  is set to 0).

1476      $E_x^{\text{miss}}$  and  $E_y^{\text{miss}}$ , the  $x$  and  $y$  components of the missing transverse energy  $E_T^{\text{miss}}$   
 1477     provide two further constraints.

### 1478     5.2.1 Original SVFit ‘‘standalone’’: maximum likelihood

1479     In one of the original versions of SVFit, called ‘‘standalone’’ SVFit [63], a maximum  
 1480     likelihood fit method is used to reconstruct the mass  $m_{\tau\tau}$  by combining the measured  
 1481     observables  $E_x^{\text{miss}}$  and  $E_y^{\text{miss}}$  with a likelihood model that includes terms for the  $\tau$   
 1482     decay kinematics and the  $E_T^{\text{miss}}$  resolution [63]. The likelihood function  $f(\vec{z}, \vec{y}, \vec{a}_1 \vec{a}_2)$   
 1483     of the parameters  $\vec{z} = (E_x^{\text{miss}}, E_y^{\text{miss}})$  in an event is constructed, where the remaining  
 1484     parameters are the kinematics of the two  $\tau$  decays, denoted  $\vec{a}_1 = (x_1, \phi_1, m_{\nu\nu,1})$  and  
 1485      $\vec{a}_2 = (x_2, \phi_2, m_{\nu\nu,2})$ , and the four-momenta of the visible decay products with the  
 1486     measured values  $\vec{y} = (p_1^{\text{vis}}, p_2^{\text{vis}})$ .

1487     The likelihood  $f$  is the product of three likelihood functions. The first two likelihood  
 1488     functions model the decay parameters  $\vec{a}_1$  and  $\vec{a}_2$  of the two  $\tau$  leptons. For leptonic  
 1489     decays, the likelihood function is modeled using matrix elements for  $\tau$  decays,  
 1490     and integrated over the allowed phase space  $0 \leq x \leq 1$  and  $0 \leq m_{\nu\nu} \leq m_\tau \sqrt{1-x}$ . For  
 1491     hadronic  $\tau$  decays, a model based on the two-body phase space is used and integrated  
 1492     over  $m_{\text{vis}}^2/m_{\tau\tau}^2 \leq x \leq 1$ . The third likelihood function quantifies the compatibility of  
 1493     a  $\tau$  decay hypothesis with the reconstructed  $\vec{E}_T^{\text{miss}}$  in an event, assuming the neutrinos  
 1494     are the only source of missing transverse energy. The expected  $\vec{E}_T^{\text{miss}}$  resolution

1495 is represented by a covariant matrix, estimated on an event-by-event basis using a  
1496 significance algorithm [64].

### 1497 5.2.2 “Classic SVFit” with matrix element

1498 Classic SVFit is an improved algorithm of the original “standalone” SVFit using the  
1499 formalism of the matrix element (ME) method [62]. In the ME method, an estimate  
1500 for the unknown model parameter  $\Theta$  (here, the mass  $m_{\tau\tau}$ ) is obtained by maximizing  
1501 the probability density  $\mathcal{P}$ . The key ingredients of the probability density are the  
1502 squared modulus of the matrix element  $|\mathcal{M}(\mathbf{p}, \Theta)|^2$  and the transfer function  $W(\mathbf{y}|\mathbf{p})$   
1503 (probability density to observe the measured observables  $\mathbf{y}$  given the phase space  
1504 point  $\mathbf{p}$ ). The best estimate  $m_{\tau\tau}$  is obtained by computing the probability density  $\mathcal{P}$   
1505 for a range of mass hypotheses and finding the value of  $m_{\tau\tau}$  that maximizes  $\mathcal{P}$ .

1506 Distributions illustrating the performance of the classic matrix element SVFit  
1507 algorithm are shown in Fig. 5.1 from [62], showing the di-tau mass after and before  
1508 application of SVFit to recover energy lost to neutrinos. The SVFit algorithm is  
1509 found to improve the sensitivity of the Standard Model  $H \rightarrow \tau\tau$  analysis performed  
1510 by CMS by about 30%, compared to performing the same analysis using only the  
1511 visible mass  $m_{\text{vis}}$ .

### 1512 5.2.3 FastMTT: optimized SVFit

1513 FastMTT [65] is a further simplification to the matrix element method of Classic  
1514 SVFit which has comparable performance but is about 100 times faster. FastMTT  
1515 drops the matrix element component of the computation without significant impact  
1516 on the final mass resolution, and simplifies the computation of the transfer functions.  
1517 The opening angle of the  $\tau$  decay products with respect to the initial  $\tau$  momenta ap-  
1518 proaches 0 for  $\tau$  with high  $\gamma = E_\tau/m_\tau$ , with typical  $\tau$  decays from the Z boson decays  
1519 already satisfying this condition. In this collinear approximation, the dimensionality

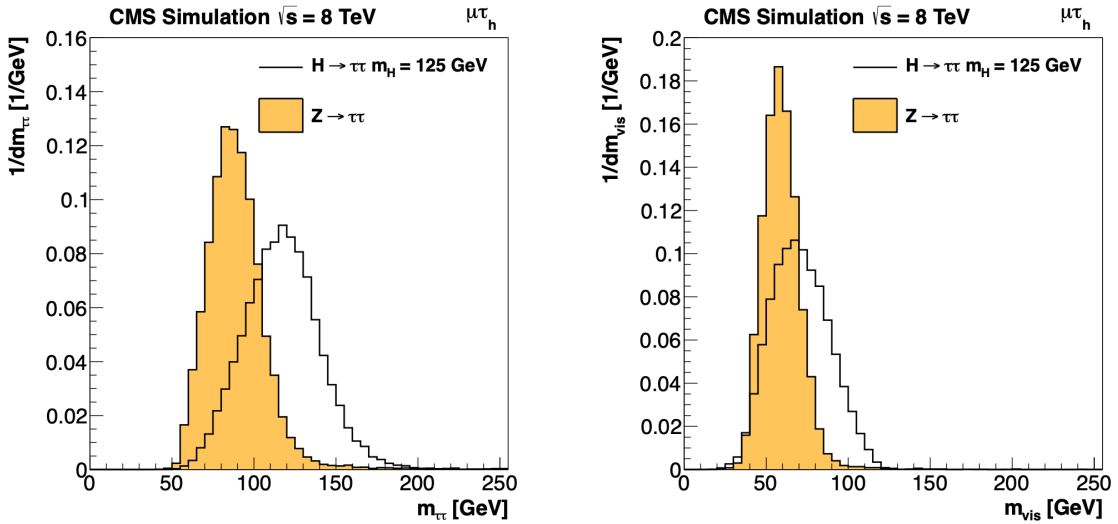


Figure 5.1: Distributions from [62], of  $m_{\tau\tau}$  after reconstruction with the original SVFit algorithm (*left*), and before SVFit with only the visible tau decay products (*right*), for  $H \rightarrow \tau\tau$  signal events of mass  $m_H = 125$  GeV (*black line*) and the  $Z/\gamma^* \rightarrow \tau\tau$  background (*orange, solid*), in the decay channel  $\tau\tau \rightarrow \mu\tau_h$ .

of the transfer function can be reduced in the computation of FastMTT, while still yielding similar results to Classic SVFit [65].

### 5.3 Corrections applied to simulation

Corrections are applied to simulated samples to account for known effects in the event modeling and reconstruction and data-taking, and are intended to bring simulations in closer agreement with data. Corrections fall into two broad categories: *energy scale corrections* applied to physics objects, and *event-level corrections*. Energy scale corrections are multiplicative factors applied to the energy and transverse momentum  $p_T$  of simulated objects (e.g. leptons or jets), and bring the average reconstructed energies of simulated particles into better agreement with those of objects reconstructed from data. Event-level corrections are applied as a per-event multiplicative weight, and account for effects such as mis-modeling in simulations of the underlying physics process, or changing detector operating conditions during data-taking. Event-level

1533 corrections change the shapes of the distributions of all the physical observables.

1534 Uncertainties in scale factors and corrections are also sources of systematic errors  
1535 in the analysis, detailed in Chapter 8. Systematic uncertainties in the tau, muon, and  
1536 electron energy scales can shift the  $p_T$  of the leptons up or down, which can change  
1537 whether events pass or fail the offline  $p_T$  thresholds for the trigger paths described in  
1538 the previous section, i.e. change the number of events in the signal region.

### 1539 5.3.1 Tau energy scale

1540 An energy scale is applied to the transverse momentum  $p_T$  and mass of the hadronic  
1541 tau  $\tau_h$  in the  $\mu\tau_h$  and  $e\tau_h$  channels, to correct for a deviation of the average recon-  
1542 structed  $\tau_h$  energy from the generator-level energy of the visible  $\tau_h$  decay products.  
1543 These correction factors are derived centrally [54], by fitting to events in  $e\tau_h$  and  $\mu\tau_h$   
1544 final states in  $Z/\gamma^*$  events separately for the  $h^\pm$ ,  $h^\pm\pi^0$ , and  $h^\pm h^\mp h^\pm$  decays. The  
1545 values used are shown in Table 5.1.

1546 When applying the energy scale to the  $\tau_h$ , the 4-momentum of the missing trans-  
1547 verse energy (MET) is adjusted such that the total 4-momenta of the  $\tau_h$  and the MET  
1548 remains unchanged [66].

Tau energy scale factor				
Decay mode	2018	2017	2016 pre-VFP	2016 post-VFP
0	$0.991 \pm 0.008$	$0.986 \pm 0.009$	$0.987 \pm 0.01$	$0.993 \pm 0.009$
1	$1.004 \pm 0.006$	$0.999 \pm 0.006$	$0.998 \pm 0.006$	$0.991 \pm 0.007$
10	$0.998 \pm 0.007$	$0.999 \pm 0.007$	$0.984 \pm 0.008$	$1.001 \pm 0.007$
11	$1.004 \pm 0.009$	$0.996 \pm 0.01$	$0.999 \pm 0.011$	$0.997 \pm 0.016$

Table 5.1: Energy scales applied to genuine hadronic tau decays  $\tau_h$  by data-taking year/era and decay mode, along with systematic errors.

1549 **5.3.2 Muon energy scale**

1550 An energy scale is applied to the  $p_T$  and mass of genuine muons from  $\tau$  decays in the  
1551  $e\mu$  and  $\mu\tau_h$  channels [67]. The applied values are the same for MC and embedded  
1552 samples and are shown in Table 5.2. Following the SM  $H \rightarrow \tau\tau$  analysis, Rochester  
1553 corrections are not applied, and instead prescriptions from [68] are followed.

Muon energy scale factor	
Eta range	Value for all years
$ \eta  \in [0.0, 1.2)$	$1.0 \pm 0.004$
$ \eta  \in [1.2, 2.1)$	$1.0 \pm 0.009$
$ \eta  \in [2.1, 2.4)$	$1.0 \pm 0.027$

Table 5.2: Energy scales and systematic errors applied to genuine muons. The values are the same for MC and embedded for all years [69] [68].

1554 **5.3.3 Electron energy scale**

1555 Corrections to the electron energy scale are applied to genuine  $e$  from  $\tau$  decays, and  
1556 are binned in two dimensions by electron  $p_T$  and  $\eta$  for barrel vs. endcap [70]. The  
1557 scale factors are binned in  $p_T$  and  $\eta$  for MC samples: e.g. values for 2018 are shown  
1558 in Fig. 5.2 from [71]. For embedded samples the electron energy scale is taken as  
1559 only binned in  $\eta$  (Table 5.3).

Electron energy scale factor for embedded samples			
Eta range	2018	2017	2016
$ \eta  \in [0.0, 1.479)$	$0.973 \pm 0.005$	$0.986 \pm 0.009$	$0.9976 \pm 0.0050$
$ \eta  \in [1.479, 2.4)$	$0.980 \pm 0.0125$	$0.887 \pm 0.0125$	$0.993 \pm 0.0125$

Table 5.3: Energy scales and systematic errors applied to electrons in embedded samples, binned in the electron  $\eta$ , by data-taking year [72] [73] [74].

1560 **5.3.4  $\tau_h$  identification efficiency**

1561 The  $\tau_h$  identification efficiency can differ in data and MC [66]. Recommended correc-  
1562 tions are provided by the Tau POG, and we use the medium DeepTau vs. jet working

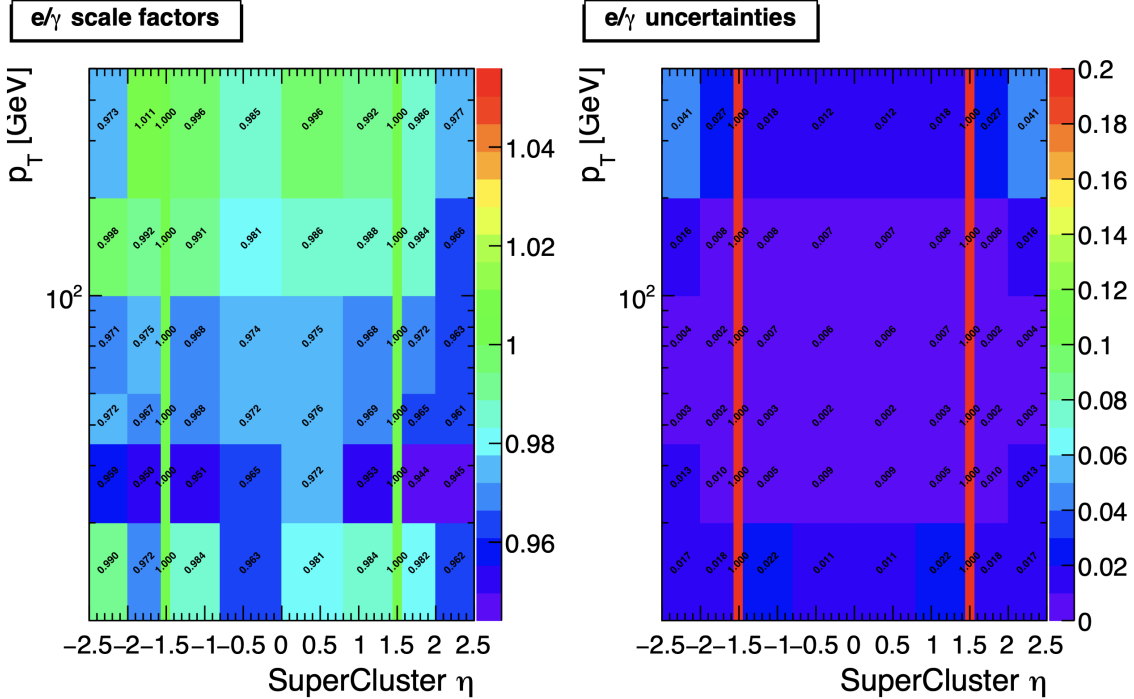


Figure 5.2: Electron/photon energy scale factors (*left*) and corresponding uncertainties (*right*) binned in the electron  $\eta$  and  $p_T$ , for the data-taking year 2018 [71].

1563 point values. The identification efficiency is measured in  $Z \rightarrow \tau\tau$  events in the  $\mu\tau_h$   
 1564 final state, and is binned in  $p_T$  due to clear  $p_T$  dependence of the DeepTau ID.

Tau ID efficiency for DeepTau Medium vs. jet WP in 2018						
$p_T$ (GeV)	< 20	(20, 25]	(25, 30]	(30, 35]	(35, 40]	(40, 500]
Central value	0	0.945	0.946	0.916	0.921	1.005
Up value	0	1.001	0.981	0.946	0.950	1.035
Down value	0	0.888	0.981	0.883	0.893	0.953

Table 5.4: Tau ID efficiency for the DeepTau vs. jet medium working point, with central, up, and down values for 2018, binned in the tau  $p_T$  [66].

### 1565 5.3.5 Trigger efficiencies

1566 Scale factors are applied to correct for differences in trigger efficiencies between MC  
 1567 and embedded vs. data, with values taken from tools provided by the Standard Model  
 1568  $H \rightarrow \tau\tau$  working group which uses the same trigger paths [69]. In the following

1569 sections we review relevant trigger efficiencies in data, which form the basis of the  
1570 trigger efficiency corrections applied to MC and embedded.

1571 **5.3.6 Tau trigger efficiencies**

1572 The efficiencies in data of the single- $\tau_h$  leg in  $\mu\tau_h$ ,  $e\tau_h$ , and di- $\tau_h$  triggers is computed  
1573 centrally per using a Tag and Probe (TnP) method [75] which is outlined here. In  
1574 this method,  $Z \rightarrow \tau\tau \rightarrow \mu\tau_h$  are selected in data and a Drell-Yan simulated sample  
1575 ( $Z \rightarrow \ell\ell, \ell = e, \mu, \tau_h$ ) with high purity. Cuts are applied to reject events not in this  
1576 final state, e.g. suppressing  $Z \rightarrow \mu\mu$  by vetoing events with a single loose ID muon.  
1577 An isolated muon candidate (the tag) with online  $p_T > 27$  GeV and  $|\eta| < 2.1$  is  
1578 identified and matched to an offline  $\mu$ . An offline  $\tau_h$  candidate (the probe) is selected,  
1579 which is separated from the tag  $\mu$ , and has  $p_T > 20$  GeV and  $|\eta| < 2.1$ . The probe  
1580  $\tau_h$  must pass anti-muon and anti-electron discriminators to avoid fakes from muons  
1581 and electrons, and must pass the medium MVA tau isolation to suppress fakes from  
1582 QCD jets. The trigger efficiency in the TnP method is calculated as

$$\text{Efficiency} = \frac{\text{Number of events passing the TnP selection with fires the HLT path}}{\text{Number of events passing the TnP selection}} \quad (5.4)$$

1583 The efficiencies for the hadronic tau legs in the relevant channels of this analyses  
1584 ( $\mu\tau_h$  and  $e\tau_h$ ) as a function of the offline tau  $p_T$  and  $\eta$ , are shown for data taken in  
1585 2016, 2017, and 2018 in Figures 5.3a and 5.3b [75] [76]. In both figures, the different  
1586 HLT thresholds and differences in the L1 seed result in higher efficiencies in 2016 and  
1587 differences in shapes of the 2016 efficiencies compared to 2017 and 2018. The low  
1588 pile-up in 2016 also leads to higher efficiencies in that year.

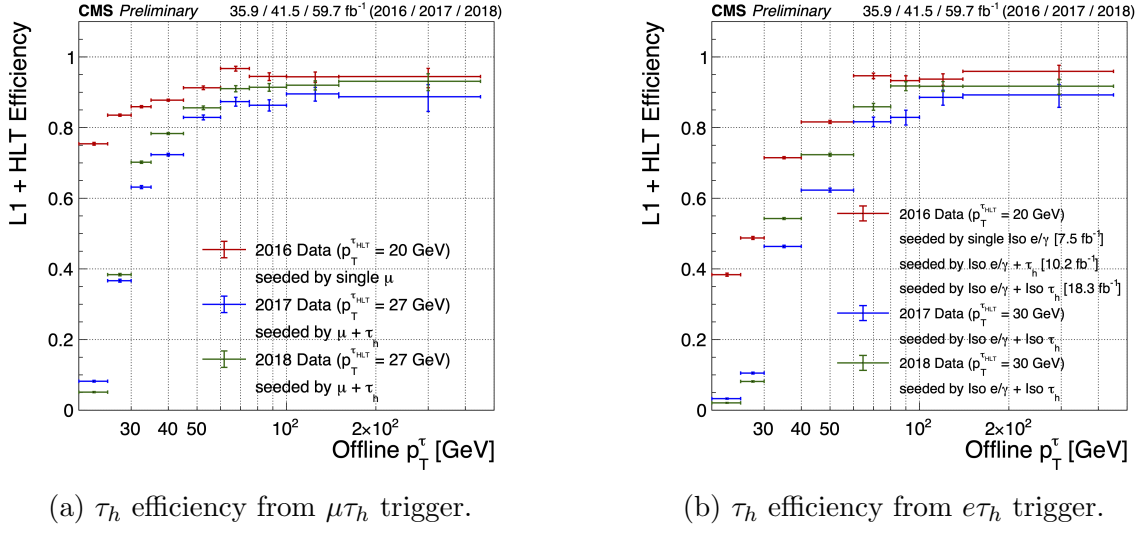
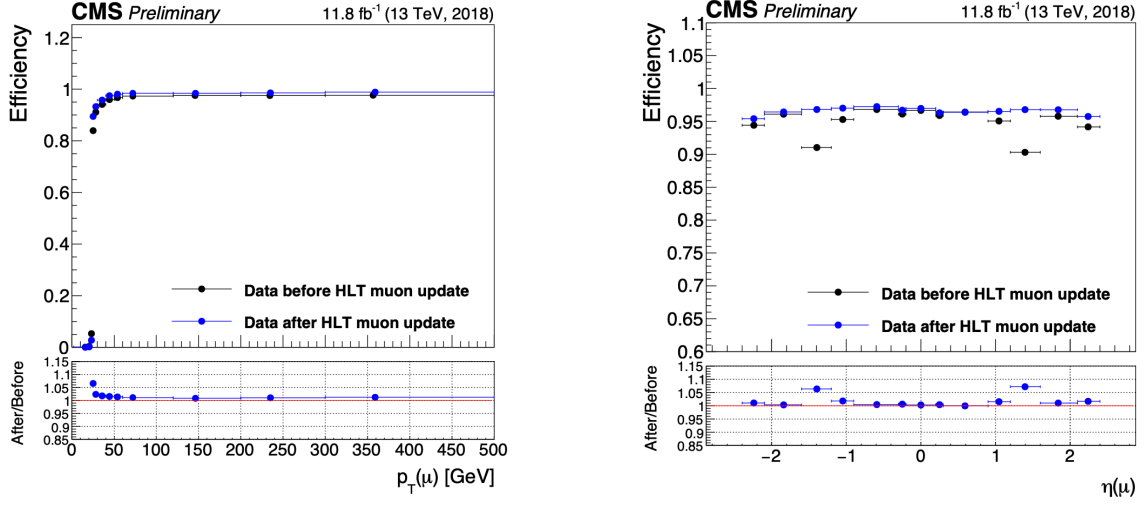


Figure 5.3: Hadronic tau leg efficiency of the cross-triggers for  $\mu\tau_h$  (left) and  $e\tau_h$  (right) triggers as a function of offline tau  $p_T$  for the years 2016 (red), 2017 (blue) and 2018 (green), from [76]. HLT  $p_T$  thresholds and L1 seeds are indicated in the legends.

### 1589 5.3.7 Single muon trigger efficiencies

1590 The efficiencies for the single isolated muon trigger with  $p_T > 24 \text{ GeV}$  used in this  
 1591 analysis, is shown for the data-taking year 2018 in Fig. 5.4a as a function of the muon  
 1592  $p_T$  and as a function of the muon  $|\eta|$  in Fig. 5.4b from [77]. The data is split with  
 1593 respect to a HLT muon reconstruction update that was deployed on 15/05/2018. A  
 1594 small asymmetry in efficiencies between negative and positive  $\eta$  in Fig. 5.4b is due to  
 1595 disabled muon chambers (CSCs). The efficiencies shown are estimated using a Tag  
 1596 and Probe method using  $Z \rightarrow \mu\mu$  events, with the tag being an offline muon with  
 1597  $p_T > 29 \text{ GeV}$  and  $|\eta| < 2.4$  passing a tight ID criteria, and the probe is an online (L1)  
 1598 trigger object with  $\Delta R < 0.3$  and passing tight ID and Particle Flow based isolation  
 1599 requirements with  $p_T > 26 \text{ GeV}$ .



(a) Muon efficiency vs  $p_T$  for SingleMuon.

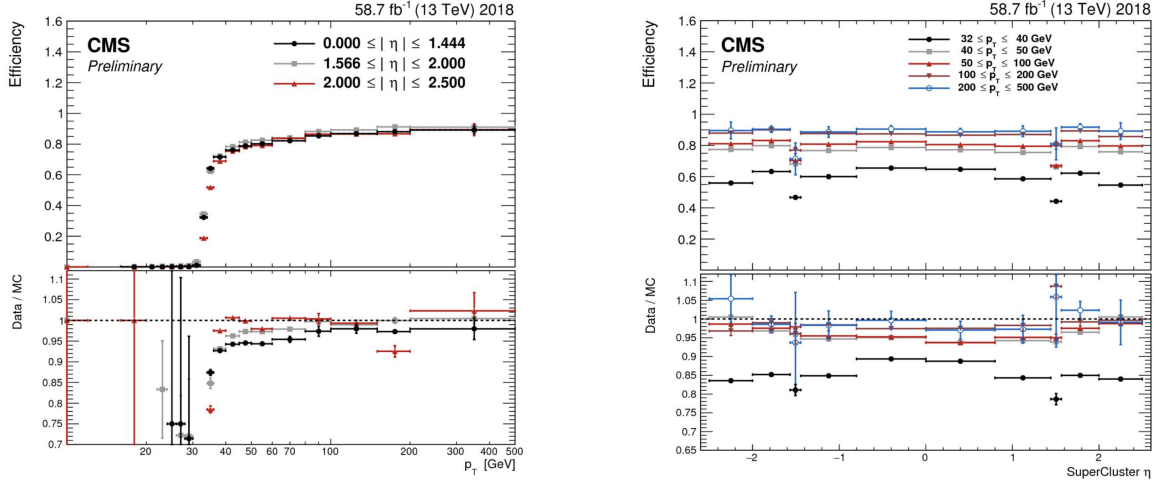
(b) Muon efficiency vs  $|\eta|$  for SingleMuon.

Figure 5.4: Trigger efficiencies in data (*top panels*) and ratio of efficiencies after/before a HLT muon reconstruction update (*bottom panels*) for the muon in the isolated single muon trigger with threshold  $p_T > 24$  GeV in the data-taking year 2018, as functions of the muon  $p_T$  (*left*) and muon  $|\eta|$  (*right*). Only statistical errors are shown [77].

### 1600 5.3.8 Single electron trigger efficiencies

1601 The efficiencies in data, and the ratio between data and MC, of the single electron  
 1602 HLT trigger with  $p_T$  threshold 32 GeV used in this analysis are shown for 2018,  
 1603 as a function of the electron  $p_T$  in Fig. 5.5a and of the electron  $|\eta|$  in Fig. 5.5b,  
 1604 from [78]. In the Tag and Probe method used for the 2018 dataset, the tag is an  
 1605 offline reconstructed electron with  $|\eta| \leq 2.1$  and not in the barrel and endcap overlap  
 1606 region, with  $p_T > 35$  GeV with tight isolation and shower shape requirements, firing  
 1607 the tag trigger. The probe is an offline reconstructed electron with  $|\eta| \leq 2.5$  with  
 1608  $E_T^{\text{ECAL}} > 5$  GeV with no extra identification criteria [78].

1609 The disagreement between data and MC, particularly at low transverse momen-  
 1610 tum, is in part due to detector effects that are difficult to simulate, such as crys-  
 1611 tal transparency losses in the ECAL and the evolution of dead regions in the pixel  
 1612 tracker [78].



(a) Electron efficiency vs  $p_T$  for single electron.

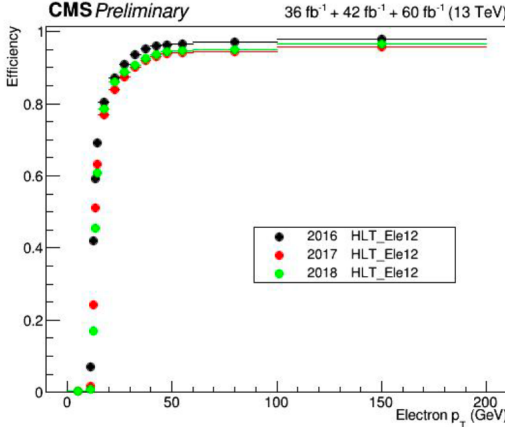
(b) Electron efficiency vs  $|\eta|$  for single electron.

Figure 5.5: Trigger efficiencies in data, and the data/MC ratio for the electron in the single electron trigger with threshold  $p_T > 32$  GeV in the data-taking year 2018, as functions of the electron  $p_T$  (*left*) and electron  $|\eta|$  (*right*) [78]. In the plot vs.  $p_T$ , the region  $1.442 \leq |\eta| \leq 1.566$  is not included as it corresponds to the transition between barrel and endcap parts of the ECAL.

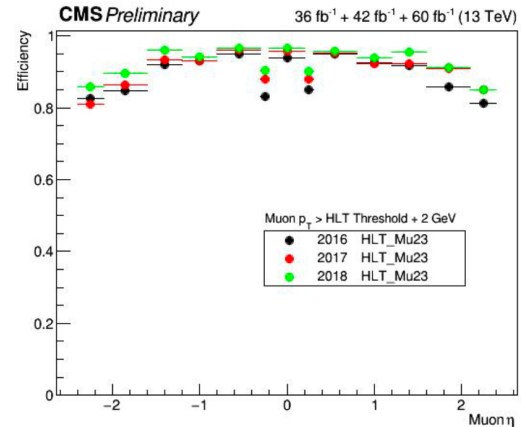
### **5.3.9 $e\mu$ cross-trigger efficiencies**

The efficiencies of the electron and muons for the cross-trigger with leading muon used in the  $e\mu$  channel are shown for data in 2016, 2017, and 2018 in Figures 5.6a and 5.6b [79]. These efficiencies were measured centrally using a Tag and Probe in events with  $Z$  to dileptons with the same flavor and opposite charge, where the tags are an isolated muon or electron, and the probe (offline) candidate is required to satisfy the same lepton selection as that of the tag candidate, be matched within  $\Delta R < 0.1$  with a corresponding online trigger object, and also to pass the cross-trigger. The trigger efficiency is then:

$$\text{Efficiency} = \frac{\text{Events passing lepton pair selections and probe passing trigger}}{\text{Events passing lepton pair selections}} \quad (5.5)$$



(a) Electron efficiency vs.  $p_T$ .



(b) Muon efficiency vs.  $\eta$ .

Figure 5.6: Efficiencies of the electron leg vs.  $p_T$  (*left*) and the muon log vs.  $\eta$  (*right*), for the HLT path with online thresholds of 12 GeV for the electron and 23 GeV for the muon, for the data-taking years 2016 (*black*), 2017 (*red*), and 2018 (*green*) [79].

### 1622 5.3.10 Electrons and muons faking $\tau_h$ : energy scales

1623 Energy scales for electrons misidentified as hadronic tau decays ( $e$  faking  $\tau_h$ ) are  
 1624 provided by the Tau POG, and were measured in the  $e\tau_h$  channel with the visible  
 1625 invariant mass of the electron and hadronic tau system [69]. This energy scale is  
 1626 applied for  $\tau_h$  with  $p_T > 20$  GeV regardless of which DeepTau vs. electron working  
 1627 point was used. Values for 2018 are shown in Table 5.5.

Electrons faking $\tau_h$ energy scale factor in 2018	
Reconstructed decay mode of the fake $\tau_h$	Central value and (up, down) shifts
0	1.01362 (+0.00474, -0.00904)
1	1.01945 (+0.01598, -0.01226)
10	0.96903 (+0.0125, -0.03404)
11	0.985 (+0.04309, -0.05499)

Table 5.5: Energy scales and up/down systematic uncertainties applied to electrons misidentified as hadronic taus for 2018, binned in decay mode of the fake  $\tau_h$  [69].

1628 No nominal energy scale is applied for muons mis-reconstructed as  $\tau_h$ , and the  
 1629 uncertainty is treated as  $\pm 1\%$  and uncorrelated in the reconstructed decay mode [69].

1630    **5.3.11 Electrons and muons faking  $\tau_h$ : misidentification effi-**  
 1631    **ciencies**

1632    Corrections on identification efficiencies are applied to genuine electrons and muons  
 1633    misidentified as  $\tau$  to account for differences in data and MC.

1634    The specific values depend on the vs. electron and vs. muon discriminator working  
 1635    points used. For misidentified  $\mu \rightarrow \tau_h$ , the scale factors are split into different  $|\eta|$   
 1636    regions, determined by the CMS muon and tracker detector geometries, as shown in  
 1637    Table 5.6 for 2018 [66].

Tau ID efficiency for DeepTau vs. muon WPs in 2018		
$ \eta $	Tight working point	VLoose working point
(0.0, 0.2)	$0.767 \pm 0.127$	$0.954 \pm 0.069$
(0.2, 0.6)	$1.255 \pm 0.258$	$1.009 \pm 0.098$
(0.6, 1.0)	$0.902 \pm 0.203$	$1.029 \pm 0.075$
(1.0, 1.45)	$0.833 \pm 0.415$	$0.928 \pm 0.145$
(1.45, 2.0)	$4.436 \pm 0.814$	$5.000 \pm 0.377$
(2.0, 2.53)	$1.000 \pm 0.000$	$1.000 \pm 0.000$

Table 5.6: Tau mis-identification efficiency for the DeepTau Tight and Very Loose (VLoose) working points vs. muons in 2018, binned in the muon  $|\eta|$  [66].

1638    For misidentified  $e \rightarrow \tau_h$ , the scale factors are split into barrel and endcap regions,  
 1639    dictated by the ECAL detector geometry, as shown in Table 5.7 for 2018.

Tau ID efficiency for DeepTau vs. electron WPs in 2018		
$ \eta $	Tight working point	VLoose working point
(0.0, 0.73)	$1.47 \pm 0.27$	$0.95 \pm 0.07$
(0.73, 1.509)	$1.509 \pm 0.0$	$1.00 \pm 0.0$
(1.509, 1.929)	$1.929 \pm 0.2$	$0.86 \pm 0.1$
(1.929, 2.683)	$2.683 \pm 0.9$	$2.68 \pm 0.0$

Table 5.7: Tau mis-identification efficiency for the DeepTau Tight and Very Loose (VLoose) working points vs. electrons in 2018, binned in the electron  $|\eta|$  [66].

### 1640 5.3.12 Electron ID and tracking efficiency

1641 Scale factors are applied to MC to correct for differences between MC and data in  
 1642 the performance of electron identification (ID) and tracking.

1643 Electron and photon identification, as discussed earlier, use variables with good  
 1644 signal vs. background discrimination power such as lateral shower shape and ratio  
 1645 of energy deposited in the HCAL to energy deposited in the ECAL at the position  
 1646 of the electron. The cut-based electron identification efficiencies in data and ratio of  
 1647 efficiencies in data to MC are shown in Fig. 5.7a for the multivariate analysis (MVA)  
 1648 identification working point.

1649 The tracking efficiencies in data and the data/MC ratio are shown in Fig. 5.7b  
 1650 for the Gaussian-sum filter (GSF) tracking [80].

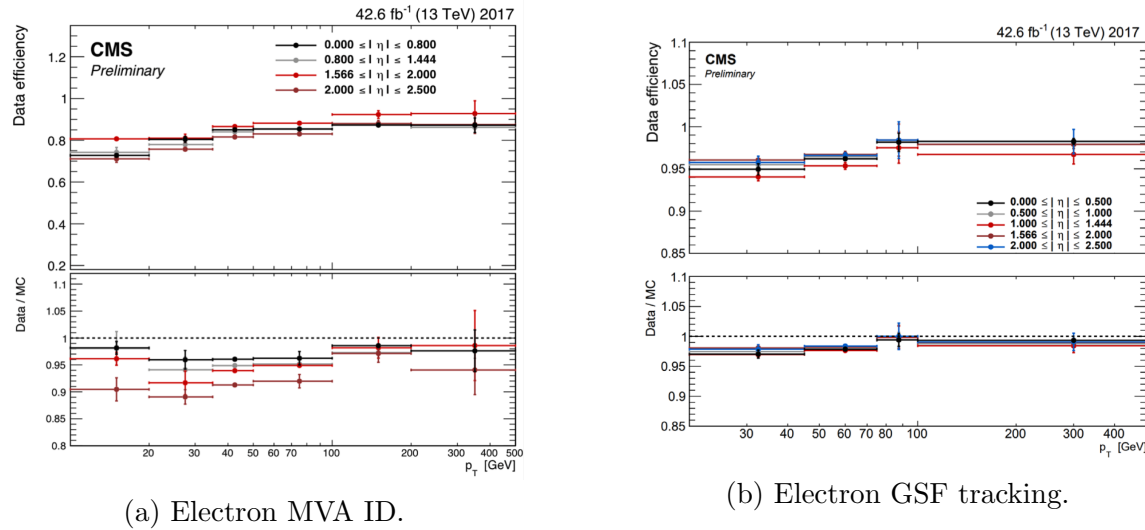


Figure 5.7: Efficiencies in data (*top panels*) and the ratio of efficiencies in data/MC (*bottom panels*), for the electron multivariate analysis (MVA) identification (*left*) and for the Gaussian-sum filter (GSF) tracking (*right*) [80]. Error bars represent statistical and systematic uncertainties.

### 1651 5.3.13 Muon ID, isolation, and tracking efficiencies

1652 Scale factors are applied to MC to correct for differences between MC and data in  
 1653 the performance of muon identification, isolation, and tracking, as detailed below.

1654        The efficiencies for muon identification measured in 2015 data and MC simulation  
 1655        are shown in Figures 5.8a and 5.8b for the loose ID and tight ID respectively [81]. The  
 1656        loose ID is chosen such that efficiency exceeds 99% over the full  $\eta$  range, and the data  
 1657        and simulation agree to within 1%. The tight ID is chosen such that efficiency varies  
 1658        between 95% and 99% as a function of  $\eta$ , and the data and simulation agree to within  
 1659        1-3%. The muon identification working point used in this analysis is the medium ID,  
 1660        which has an efficiency of 98% for all  $\eta$  and an agreement within 1-2% [81].

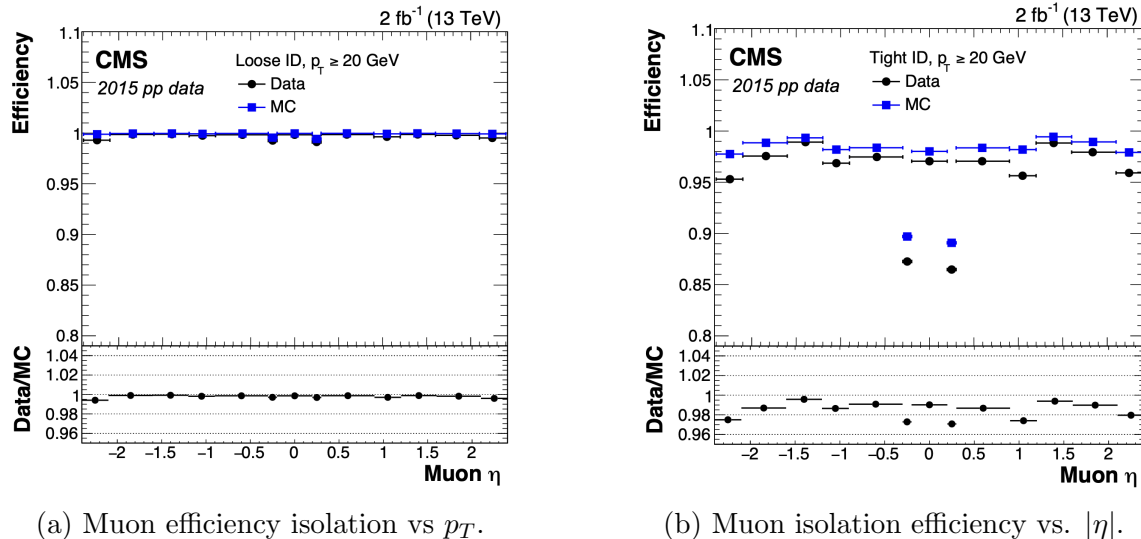
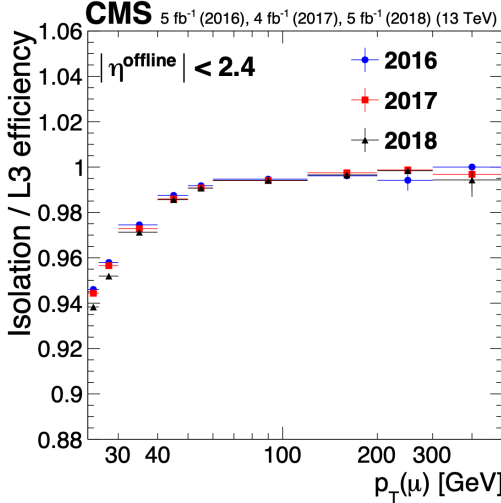


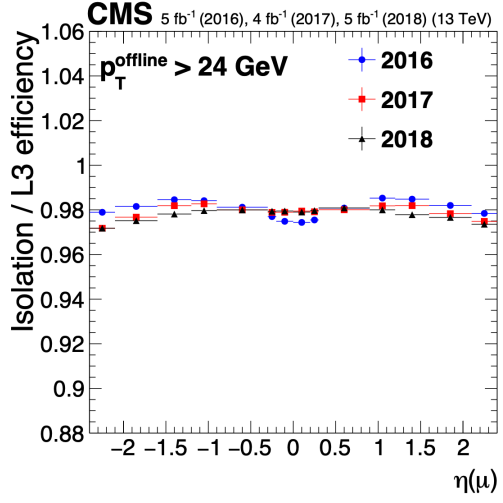
Figure 5.8: Muon identification efficiencies in 2015 data and MC as a function of the muon  $p_T$  for the loose ID (left) and tight ID (right) working points [81].

1661        The efficiencies in data for the muon isolation, as measured in Level-3 muons  
 1662        (muons in one of the final stages of reconstruction in the HLT), as a function of the  
 1663        muon  $p_T$  and  $|\eta|$  are shown in Figures 5.9a and 5.9b [81]. The HLT muon reconstruc-  
 1664        tion consists of two steps: Level-2 (L2), where the muon is reconstructed in the muon  
 1665        subdetectors only, and Level-3 (L3) which is a global fit of tracker and muon hits (i.e.  
 1666        the global muon reconstruction as described in Section 5.1.2) [82].

1667        The muon tracking efficiencies as a function of  $|\eta|$  for standalone muons (i.e. tracks  
 1668        from only the muon system, i.e. DT, CSC, and RPC, as discussed in Section 5.1.2),  
 1669        is shown for data and simulated Drell-Yan samples in Fig. 5.10 [83].



(a) Muon efficiency isolation vs  $p_T$ .



(b) Muon isolation efficiency vs.  $|\eta|$ .

Figure 5.9: Muon isolation efficiencies in Run-2 data with respect to Level-3 muons (one of the final stages of HLT muon reconstruction) as a function of the muon  $p_T$  (left) and  $|\eta|$  (right) [81].

### 1670 5.3.14 Recoil corrections

1671 In proton-proton collisions, W and Z bosons are predominantly produced through  
 1672 quark-antiquark annihilation. Higher-order processes can induce radiated quarks or  
 1673 gluons that recoil against the boson, imparting a non-zero transverse momentum to  
 1674 the boson [84]. Recoil corrections accounting for this effect are applied to samples  
 1675 with W+jets, Z+jets, and Higgs bosons [69]. The corrections are performed on the  
 1676 vectorial difference between the measured missing transverse momentum and the total  
 1677 transverse momentum of neutrinos originating from the decay of the W, Z, or Higgs  
 1678 boson. This vector is projected onto the axes parallel and orthogonal to the boson  
 1679  $p_T$ . This vector, and the resulting correction to use, is measured in  $Z \rightarrow \mu\mu$  events,  
 1680 since these events have leptonic recoil that do not contain neutrinos, allowing the  
 1681 4-vector of the Z boson to be measured precisely. The corrections are binned in  
 1682 generator-level  $p_T$  of the parent boson and also the number of jets in the event.

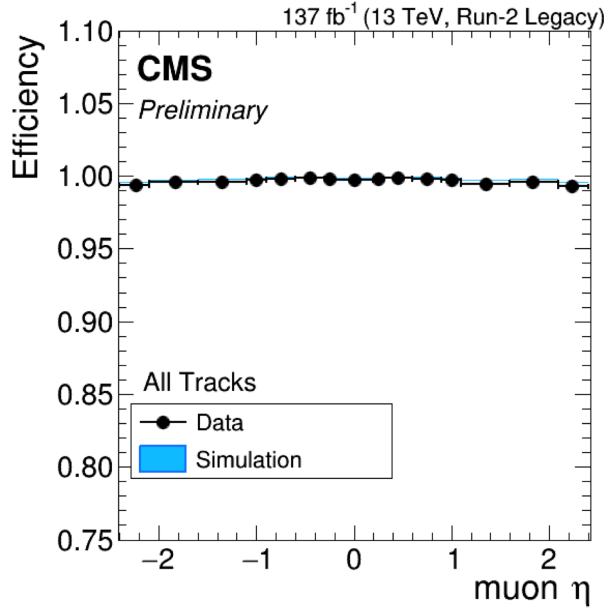


Figure 5.10: Muon tracking efficiencies as a function of  $|\eta|$  for standalone muons in Run-2 data (*black*) and Drell-Yan MC simulation (*blue*) [83]. All Tracks refers to tracks which exploit the presence of muon candidates in the muon system to seed the track reconstruction in the inner tracker, in contrast to tracks that use tracker-only hits for seeding. Uncertainties shown are statistical.

### 5.3.15 Drell-Yan corrections

The Z boson transverse momentum distribution disagrees between leading-order (LO) simulations and data in a  $Z \rightarrow \mu\mu$  control region with at least one b-tag jet [85]. Per-event weights derived by the 2016 data-only version of this analysis [85] are applied to  $Z \rightarrow \tau\tau/\ell\ell$  events, as a function of the generator-level Z boson  $p_T$  to provide better matching of MC to data.

### 5.3.16 Pile-up reweighting

Reweighting is performed to rescale MC events to account for differences between MC and data, in the distribution of the pile-up (number of additional proton-proton interactions per bunch crossing). A tool for calculating the pile-up reweighting for the MC samples used is provided centrally by the Luminosity POG [86].

1694 **5.3.17 Pre-firing corrections**

1695 In 2016 and 2017 data-taking, a gradual timing shift of ECAL was not properly  
1696 propagated to L1 trigger primitives (TPs), resulting in a large fraction of high  $\eta$   
1697 TPs being incorrectly associated with the previous bunch crossing. L1 trigger rules  
1698 prevent two consecutive bunch crossings from firing, causing events to be rejected if  
1699 significant ECAL energy was deposited in  $2.0 < |\eta| < 3.0$ . To account for this issue,  
1700 MC simulations for 2016 and 2017 are corrected using an event-dependent weight.  
1701 Embedded samples are not corrected [51].

1702 **5.3.18 Top  $p_T$  spectrum reweighing**

1703 In Run-1 and Run-2 it was observed that the  $p_T$  spectra of top quarks in  $t\bar{t}$  data  
1704 was significantly softer than those predicted by MC simulations [87]. Possible sources  
1705 of this discrepancy are higher order QCD and/or electroweak corrections, and non-  
1706 resonant production of  $t\bar{t}$ -like final states. To account for this, corrections derived  
1707 from Run-2 data by the Top Physics Analysis Group (PAG) are applied to the  $p_T$   
1708 of the top and anti-top quarks in MC simulations, computed as a function of their  
1709 generator-level  $p_T$  [87].

1710 **5.3.19 B-tagging efficiency**

1711 In order to predict correct b-tagging discriminant distributions and event yields in  
1712 data, the weight of selected MC events is reweighed according to recommendations by  
1713 the BTV POG [88]. The reweighing depends on the jet  $p_T$ ,  $\eta$ , and the b-tagging dis-  
1714 criminant. In this method, there is no migration of events from one b-tag multiplicity  
1715 bin to another.

1716 **5.3.20 Jet energy resolution and jet energy smearing**

1717 Calibration of jet energies, i.e. ensuring that the energy and momentum of the recon-  
1718 structed jet matches that of the quark/gluon-initiated jet, is a challenging task due  
1719 to time-dependent changes in the detector response and calibration and high pile-  
1720 up [89] [90]. Jet calibration is done via jet energy corrections (JECs) applied to the  
1721  $p_T$  of jets in MC samples, accounting successively for the effects of pile-up, uniformity  
1722 of the detector response, and residual data-simulation jet energy scale differences [91].  
1723 Typical jet energy resolutions reported at  $\sqrt{s} = 8$  TeV in the central rapidities are  
1724 15-20% at 30 GeV and about 10% at 100 GeV [89]. Jet energy corrections are also  
1725 propagated to the missing transverse energy.

1726 Measurements show that the jet energy resolution (JER) in data is worse than  
1727 in simulation, and so the jets in MC need to be smeared to describe the data. JER  
1728 corrections are applied after JEC on MC simulations, and adjust the width of the  $p_T$   
1729 distribution based on pile-up, jet size, and jet flavor [92]. Tools for applying JEC and  
1730 JER are provided centrally by the JER Corrections group.

# <sup>1731</sup> Chapter 6

## <sup>1732</sup> Event selection

<sup>1733</sup> This chapter describes how events in data and simulated samples are selected in the  
<sup>1734</sup> search for  $h \rightarrow aa \rightarrow bb\tau\tau$ . As described in the previous chapter, the tau lepton can  
<sup>1735</sup> decay to electrons ( $e$ ), muons ( $\mu$ ), or hadronic states ( $\tau_h$ ). As a result, several different  
<sup>1736</sup> final states of the  $\tau\tau$  system are possible, and are here referred to as “channels” since  
<sup>1737</sup> they are mutually exclusive. The three  $\tau\tau$  final states studied in this analysis are  
<sup>1738</sup> muon and hadronic tau ( $\mu\tau_h$ ), electron and hadronic tau ( $e\tau_h$ ), and electron and  
<sup>1739</sup> muon ( $e\mu$ ). The procedure for dividing events into these three channels begins with  
<sup>1740</sup> checking the High-Level Trigger paths passed by the events as detailed in Section 6.1.  
<sup>1741</sup> Events are further accepted or rejected based on criteria applied to the leptons in the  
<sup>1742</sup> event. These event selections are described for the  $\mu\tau_h$  channel in Section 6.2, the  $e\tau_h$   
<sup>1743</sup> channel in Section 6.3, and the  $e\mu$  channel in Section 6.4.

### <sup>1744</sup> 6.1 General procedure for all channels

<sup>1745</sup> For the search for  $h \rightarrow aa \rightarrow bb\tau\tau$ , three final states of the  $\tau\tau$  system are considered:  
<sup>1746</sup>  $\mu\tau_h$ ,  $e\tau_h$ , and  $e\mu$ . The  $\tau_h\tau_h$  final state is not considered because signal events in the  
<sup>1747</sup>  $\tau_h\tau_h$  channel would typically produce hadronic taus with momenta below data-taking  
<sup>1748</sup> trigger thresholds.

1749 In all three final states, events are required to have at least one b-tag jet passing the  
1750 medium working point of the DeepFlavour tagger, with  $p_T > 20$  GeV, and  $|\eta| < 2.4$ .  
1751 A second b-tag jet is not required because such a requirement would reduce signal  
1752 acceptance by 80% compared to only requiring one b-tag jet.

1753 Events in MC samples are sorted into one of the three  $\tau\tau$  channels if they pass the  
1754 following trigger requirements and requirements on the offline reconstructed objects  
1755 in the event, first checking the HLT paths for the  $\mu\tau_h$  channel, then  $e\tau_h$ , and finally  $e\mu$ .  
1756 The two leading leptons (e.g. muon and hadronic tau for the  $\mu\tau_h$  channel) that were  
1757 determined to have originated from the  $\tau\tau$  decay, are called the  $\tau\tau$  “legs”. For events  
1758 in data and embedded samples, the HLT paths requirements for the corresponding  
1759 channel are checked.

1760 After sorting events by HLT paths and identifying the leading tau legs in the offline  
1761 reconstructed objects, the  $p_T$  of the offline objects is checked against the online trigger  
1762 thresholds. Trigger matching is also performed, which checks the correspondence  
1763 between each offline reconstructed object used in the analysis (e.g. a muon), and a  
1764 trigger object in the HLT (e.g. a HLT muon). An offline object is considered to be  
1765 matched, if it corresponds to a trigger object of the same object type, with  $\Delta R < 0.5$ .  
1766 This matched trigger object is also required to pass the filter(s) of the HLT trigger.  
1767 The trigger thresholds used for the  $bb\mu\mu$  final state and the  $bb\tau\tau$  final state (the focus  
1768 of this work) are summarized in Tables 6.1.

1769 After checking the HLT paths and trigger objects in each channel, events are  
1770 subject to further selection to ensure that they contain leptons and b-tag jet(s) of in-  
1771 terest. These requirements are summarized in Table 6.2, and detailed in the following  
1772 sections.

Year	Single/dilepton trigger $p_T$	$bb\mu\mu$	$bb\tau\tau$					
			$e\mu$		$e\tau_h$		$\mu\tau_h$	
		$\mu$	$e$	$\mu$	$e$	$\tau_h$	$\mu$	$\tau_h$
2016	Single lepton	24	–	–	25	–	22	–
	$p_T$ -leading lepton	17	23	23	–	–	–	20
	$p_T$ -subleading lepton	8	12	8	–	–	19	–
2017	Single lepton	24	–	–	27, 32	–	24, 27	–
	$p_T$ -leading lepton	17	23	23	–	30	–	27
	$p_T$ -subleading lepton	8	12	8	24	–	20	–
2018	Single lepton	24	–	–	32, 35	–	24, 27	–
	$p_T$ -leading lepton	17	23	23	–	30	–	27
	$p_T$ subleading lepton	8	12	8	24	–	20	–

Table 6.1: Trigger thresholds used for the leptons in the  $bb\mu\mu$  analysis and the  $bb\tau\tau$  analysis (the focus of this work). The thresholds for the three  $bb\tau\tau$  channels ( $e\mu$ ,  $e\tau_h$ , and  $\mu\tau_h$ ) are listed separately, with some channels and years taking the logical OR of two triggers with different thresholds.

## 6.2 Event selection in the $\mu\tau_h$ channel

In all three years, a single muon trigger is used if the muon has sufficiently high  $p_T$ , otherwise a dilepton  $\mu\tau_h$  cross-trigger is used (Tables 6.3, 6.4, and 6.5). For data taken in 2017-2018 (2016), the logical OR of the single muon triggers with online  $p_T$  thresholds 24 and 27 (23) GeV is used, with the corresponding offline muon required to have with  $p_T$  1 GeV above the online threshold. For data taken in 2017-2018 (2016), a dilepton  $\mu + \tau_h$  cross-trigger with  $p_T$  thresholds of 20 (19) and 27 (20) GeV for the muon and tau respectively, is used. The  $\tau_h$  is required to have  $|\eta| < 2.3$  if the single trigger is fired,  $|\eta| < 2.1$ .

The muon and  $\tau_h$  are required to have opposite charge and be separated by  $\Delta R > 0.4$ . The muon is required to have  $|\eta| < 2.4$ , and the  $\tau_h$  is required to have  $|\eta| < 2.3$  unless a cross-trigger is required, in which case we require  $|\eta| < 2.1$  as discussed above.

The muon is required to pass the medium identification (ID) working point [93], which is defined by the Muon POG as a loose muon (i.e. a Particle Flow muon that is either a global or a tracker muon - see Section 5.1.2) with additional requirements

All years (2016, 2017, 2018) and eras				
Kinematic variable	$bb\mu\mu$		$bb\tau\tau$	
	$\mu$	$e\mu$	$e\tau_h$	$\mu\tau_h$
$\Delta R$ between leptons	>0.4	>0.3	>0.4	>0.4
$ \eta $ of electron	-	<2.4	<2.1	-
$ \eta $ of muon	<2.4	<2.4	-	<2.1
$ \eta $ of hadronic tau	-	-	<2.3/< 2.1	<2.3/< 2.1
Relative isolation of electron	-	<0.10	-	<0.15
Relative isolation of muon	<0.25	<0.15	-	<0.15
Leading b-tag jet $p_T$	>15 GeV		>20 GeV	
Leading b-tag jet $ \eta $	<2.4		<2.4	
Leading b-tag jet WP	Tight		Medium	
Sub-leading b-tag jet $p_T$	>15 GeV		-	
Sub-leading b-tag jet $ \eta $	<2.4		-	
Sub-leading b-tag jet WP	Loose		-	
$\Delta R$ between jet(s) and leptons	>0.4		>0.5	

Table 6.2: Summary of requirements applied to the leptons in the  $bb\mu\mu$  analysis and the  $bb\tau\tau$  analysis (the focus of this work).  $\Delta R = \sqrt{(\Delta\eta)^2 + (\Delta\phi)^2}$  is a measure of spatial separation. Relative isolation is defined in Eqn. 5.2 and Section 5.1.2. The b-tag jets are required to pass the listed DeepFlavour working points (WP), which are described in Section 5.1.5. In the  $bb\tau\tau$  analysis, the required  $|\eta|$  of the hadronic taus are listed for the single and cross triggers respectively. The  $bb\mu\mu$  analysis requires two b-tag jets in all events, while the  $bb\tau\tau$  analysis only requires one.

1789 on track quality and muon quality. This identification criteria is designed to be  
1790 highly efficiently for prompt muons and for muons from heavy quark decays. In  
1791 addition to the ID, for prompt muons it is recommended to apply cuts on the impact  
1792 parameter [93]: we apply  $|\Delta(z)| < 0.2$  and  $|\Delta(xy)| < 0.045$ .

1793 In addition, a cut is applied on the muon relative isolation (defined in Section  
1794 5.1.2), to be less than 0.15 in a cone size of  $\Delta R = 0.4$ , which corresponds to the  
1795 Tight Particle Flow isolation requirement [93].

1796 The  $\tau_h$  is required to pass a cut on its impact parameter of  $|\Delta(z)| < 0.2$ . The  $\tau_h$   
1797 is also required to pass the VLoose (Very Loose) DeepTau working point vs. elec-  
1798 tron, the Tight DeepTau working point vs. muons, and the VVVLoose and Medium  
1799 DeepTau working point vs. jets. Events with taus reconstructed in two of the decay  
1800 modes (labeled 5 and 6) are rejected, since these decay modes are meant to recover  
1801 3-prong taus, but are only recommended for use in analyses where the benefits in  
1802 final significance outweigh the resulting increase in background [66].

1803 For the estimation of the background from jets faking  $\tau_h$ , which is described in Sec-  
1804 tion 7.7, anti-isolated events are selected, by requiring events to pass all the selections  
1805 described above, except failing the Medium DeepTau working point vs. jets.

### 1806 6.3 Event selection in the $e\tau_h$ channel

1807 The HLT trigger paths for the  $e\tau_h$  channel are summarized in Tables 6.3, 6.4, and  
1808 6.5. Similarly to the  $\mu\tau_h$  channel, a single electron trigger is used if the electron has  
1809 sufficiently high  $p_T$  in 2018 and 2017. For data taken in 2018 (2017), the OR of the  
1810 single electron triggers with online  $p_T$  thresholds at 32 and 35 (27 and 32) GeV are  
1811 used, with the corresponding offline electrons required to have  $p_T$  greater than 33  
1812 (28) GeV. A  $e + \tau_h$  cross-trigger is used for electrons with lower offline  $p_T$  between  
1813 25 and 33 GeV (25 and 28 GeV). For the 2016 dataset, there is no cross trigger but

1814 only a single electron trigger with online  $p_T$  threshold at 25 GeV, which is used if the  
1815 offline electron has  $p_T$  greater than 26 GeV.

1816 The electron and  $\tau_h$  are required to have opposite charge and be separated by  
1817  $\Delta R > 0.4$ . The electron is required to be within  $|\eta| < 2.3$  when no cross trigger is  
1818 used, and  $|\eta| < 2.1$  when the cross trigger is fired. The  $\tau_h$  is required to have  $|\eta| < 2.3$   
1819 if no cross trigger is fired, and have  $|\eta| < 2.1$  if the cross trigger is fired.

1820 The electron is required to have a relative isolation (same definition as in Section  
1821 5.1.2) of less than 0.1 in a cone size of  $\Delta R = 0.3$ , which is the standard recommended  
1822 cone size giving minimal pile-up dependence and reduced probability of other objects  
1823 overlapping with the cone. The isolation quantity used includes an “effective area”  
1824 (EA) correction to remove the effect of pile-up in the barrel and endcap parts of the  
1825 detector [94].

1826 The electron is also required to pass cuts on its impact parameter of  $|\Delta(z)| < 0.2$   
1827 and  $|\Delta(xy)| < 0.045$ . It is also required to pass the non-isolated MVA working point  
1828 corresponding to 90% efficiency. The electron’s number of missing hits, which are  
1829 gaps in its trajectory through the inner tracker [94], must be less than or equal to  
1830 1. The electron must pass a conversion veto, which rejects electrons coming from  
1831 photon conversions in the tracker, which should instead be reconstructed as part of  
1832 the photon [94].

1833 The impact parameter cut for the  $\tau_h$  is  $|\Delta(z)| < 0.2$ . In contrast to the  $\mu\tau_h$  event  
1834 selection, the vs. electron and vs. muon DeepTau working points are flipped, to  
1835 reject muons faking the  $\tau_h$  leg. The  $\tau_h$  is required to pass the Tight DeepTau working  
1836 point vs. electrons, the VLoose DeepTau working point vs. muons, and the Medium  
1837 DeepTau working point vs. jets.

1838 As in the  $\mu\tau_h$  channel, for the estimation of the background from jets faking  $\tau_h$ ,  
1839 which is described in Section 7.7, anti-isolated events are selected, by requiring events  
1840 to pass all the selections described above, except failing the Medium DeepTau working

1841 point vs. jets.

## 1842 6.4 Event selection in the $e\mu$ channel

1843 The HLT trigger paths for the  $e\mu$  channel are summarized in Tables 6.3, 6.4, and  
1844 6.5. Events are selected with the logical OR of two  $e + \mu$  cross triggers, where either  
1845 the electron or muon can have larger  $p_T$ : (1) leading electron, where the electron has  
1846 online  $p_T > 23$  GeV and muon has online  $p_T > 8$  GeV, or (2) leading muon, where  
1847 electron has online  $p_T > 12$  GeV and muon has online  $p_T > 23$  GeV.

1848 The leading and sub-leading leptons are required to have an offline  $p_T$  greater  
1849 than 1 GeV above the online threshold (i.e.  $p_T > 24$  GeV). If the sub-leading lepton  
1850 is the electron, the offline  $p_T$  threshold is 1 GeV above the online threshold ( $p_T > 13$   
1851 GeV), but if it is a muon, the offline  $p_T$  threshold is required to be at least 5 GeV  
1852 greater than the online threshold (i.e.  $p_T > 13$  GeV). This is because of poor data  
1853 and simulation agreement for low- $p_T$  muons with  $p_T$  between 9 GeV and 13 GeV, and  
1854 the higher probability of mis-identifying jets as muons at lower  $p_T$ . With no effect on  
1855 the expected limits, the offline  $p_T$  threshold for muons is raised to 13 GeV instead of  
1856 9 GeV, even though it may lead to loss in signal acceptance. Both the electron and  
1857 muon are required to have  $|\eta| < 2.4$ .

1858 The electron and muon are required to have opposite charge and be separated  
1859 by  $\Delta R > 0.3$  (note the decreased separation requirement compared to the other  
1860 two channels). The electron is required to pass the non-isolated MVA identification  
1861 working point corresponding to 90% efficiency, and to have a relative isolation less  
1862 than 0.1 for a cone size of  $\Delta R = 0.3$  with the EA pile-up subtraction correction.  
1863 The electron must have one or fewer missing hits and pass the conversion veto (both  
1864 described previously in Section 6.3).

1865 The muon is required to pass the medium identification working point (described

earlier in 6.2), and to have a relative isolation less than 0.15 for a cone size of  $\Delta R = 0.4$ . The muon impact parameter is required to have  $|\Delta(z)| > 0.2$  and  $|\Delta(xy)| < 0.045$ .

For the QCD multijet background estimation described in Section 7.8, the same-sign region is selected by requiring all the above selections, except the legs are required to have the same electric charge rather than opposite.

2016 $\mu\tau_h$ trigger paths	
Notes	HLT Path
	HLT_IsoMu22_v
	HLT_IsoMu22_eta2p1_v
	HLT_IsoTkMu22_v
	HLT_IsoTkMu22_eta2p1_v
	HLT_IsoMu19_eta2p1_LooseIsoPFTau20_v
	HLT_IsoMu19_eta2p1_LooseIsoPFTau20_SingleL1_v
2016 $e\tau_h$ trigger paths	
Notes	HLT Path
	HLT_Ele25_eta2p1_WPTight_Gsf_v
2016 $e\mu$ trigger paths	
Notes	HLT Path
runs B-F and MC	HLT_Mu23_TrkIsoVVL_Ele12_CaloIdL_TrackIdL_IsoVL_v
runs B-F and MC	HLT_Mu8_TrkIsoVVL_Ele23_CaloIdL_TrackIdL_IsoVL_v
runs G-H	HLT_Mu23_TrkIsoVVL_Ele12_CaloIdL_TrackIdL_IsoVL_DZ_v
runs G-H	HLT_Mu8_TrkIsoVVL_Ele23_CaloIdL_TrackIdL_IsoVL_DZ_v

Table 6.3: High-Level Trigger (HLT) paths used to select data and simulation events in 2016 for the three  $\tau\tau$  channels.

## 6.5 Extra lepton vetoes in all channels

Events containing a third lepton (electron or muon) that is neither of the leading  $\tau\tau$  legs are rejected, and events with di-muons and di-electrons are vetoed, with criteria taken from the Standard Model  $H \rightarrow \tau\tau$  working group [69].

The event is vetoed if a third electron is found with the following properties:  $p_T > 10$  GeV,  $|\eta| < 2.5$ , impact parameter  $|\Delta(z)| < 0.2$  and  $|\Delta(xy)| < 0.045$ , passing non-isolation MVA identification with 90% efficiency, conversion veto,  $\leq 1$  missing

2017 $\mu\tau_h$ trigger paths	
Notes	HLT Path
	HLT_IsoMu24_v
	HLT_IsoMu27_v
	HLT_IsoMu20_eta2p1_LooseChargedIso_PFTau27_eta2p1_CrossL1_v
2017 $e\tau_h$ trigger paths	
Notes	HLT Path
	HLT_Ele32_WPTight_Gsf_v
	HLT_Ele35_WPTight_Gsf_v
	HLT_Ele24_eta2p1_WPTight_Gsf_Loose_ChargedIsoPFTau30_eta2p1_CrossL1_v
2017 $e\mu$ trigger paths	
Notes	HLT Path
	HLT_Mu23_TrkIsoVVL_Ele12_CaloIdL_TrackIdL_IsoVL_DZ_v
	HLT_Mu8_TrkIsoVVL_Ele23_CaloIdL_TrackIdL_IsoVL_DZ_v

Table 6.4: High-Level Trigger (HLT) paths used to select data and simulation events in 2017 for the three  $\tau\tau$  channels.

1878 hits, and relative isolation  $< 0.3$  with cone size  $\Delta R = 0.3$ . The event is also vetoed if  
 1879 a third muon is found with the following properties:  $p_T > 10$  GeV,  $|\eta| < 2.4$ , impact  
 1880 parameter  $|\Delta(z)| < 0.2$  and  $|\Delta(xy)| < 0.045$ , medium ID, and isolation  $< 0.3$  with  
 1881 cone size  $\Delta R = 0.4$ .

1882 A di-muon veto is applied, which rejects events containing a pair of muons with  
 1883 opposite charge and separation of  $\Delta R > 0.15$ , that both pass the following selections:  
 1884  $p_T > 15$  GeV,  $|\eta| < 2.4$ , flag for global muons, flag for tracker muon, flag for Particle  
 1885 Flow muon,  $|\Delta(z)| < 0.2$ ,  $|\Delta(xy)| < 0.045$ , and isolation  $< 0.3$  with cone size  $\Delta R =$   
 1886 0.4. A similar di-electron veto is applied to reject events containing a pair of electrons  
 1887 with opposite charge and separation of  $\Delta R > 0.15$ , that both pass the following  
 1888 selections:  $p_T > 15$  GeV,  $|\eta| < 2.5$ , a dedicated electron ID (cut-based) for vetoing  
 1889 third leptons,  $|\Delta(z)| < 0.2$ ,  $|\Delta(xy)| < 0.045$ , with pile-up corrected relative isolation  
 1890  $< 0.3$  with cone size  $\Delta R = 0.3$ .

1891 These vetoes on extra leptons also ensure orthogonality of events to analyses such  
 1892 as the  $bb\mu\mu$  final state, whose results are combined with this  $bb\tau\tau$  final state as  
 1893 described in Section 10.2.

2018 $\mu\tau_h$ trigger paths	
Notes	HLT Path
	HLT_IsoMu24_v
	HLT_IsoMu27_v
only data run < 317509	HLT_IsoMu20_eta2p1_ (contd.)
	LooseChargedIsoPFTauHPS27_eta2p1_CrossL1_v
MC and data run $\geq$ 317509	HLT_IsoMu20_eta2p1_ (contd.)
	LooseChargedIsoPFTauHPS27_eta2p1_TightID_CrossL1_v
2018 $e\tau_h$ trigger paths	
Notes	HLT Path
	HLT_Ele32_WPTight_Gsf_v
	HLT_Ele35_WPTight_Gsf_v
only data run < 317509	HLT_Ele24_eta2p1_WPTight_Gsf_ (contd.)
	LooseChargedIsoPFTauHPS30_eta2p1_CrossL1_v
MC and data run $\geq$ 317509	HLT_Ele24_eta2p1_WPTight_Gsf_ (contd.)
	LooseChargedIsoPFTauHPS30_eta2p1_TightID_CrossL1_v
2018 $e\mu$ trigger paths	
Notes	HLT Path
	HLT_Mu23_TrkIsoVVL_Ele12_CaloIdL_TrackIdL_IsoVL_DZ_v
	HLT_Mu8_TrkIsoVVL_Ele23_CaloIdL_TrackIdL_IsoVL_DZ_v

Table 6.5: High-Level Trigger (HLT) paths used to select data and simulation events in 2018 for the three  $\tau\tau$  channels. In 2018 a HLT trigger path using the hadron plus strips (HPS) tau reconstruction algorithm became available.

1894 **Chapter 7**

1895 **Background estimation**

1896 This section describes methods used to estimate sources of background from Standard  
1897 Model processes in the search for  $h \rightarrow aa \rightarrow bb\tau\tau$ . Similar background estimation  
1898 methods are being used for the  $h \rightarrow a_1a_2$  analysis. The background contributions  
1899 directly taken from MC are described in Sections 7.1 to 7.6. Section 7.7 describes  
1900 the data-driven method for estimating backgrounds from jets faking hadronic tau  
1901 decays ( $\text{jet} \rightarrow \tau_h$ ), which is used in the  $\mu\tau_h$  and  $e\tau_h$  channels. Section 7.8 describes  
1902 the data-driven method for estimating background from quantum chromodynamic  
1903 (QCD) processes in the  $e\mu$  channel.

1904 **7.1 Z+jets**

1905 A major source of background for  $\tau\tau$  analyses is the Drell-Yan (DY) process (Z+jets).  
1906 The Z boson decays to  $\tau\tau/\mu\mu/ee$  with equal probability of 3.4% each, with the domi-  
1907 nant decay modes being to hadrons (around 70%) and neutrinos (invisible) (20%) [26].  
1908 The Drell-Yan contribution with genuine taus,  $Z \rightarrow \tau\tau$ , is estimated using embed-  
1909 ded samples, described in Section 4.3. To avoid double-counting between embedded  
1910 and MC samples, in all MC samples, events with legs that originated from genuine  $\tau$   
1911 are discarded.

1912      The other decays of the  $Z$ ,  $Z \rightarrow ee$  and  $Z \rightarrow \mu\mu$ , are estimated from MC simulation,  
1913 and are hereafter referred to as simply the Drell-Yan background. These MC samples  
1914 are generated to leading order (LO) with different numbers of jets (jet multiplicity) in  
1915 the matrix element:  $Z+1$  jet,  $Z+2$  jets,  $Z+3$  jets,  $Z+4$  jets, and inclusive  $Z+jets$ . The  
1916 cross-sections of the samples with  $\geq 1$  jets are normalized to next-to-NLO (NNLO)  
1917 in QCD.

1918      For the inclusive Drell-Yan sample, two samples are used with different thresholds  
1919 for the di-lepton invariant mass ( $m_{\ell\ell}$ ) at the generator level: one with  $m_{\ell\ell} > 50$  GeV  
1920 and the other with  $10 < m_{\ell\ell} < 50$ .

## 1921 **7.2 W+jets**

1922      The dominant  $W$  boson decay modes are to hadrons (67.4%),  $e + \nu_e$  (10.7%),  $\mu + \nu_\mu$   
1923 (10.6%), and  $\tau + \nu_\tau$  (11.4%) [26]. The  $W+jets$  background is estimated from MC  
1924 simulation. Similarly to the  $Z+jets$ , the  $W+jets$  samples are generated with different  
1925 jet multiplicities in the matrix element. LO samples are used for greater statistics  
1926 and are normalized to NNLO cross sections.

## 1927 **7.3 $t\bar{t} + jets$**

1928      In hadron collisions, top quarks are produced singly with the weak interaction, or in  
1929 pairs via the strong interaction, with interference between these leading-order pro-  
1930 cesses possible in higher orders of the perturbation theory. The top quark is the  
1931 heaviest fermion in the Standard Model and has a short lifetime ( $\sim 10^{-25}$  s), decay-  
1932 ing without hadronization into a bottom quark and a  $W$  boson [26], with the decay  
1933 modes of the  $W$  boson as listed in the previous section. With two top quarks, the  
1934 final states of the two resulting  $W$  bosons can be described as fully leptonic, semilep-  
1935 tonic, and fully hadronic. These three final states are modeled separately with MC

1936 simulation in 2018 and 2017, while for 2016 the sample used is inclusive.

## 1937 7.4 Single top

1938 There are three main production modes of the single top in  $pp$  collisions [95]: the  
1939 exchange of a virtual W boson ( $t$  channel), the production and decay of a virtual W  
1940 boson ( $s$  channel), and the associated production of a top quark and W boson ( $tW$ ,  
1941 or W-associated) channel. As the  $s$  channel process is rare and only 3% of the total  
1942 production, the dominant production mode of the  $t$ -channel and the  $tW$  production  
1943 are considered and modeled with MC.

## 1944 7.5 Diboson

1945 In  $pp$  collisions, the production of dibosons (pairs of electroweak gauge bosons, i.e.  
1946 WW, WZ, and ZZ) is dominated by quark-antiquark annihilation, with a small con-  
1947 tribution from gluon-gluon interaction [96]. MC is used to model the pair production  
1948 and decays of VV to  $2\ell 2\nu$ , WZ to  $2q 2\ell$  and  $3\ell\nu$ , and ZZ to  $4\ell$  and  $2q 2\ell$  ( $q$  being  
1949 quarks and  $\ell$  being leptons).

## 1950 7.6 Standard Model Higgs

1951 MC is used to simulate backgrounds from major production modes of the Standard  
1952 Model 125 GeV Higgs boson: gluon-gluon fusion (ggH), vector boson fusion (VBF),  
1953 associated production with a W or Z (WH, ZH), and associated production with a  
1954 top pair (ttH) (see Fig. 7.1 for leading-order diagrams). For these production modes,  
1955 samples with the Higgs decaying to  $\tau\tau$  or to  $WW$  are used. Samples made with  
1956 higher-order diagrams for WH and ZH that include the production of a jet, with the  
1957 Higgs decaying to WW, are also used.

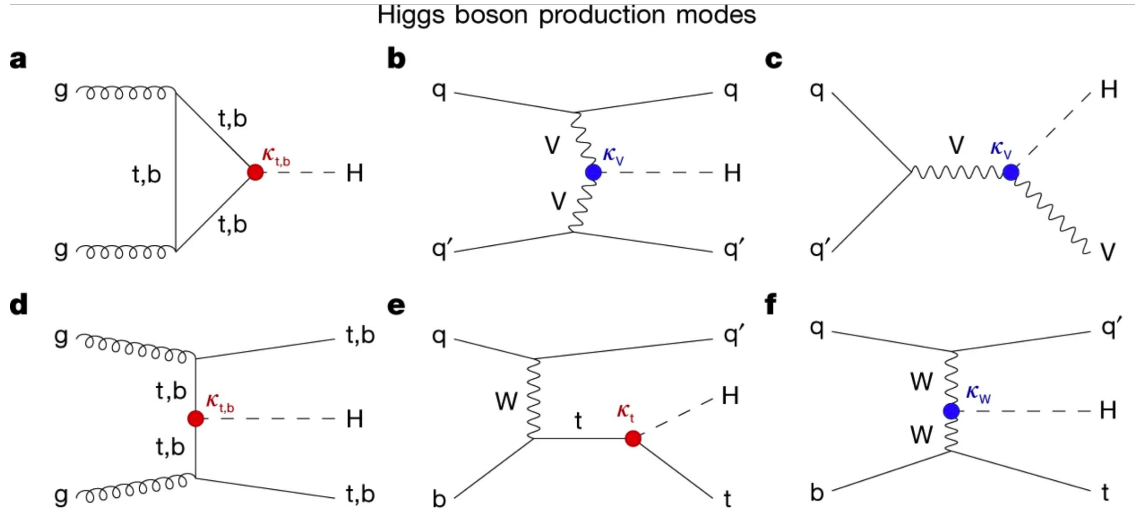


Figure 7.1: Leading-order Feynman diagrams of Higgs production from [97], in ggH (a) and vector boson fusion (VBF; b), associated production with a W or Z (V) boson (VH; c), associated production with a top or bottom quark pair (ttH or bbH); d, and associated production with a single top quark (tH; e, f).

## 1958 7.7 Jet faking $\tau_h$

1959 Events with a jet mis-reconstructed as the hadronic tau leg  $\tau_h$  are a major source of  
 1960 background in the  $\mu\tau_h$  and  $e\tau_h$  channels. The main processes contributing to jet  $\rightarrow \tau_h$   
 1961 events are QCD multijet, W+jets, and  $t\bar{t}$  production. These events are estimated  
 1962 using a data-driven method adapted from past analyses [51] [85]. This background  
 1963 includes contributions from W+jets, QCD multijets, and  $t\bar{t}$ +jets. To estimate this  
 1964 background, a sideband region is constructed, where events are required to pass all  
 1965 baseline  $\mu\tau_h/e\tau_h$  selection criteria, but fail the  $\tau_h$  isolation criteria. The events in  
 1966 this sideband region is reweighed with a factor  $f/(1 - f)$ , where  $f$  is the probability  
 1967 for a jet to be misidentified as a  $\tau_h$ . The jet  $\rightarrow \tau_h$  background is the anti-isolated,  
 1968 reweighed MC and embedded events subtracted from the anti-isolated, reweighted  
 1969 data events.

1970 The fake factor is measured in  $Z \rightarrow \mu\mu + \text{jets}$  events in data in the  $\mu\mu\tau_h$  final  
 1971 state, as any reconstructed  $\tau_h$  in these events must originate from a jet. The two  
 1972 muons are required to be isolated ( $< 0.15$ ), have opposite electric charge, and have

1973 an invariant mass between 76 and 106 GeV (close to the Z mass). These events are  
1974 selected with a double muon trigger, with the leading muon having offline  $p_T > 20$   
1975 GeV and the subleading muon  $p_T > 10$  GeV. Simulated diboson (ZZ and WZ) events  
1976 are subtracted to avoid contamination from events with real  $\tau_h$ . The denominator of  
1977 the fake rate corresponds to fake taus passing the VVVLoose working point of the  
1978 discriminator vs. jets, while the numerator corresponds to those passing the Medium  
1979 working point, i.e.  $f = N_{\text{jet passing tight}} / N_{\text{jet passing loose}}$ .

1980  $f$  is measured as a function of the  $\tau_h$  transverse momentum and is 8% - 10% in  
1981 each of the data-taking years.  $f$  is derived separately for the  $\mu\tau_h$  and  $e\tau_h$  channels  
1982 because the channels use different anti-lepton identification working points.

## 1983 7.8 QCD multijet background

1984 In the  $e\mu$  channel, events with jets faking electrons or muons originating from QCD  
1985 multijet, is estimated from data events with the same baseline selection as in the  
1986 signal region, except with same-signed (SS) charged  $e + \mu$ , ensuring orthogonality  
1987 with the signal region which requires opposite-sign (OS)  $e\mu$  pairs. All same-sign MC  
1988 events (both events with real and fake  $e + \mu$ ) are subtracted from same-sign data  
1989 events to remove contamination from other backgrounds. i.e.  $\text{QCD}_{\text{SS}} = \text{Data}_{\text{SS}} -$   
1990  $\text{MC}_{\text{SS}}$ .

1991 Three scale factors are applied to the  $\text{QCD}_{\text{SS}}$  events to compute the QCD multijet  
1992 background [85] [40]:

- 1993 • *OS-to-SS scale factor*: This scales the SS QCD to the OS region, and is mea-  
1994 sured from an orthogonal region with an isolated electron and an anti-isolated  
1995 muon. Only the muon is chosen to be anti-isolated because this scale factor was  
1996 observed to depend more strongly on electron isolation than that of the muon.  
1997 This scale factor is treated as a function of the  $\Delta R$  separation of the trajectories

1998 of the electron and muon, and is measured separately for events with 0 jets, 1,  
1999 jet, and greater than 1 jet.

- 2000 • *2D closure correction for the lepton  $p_T$ :* This factor accounts for subleading  
2001 dependencies of the first scale factor on the  $p_T$  of the two leptons. A 2D weight  
2002 is derived in a similar fashion, as a ratio of  $\text{QCD}_{OS}$  events to  $\text{QCD}_{SS}$  events,  
2003 but parameterized by both electron and muon  $p_T$ , where the SS events have the  
2004 previous scale factor applied.
- 2005 • *Isolation correction for the muon:* The third and final factor is an isolation  
2006 correction, which is a bias correction to account for the fact that the fake  
2007 factor was determined for less-isolated muons. This factor is obtained as the  
2008 ratio of the OS-to-SS scale factors measured in two other control regions: (1)  
2009 events where the electron is anti-isolated ( $0.15 < \text{iso} < 0.5$ ) and the muon is  
2010 isolated, and (2) events where both leptons are anti-isolated.

# 2011 Chapter 8

## 2012 Systematic uncertainties

2013 The handling of systematic uncertainties is separated into normalization uncertainties  
2014 (those that affect the total yield of a variables' distribution) and shape uncertainties  
2015 (those that shift the distribution of events). Normalization uncertainties are expressed  
2016 as multiplicative factors, while shape uncertainties are represented as up and down  
2017 shifts of a variable's distribution.

2018 Up/down shifts of shape uncertainties can change the number of background  
2019 events in a distribution. For instance, hadronic taus receive corrections from the  
2020 nominal tau energy scale, with the nominal, up, and down energy scales provided  
2021 centrally by CMS. For the  $\mu\tau_h$  channel, an event could have a  $\tau_h$  with  $p_T$  just below  
2022 the offline threshold of 20 GeV (for instance, 19.5 GeV), so in the nominal distribution  
2023 of  $m_{\tau\tau}$  (or any other variable for this channel), the event is excluded. However, when  
2024 we build our distributions with the tau energy scale “up” shift, the energy of this  $\tau_h$   
2025 may be scaled up to, say, 20.5 GeV, and now the event passes the offline  $p_T$  threshold  
2026 for the single muon trigger, leading to the event's inclusion in the distributions made  
2027 with the tau energy scale “up” shift.

2028 In evaluating the up and down shifts of a specific source of uncertainty, all other  
2029 corrections and scale factors are held at their nominal values, and the full chain of

2030 object and event selection and event categorization is performed to obtain the observ-  
2031 able distributions. Any “downstream” variables that depend on the shifted variable,  
2032 e.g. the invariant di-tau mass  $m_{\tau\tau}$ , must be computed for the nominal case, and then  
2033 re-computed separately for each up and down shift of the tau legs’ energy scale. The  
2034 objective of this process is to quantify the effect of a single source of uncertainty on  
2035 the resulting observable distributions. Each scale factor and correction described in  
2036 Section 5.3 has an associated uncertainty. The binning of the uncertainties follows  
2037 that of the nominal scale factor value.

2038 Sections 8.1 to 8.5 describe uncertainties associated with physics objects, and  
2039 Sections 8.6 and 8.7 describe uncertainties associated with sample-level effects. The  
2040 pulls and impacts for the top sixty most important systematics are shown in Section  
2041 8.8.

## 2042 8.1 Uncertainties in the lepton energy scales

2043 The uncertainties in the tau energy scales [66] are binned by the tau decay mode and  
2044 are taken as shape uncertainties treated as uncorrelated across the tau decay modes  
2045 and years. Same as with the application of the nominal scale factor, when applying  
2046 the up or down shifts, the missing transverse energy ( $p_T^{\text{miss}}$ ) of the event is adjusted  
2047 so that the 4-vector sum of the tau  $p_T^{\text{miss}}$  is unchanged.

2048 The uncertainties in the muon energy scale [67] are 0.4% for  $|\eta| < 1.2$ , 0.9% for  
2049  $1.2 < |\eta| < 2.1$ , and 2.7% for  $2.1 < |\eta| < 2.4$ , and are treated as shape uncertainties,  
2050 fully uncorrelated between embedded and MC samples.

2051 The uncertainties in the electron energy scale [70] in MC are binned in the electron  
2052  $|\eta|$  and  $p_T$ , and are shown in Fig. 5.2. The uncertainties range from 0.5% to 2.2% in  
2053 the barrel, and 0.3% to 4.1% in the endcap, across the  $p_T$  range. The uncertainties  
2054 for the embedded sample are binned only in  $|\eta|$  and are on the order of 0.5% and

2055 1.25% for the barrel and endcap [74].

2056 There are also uncertainties in the energy scales for electrons and muons misiden-  
2057 tified as  $\tau_h$ . The uncertainty for muons misidentified as  $\tau_h$  is 1% [66]. For electrons  
2058 misidentified as  $\tau_h$ , the uncertainty is binned in barrel/endcap  $\eta$  and by 1-prong and  
2059 1-prong +  $\pi_0$  decays. The probability for  $e/\mu$  faking a 3-prong decay mode is much  
2060 lower.

## 2061 8.2 Uncertainties from other lepton corrections

2062 Uncertainties associated with the  $\tau_h$  identification efficiencies are treated as shapes,  
2063 uncorrelated across the seven  $p_T$  bins and years. The shape uncertainties in the  
2064 embedded samples are taken as 50% correlated with those of the MC samples.

2065 The uncertainties on electron and muon identification efficiencies are taken as  
2066 normalization uncertainties of 2% each, with a 50% correlation between embedded  
2067 and MC samples.

2068 In the  $e\tau_h$  channel, there is an additional uncertainty for the vs. jet discrimination  
2069 efficiency [66], because the analysis uses a looser anti-lepton working point (VLoose  
2070 WP) than the working points used in the measurement of the efficiency (namely,  
2071 VLoose WP vs e, and Tight WP vs mu). For nominal  $\tau_h p_T < 100$  GeV, an additional  
2072 uncertainty of 3% (5%) is used in MC (embedded), and for high  $p_T$  an uncertainty of  
2073 15% is used for both.

2074 The uncertainties in trigger efficiencies are taken as shapes [66]. In the  $e\tau_h$  and  $\mu\tau_h$   
2075 channels, there are uncertainties for the single and cross lepton triggers, and in the  
2076  $e\mu$  channel there is one uncertainty each for the two  $e + \mu$  triggers, and one combined  
2077 uncertainty since their trigger phase spaces are not mutually exclusive.

2078    **8.3 Uncertainties from jet energy scale and reso-**  
2079    **lution**

2080    The jet energy scale uncertainties are taken as shape uncertainties: there are eleven  
2081    in total, with seven correlated across years (labeled “Year” below) and the remainder  
2082    uncorrelated across years. They affect the b-tag jet  $p_T$  and mass, and hence the  
2083    missing transverse energy  $p_T^{\text{miss}}$ . The shifts are propagated through the b-tagging  
2084    scale factor calculation and b-tag jet counting.

2085    The uncertainties in the jet energy correction and resolution [89] [98] are as follows:

- 2086    • *Absolute, AbsoluteYear*: flat absolute scale uncertainties.
- 2087    • *BBEC1, BBEC1Year*: for sub-detector regions, with barrel “BB” in  $|\eta| < 1.3$   
2088    and endcap region 1 “EC1”:  $1.3 < |\eta| < 2.5$ .
- 2089    • *EC2, EC2 year*: for sub-detector regions, with endcap region 2 “EC2” in  $2.5 <$   
2090     $|\eta| < 3.0$ .
- 2091    • *HF, HF year*: for sub-detector regions, with hadron forward “HF” in  $|\eta| > 3$ .
- 2092    • *FlavorQCD*: for uncertainty in jet flavor (uds/c/b-quark and gluon) estimates  
2093    based on comparing Pythia and Herwig (different MC generator) predictions.
- 2094    • *RelativeBal*: account for difference between log-linear fits of the two methods  
2095    used to study the jet energy response: MPF (missing transverse momentum  
2096    projection fraction) and  $p_T$  balance.
- 2097    • *RelativeSample*: account for  $\eta$ -dependent uncertainty due to a difference be-  
2098    tween relative residuals, observed with dijet and Z+jets in Run D of 2018 data.
- 2099    • *JetResolution*: uncertainty in the jet energy resolution.

## 2100 8.4 Uncertainties from b-tagging scale factors

2101 The b-tagging scale factor has its own set of associated uncertainties (not to be  
2102 confused with shifts in the b-tagging scale factor due to the propagation of the jet  
2103 energy scale uncertainties described in the previous section 8.3). They are:

- 2104 •  $hf$ : contamination from heavy flavor ( $b+c$ ) jets in the light flavor region.
  - 2105 •  $hfstats1, hfstats2$ : linear and quadratic statistical fluctuations from  $b$ -flavor jets.
  - 2106 •  $lf$ : contamination from light flavor ( $udsg+c$  jets) in the heavy flavor region.
  - 2107 •  $lfstats1, lfstats2$ : linear and quadratic statistical fluctuations from  $udsg$  jets.
  - 2108 •  $cferr, cferr2$ : uncertainty for charm jets.
- 2109 The variations for “ $lf, hf, hfstats1/2, lfstats1/2$ ” are applied to both  $b$  and  $udsg$  jets.
- 2110 For  $c$ -flavor jets, only “ $cferr1/2$ ” is applied.

## 2111 8.5 Uncertainties from MET

2112 Samples where recoil corrections were applied ( $Z+jets$ ,  $W+jets$ , and Standard Model  
2113 Higgs, as described in Section 5.3) have uncertainties from the response and resolution  
2114 of the hadronic recoil against the leptonic system. These are each binned in jet  
2115 multiplicity.

## 2116 8.6 Uncertainties associated with samples used

2117 Normalization uncertainties related to the samples used are:

- 2118 • *Cross-section uncertainties*:  $\sigma(t\bar{t})$ : 4.2%,  $\sigma(\text{diboson})$ : 5%,  $\sigma(\text{single top})$ : 5%,  
2119  $\sigma(\text{ggH})$ : 3.2%,  $\sigma(\text{qqH})$ : 2.1%,  $\sigma(\text{WH})$ : 1.9%,  $\sigma(\text{ZH})$ : 1.3%,  $\sigma(\text{ttH})$ : 3.6%

2120 • *Uncertainties in QCD renormalization scale*: QCD scale(qqH): +0.43%-0.33%,

2121 QCD scale(WH): +0.5%-0.7%, QCD scale(ttH): +5.8%-9.2%

2122 • *Branching ratio uncertainties*: BR( $H \rightarrow \tau\tau$ ): 1.8%, and BR( $H \rightarrow WW$ ): 1.5%.

2123 • *Normalization uncertainties*: 2% for Drell-Yan, 4% for embedded, 20% pre-fit  
2124 for the QCD multijet background in the  $e\mu$  channel, 20% pre-fit for the jet  
2125 faking background.

2126 The  $t\bar{t}$  process has additional acceptance uncertainties from QCD scale variation  
2127 and parton shower uncertainties [99]. Parton shower uncertainties originate from  
2128 the modeling of perturbative and non-perturbative QCD effects handled in parton  
2129 shower MC generators. The scale variations are determined from the envelope of the  
2130 6 provided shapes due to variations in the factorization scale, renormalization scale,  
2131 and their combined variation [99].

2132 The Z  $p_T$  reweighing uncertainty in Drell-Yan samples is taken to be 10% of the  
2133 nominal value, taken as a shape uncertainty.

2134 The fake rate uncertainties are taken as shape uncertainties. For the weight ap-  
2135 plied to scale up anti-isolated events in cross-trigger regions, 20% of the nominal  
2136 weight is taken as a shape uncertainty.

## 2137 8.7 Other uncertainties

2138 A 3.6% yield uncertainty in the signal is used to cover uncertainties in the parton  
2139 distribution functions,  $\alpha_s$  (fine structure constant), and QCD scale.

2140 Normalization uncertainties from luminosity are applied to all MC samples, di-  
2141 vided into those uncorrelated across years, those correlated between 2017 and 2018,  
2142 and one for 2018 [86].

## <sup>2143</sup> 8.8 Pulls and impacts

<sup>2144</sup> The top impacts and pulls computed for the combination of all channels and years is  
<sup>2145</sup> shown in Fig. 8.1. The top impacts are related to uncertainty in the signal sample and  
<sup>2146</sup> cross-section of the  $t\bar{t}$  cross-section, and also the yields of the jet faking  $\tau_h$  background,  
<sup>2147</sup> which is a major background in all channels and expected to be constrained due to  
<sup>2148</sup> the yield uncertainty which is taken to be 20% pre-fit.

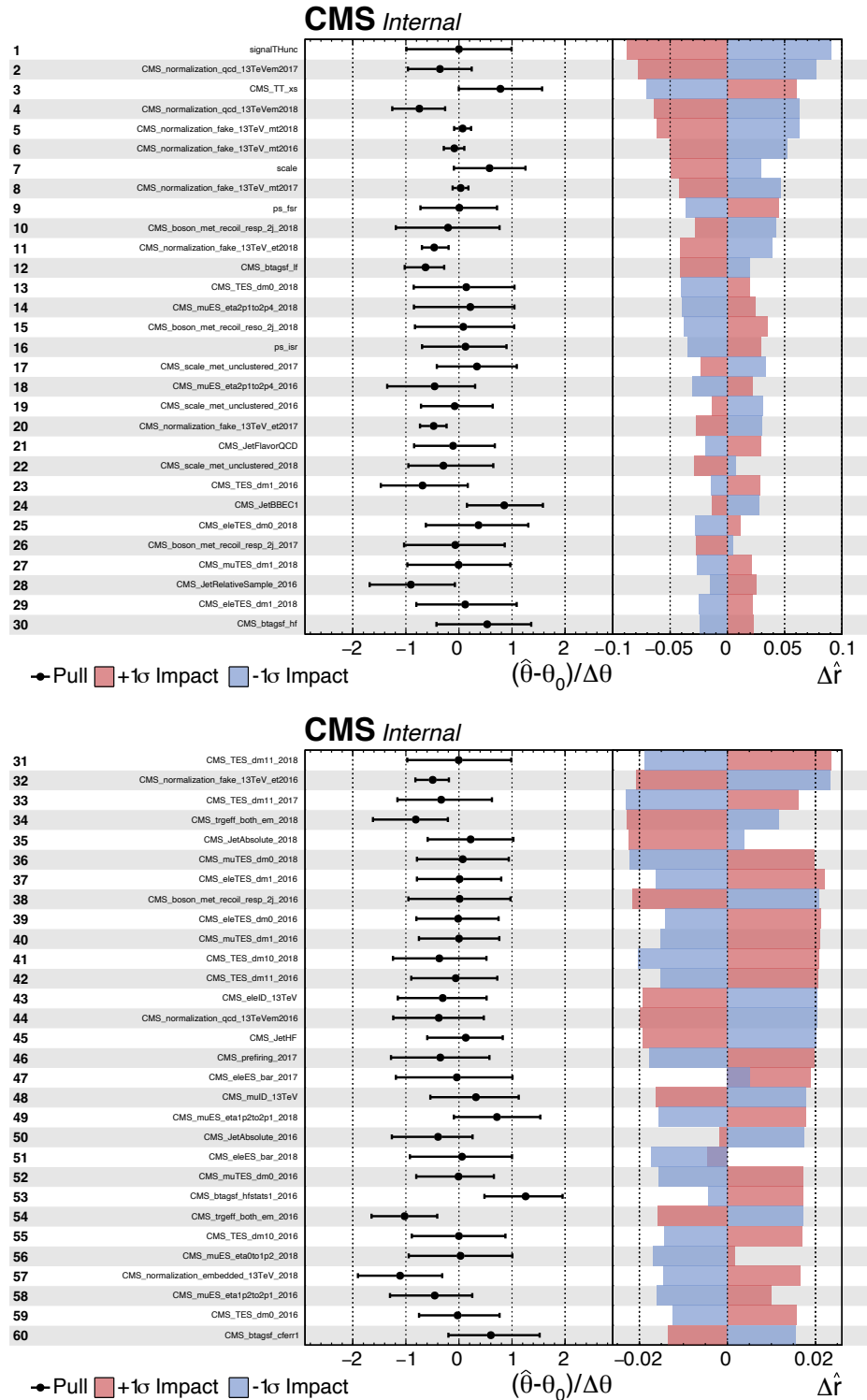


Figure 8.1: Top sixty pulls and impacts for the combination of all channels and years [45].

2149 **Chapter 9**

2150 **Event categorization and signal  
extraction**  
2151

2152 Measured events are divided into categories, based on cuts on values of observables  
2153 in the event, or some derived quantity based on the observables in the event. The  
2154 objective of event categorization is to divide events into signal regions, where the  
2155 signal is enhanced and the background is suppressed, and control regions, which are  
2156 signal-poor and used to check that the background estimation methods employed in  
2157 the analysis in fact accurately models the data. In this analysis, events in each tau-tau  
2158 channel are selected to contain one or more b-tag jets reconstructed in the event as  
2159 described in Section 9.1. Events are further divided into signal and control regions  
2160 using a deep learning-based approach described in Section 9.2. The signal is extracted  
2161 from the di-tau mass distribution in the signal region using the statistical procedure  
2162 described in Section 9.3.

2163 **9.1 B-tag jet multiplicity**

2164 The increased statistics of the full Run-2 dataset enables the separation of events into  
2165 events with exactly 1 b-tag jet and events with greater than 1 b-tag jet. Further event

2166 categorization is performed with deep neural networks (DNNs) described below. The  
2167 DNNs are used only for separating events into signal and control regions in the 1  
2168 b-tag and 2 b-tag jets scenarios. The final results are extracted from the statistical  
2169 fitting to the mass of the  $\tau\tau$ ,  $m_{\tau\tau}$ .

## 2170 9.2 DNN-based event categorization

2171 Neural networks for event categorization are trained for each of the  $\mu\tau_h$ ,  $e\tau_h$ , and  $e\mu$   
2172 channels, for 1 and 2 b-tag jets, giving  $3 \times 2 = 6$  networks in total. In the training,  
2173 the signal is taken to be all of the possible pseudoscalar mass  $m_a$  hypotheses together.  
2174 The backgrounds for each DNN are taken to be a representative combination of the  
2175 three major backgrounds:  $Z \rightarrow \tau\tau$ ,  $t\bar{t} + \text{jets}$ , and fake backgrounds. The proportions of  
2176 each background for each channel and b-tag jet multiplicity are taken from the yields  
2177 in the  $m_{\tau\tau}$  distribution. For instance, in the  $\mu\tau_h$  1 b-tag jet category, the composition  
2178 of the background for training is 17.4% from  $Z \rightarrow \tau\tau$ , 42.4% from  $t\bar{t} + \text{jets}$ , and 40.2%  
2179 fakes.

2180 The input variables capture the key differences between the signal and the back-  
2181 ground:

- 2182 • Transverse momentum  $p_T$  of the electron and muon in the  $e\tau_h$  and  $\mu\tau_h$  channels,  
2183 where the signal tends to have a softer  $p_T$  spectrum (lower energy) than the  
2184 background.
- 2185 •  $p_T$  of the b-tag jet(s). The signal sample b-tag jet(s) tend to have softer  $p_T$ .
- 2186 • Invariant masses of the various objects ( $\tau\tau$  legs and the b-tag jet(s)), which  
2187 tend to be smaller for the signal samples.
- 2188 • The angular separation  $\Delta R$  between pairs of the objects, where signal samples  
2189 peak at smaller  $\Delta R$  values.

- 2190 • The transverse mass between the missing transverse energy  $p_T^{\text{miss}}$  and each of  
 2191 the four objects [85], defined as

$$m_T(\ell, p_T^{\text{miss}}) \equiv \sqrt{2p_T^\ell \cdot p_T^{\text{miss}}[1 - \cos(\Delta\phi)]} \quad (9.1)$$

2192 where  $p_T^\ell$  is the transverse momentum of the object  $\ell$ , and  $\Delta\phi$  is the difference  
 2193 in azimuthal angle between the object and the  $p_T^{\text{miss}}$ . Events from  $t\bar{t}$ +jets and  
 2194 jets faking  $\tau_h$  backgrounds have larger  $p_T^{\text{miss}}$  resulting in larger transverse mass  
 2195 values compared to the signal, which tends to have smaller  $p_T^{\text{miss}}$  that is also  
 2196 more aligned with the lepton legs.

- 2197 • The variable  $D_\zeta$  [85], defined as

$$D_\zeta \equiv p_\zeta - 0.85p_\zeta^{\text{vis}} \quad (9.2)$$

2198 where the  $\zeta$  axis is the bisector of the transverse directions of the visible  $\tau$  decay  
 2199 products.  $p_\zeta$  is the component of the  $p_T^{\text{miss}}$  along the  $\zeta$  axis, and  $p_\zeta^{\text{vis}}$  is the sum  
 2200 of the components of the lepton  $p_T$  along the same axis. This variable captures  
 2201 the fact that in signal the  $p_T^{\text{miss}}$  is small and approximately aligned with the  $\tau\tau$ .  
 2202 In contrast, the  $Z \rightarrow \tau\tau$  background tends towards large  $D_\zeta$  values because the  
 2203  $p_T^{\text{miss}}$  is collinear to the  $\tau\tau$ , and the  $t\bar{t}$ +jets events tend to have small  $D_\zeta$  due to  
 2204 a large  $p_T^{\text{miss}}$  not aligned with the  $\tau\tau$ .

- 2205 • For events with 2 b-tag jets, one additional variable is defined to capture the  
 2206 difference in the invariant mass of the  $bb$  and the  $\tau\tau$ :

$$\Delta m_{a_1} \equiv (m_{bb} - m_{\tau\tau})/m_{\tau\tau} \quad (9.3)$$

2207 This variable peaks at zero for the  $h \rightarrow aa \rightarrow 2b2\tau$  signal.

After training, events in data, MC, and embedded are evaluated with the six DNNs and assigned a raw score between 0 and 1 (background-like or signal-like). In order to flatten the distribution of the score and define score thresholds for categorizing events, the raw output scores are transformed with the function  $\tilde{p}(n) = \text{arctanh}(p \times \tanh(n))/n$  where  $n$  is a positive integer. The thresholds of the DNN score used for signal/control region definition are determined using scans that optimize the signal sensitivity and are shown in Tables 9.1 and 9.2.

1bNN $\tilde{p}(n = 1.5)$				
	SR1	SR2	SR3	CR
$\mu\tau_h$ 2018	$> 0.98$	$\in [0.95, 0.98]$	$\in [0.90, 0.95]$	$< 0.90$
$\mu\tau_h$ 2017	$> 0.97$	$\in [0.94, 0.97]$	$\in [0.90, 0.94]$	$< 0.90$
$\mu\tau_h$ 2016	$> 0.97$	$\in [0.94, 0.97]$	$\in [0.89, 0.94]$	$< 0.89$
1bNN $\tilde{p}(n = 1.5)$				
	SR1	SR2	SR3	CR
$e\tau_h$ 2018	$> 0.97$	$\in [0.945, 0.97]$	$\in [0.90, 0.945]$	$< 0.90$
$e\tau_h$ 2017	$> 0.985$	$\in [0.965, 0.985]$	$\in [0.93, 0.965]$	$< 0.93$
$e\tau_h$ 2016	$> 0.985$	$\in [0.965, 0.985]$	$\in [0.93, 0.965]$	$< 0.93$
1bNN $\tilde{p}(n = 2.5)$				
	SR1	SR2	SR3	CR
$e\mu$ 2018	$> 0.99$	$\in [0.95, 0.99]$	$\in [0.85, 0.95]$	$< 0.85$
$e\mu$ 2017	$> 0.985$	$\in [0.95, 0.985]$	$\in [0.85, 0.95]$	$< 0.85$
$e\mu$ 2016	$> 0.99$	$\in [0.95, 0.99]$	$\in [0.85, 0.95]$	$< 0.85$

Table 9.1: Event categorization based on DNN scores for events with exactly 1 b-tag jet (1bNN), for the three  $\tau\tau$  channels and three eras.

### 9.3 Methodology for signal extraction

After events are divided into categories, the data is compared to the expected backgrounds in the signal region categories. Here, we describe the fundamental concepts behind hypothesis testing in high-energy physics, as well as how exclusion limits can be set on parameters whose true values we cannot measure, culminating in the modified frequentist method  $CL_S$  which is used to perform signal extraction in this

	2bNN $\tilde{p}(n = 1.5)$		
	SR1	SR2	CR
$\mu\tau_h$ 2018	> 0.99	$\in [0.96, 0.99]$	< 0.96
$\mu\tau_h$ 2017	> 0.98	$\in [0.94, 0.98]$	< 0.94
$\mu\tau_h$ 2016	> 0.97	$\in [0.93, 0.97]$	< 0.93
	2bNN $\tilde{p}(n = 1.5)$		
	SR1	SR2	CR
$e\tau_h$ 2018	> 0.96	NA	< 0.96
$e\tau_h$ 2017	> 0.985	NA	< 0.985
$e\tau_h$ 2016	> 0.96	NA	< 0.96
	2bNN $\tilde{p}(n = 2.5)$		
	SR1	SR2	CR
$e\mu$ 2018	> 0.98	$\in [0.94, 0.98]$	< 0.94
$e\mu$ 2017	> 0.97	$\in [0.93, 0.97]$	< 0.93
$e\mu$ 2016	> 0.98	$\in [0.94, 0.98]$	< 0.94

Table 9.2: Event categorization based on DNN scores for events with 2 b-tag jets (2bNN), for the three  $\tau\tau$  channels and three eras.

2221 analysis.

### 2222 9.3.1 Model building and parameter estimation

In the frequentist interpretation of probability, an experiment measuring an observable can be repeated, resulting in different values of the observable, e.g. the invariant mass of a candidate Higgs boson in a search for the Higgs [100]. The ensemble of values of the observable  $x$  gives rise to the probability density function (PDF)  $f(x)$ , which has the important property that it is normalized to unity:

$$\int f(x) dx = 1.$$

A parametric family of PDFs

$$f(x|\alpha),$$

2223 read “ $f$  of  $x$  given  $\alpha$ ”, is referred to as a probability model or model. The parameters  $\alpha$   
 2224 typically represent parameters of the theory or an unknown property of the detector’s  
 2225 response. The parameters are not frequentist in nature, unlike  $x$ . Out of all the  
 2226 parameters, typically only a few are of interest, and are called the parameters of  
 2227 interest (POI), labeled  $\mu$  here. The remaining are referred to as nuisance parameters  
 2228 (NP) [100] and are labeled  $\theta$ .

2229  $f(x)$  is the probability density for the observable in one event and we wish to  
 2230 describe the probability density for a dataset with many events,  $\mathcal{D} = \{x_1, \dots, x_n\}$ ,  
 2231 called the total probability model  $\mathbf{f}$ . For instance, if we also have a prediction for  
 2232 the total number of events expected, called  $\nu$ , we also account for the overall Poisson  
 2233 probability for observing  $n$  events given  $\nu$  expected:

$$\mathbf{f}(\mathcal{D}|\nu, \alpha) = \text{Poisson}(n|\nu) \prod_{e=1}^n f(x_e|\alpha) \quad (9.4)$$

The likelihood function  $L(\alpha)$  is numerically equivalent to  $f(x|\alpha)$  for fixed  $x$ , or  
 $\mathbf{f}(\mathcal{D}|\alpha)$  with  $\mathcal{D}$  fixed [100]. The likelihood function is not a probability density for  $\alpha$   
 and is not normalized to unity:

$$\int L(\alpha) d(\alpha) \neq 1.$$

2234 i.e. the likelihood function is the value of  $f$  as a function of  $\alpha$  given a fixed value of  
 2235  $x$ .

2236 To estimate the parameter  $\alpha$  we use an estimator, which is a function of the  
 2237 data. Take for example the measurement of data distributed according to a Gaussian  
 2238 probability density  $f(x|\mu, \sigma) = \text{Gauss}(x|\mu, \sigma)$ . One possible estimator of the mean  $\mu$ ,  
 2239 is the mean of the measured data points  $\bar{x} = \sum_{i=1}^n x_i/n$  [100].

2240 A commonly used estimator in physics is the maximum likelihood estimator  
 2241 (MLE), defined as the value  $\alpha$  which maximizes the likelihood function  $L(\alpha)$ . This

2242 value, labeled  $\hat{\alpha}$ , also maximizes  $\ln L(\alpha)$  and minimizes  $-\ln L(\alpha)$ . By convention the  
2243  $-\ln L(\alpha)$  is minimized, in a process called “fitting”, and the maximum likelihood  
2244 estimate is called the “best fit value”.

2245 **9.3.2 Hypothesis testing**

2246 In this section we next introduce concepts related to hypothesis testing such as the  
2247 test statistic constructed from the ratio of likelihood functions.

2248 The objective of a likelihood analysis is to distinguish different models repre-  
2249 senting the various hypotheses, and determine the one that best explains the ex-  
2250 perimental outcome. In a search for new physics, a signal is additive on top of the  
2251 background. The background-only hypothesis is the null hypothesis, and the signal-  
2252 plus-background hypothesis is the alternative.

2253 As a simple example, take the  $p$ -value test, for an experiment where we count  
2254 events in the signal region,  $n_{SR}$ , and expect  $\nu_B$  background events and  $\nu_S$  events from  
2255 the signal [100]. Then

2256 1. The null hypothesis ( $H_0$ ), i.e. the background-only hypothesis in this experi-  
2257 ment, with the probability modeled by  $\text{Poisson}(n_{SR}|\nu_B)$ .

2258 2. The alternate hypothesis ( $H_1$ ), i.e. signal-plus-background hypothesis, with the  
2259 probability modeled by  $\text{Poisson}(n_{SR}|(\nu_B + \nu_S))$ .

2260 The compatibility of the observed data  $\nu_{SR}^0$  and the null hypothesis, is quantified as  
2261 the probability that the background-only hypothesis would produce at least as many  
2262 events as was observed. This probability is the  $p$ -value:

$$p = \sum_{n=n_{SR}^0}^{\infty} \text{Poisson}(n|\nu_B). \quad (9.5)$$

2263 If the  $p$ -value is very small, we might reject the null hypothesis. The  $p$ -value is not the

2264 probability of the null hypothesis given the data; rather, it expresses the probability  
2265 that data with a certain property was obtained, assuming the null hypothesis [100].

2266 The  $p$ -value is an example of a test statistic  $T$ , which maps the data to a single  
2267 real number. The Neyman-Pearson lemma states that out of the infinite possibilities  
2268 of choices of test statistic, the uniformly most powerful test statistic is the likelihood  
2269 ratio  $T_{NP}$  [100]:

$$T_{NP}(\mathcal{D}) = \frac{L(\mathcal{D}|H_1)}{L(\mathcal{D}|H_0)} \quad (9.6)$$

To reiterate, the test statistic  $T$  is a real-valued function of the data, implying that a particular probability model  $\mathbf{f}(\mathcal{D}|\boldsymbol{\alpha})$  implies a distribution of the test statistic,  $f(T|\boldsymbol{\alpha})$ , which depends on the value of  $\boldsymbol{\alpha}$ . With this distribution in hand, the  $p$ -value can be evaluated in the following equivalent formulations:

$$p(\boldsymbol{\alpha}) = \int_{T_0}^{\infty} f(T|\boldsymbol{\alpha}) dT \quad (9.7)$$

$$= \int \mathbf{f}(\mathcal{D}|\boldsymbol{\alpha}) \theta(T(\mathcal{D}) - T_0) d\mathcal{D} \quad (9.8)$$

$$= P(T \geq T_0|\boldsymbol{\alpha}) \quad (9.9)$$

2270 where  $T_0$  is the value of  $T$  based on the observed data, and  $\theta()$  is the Heaviside  
2271 function. The size of the test is conventionally chosen to be 10%, 5%, or 1%. As  
2272 the  $p$ -value depends on  $\boldsymbol{\alpha}$  (both the POI and NP), the null hypothesis should not be  
2273 rejected if the  $p$ -value is larger than the size of the test for any value of the nuisance  
2274 parameters.

### 2275 9.3.3 Confidence intervals

2276 In an example of the measurement of the Standard Model Higgs boson,  $\boldsymbol{\alpha}_{POI} =$   
2277  $(\sigma/\sigma_{SM}, M_H)$ , with  $\sigma/\sigma_{SM}$  is the ratio of the production cross-section for Higgs with

respect to its value in the SM, and  $M_H$  is the unknown mass of the Higgs, values  
 of these parameters outside specific bounds are said to be “excluded at the 95%  
 confidence level”. These allowed regions are called confidence levels or confidence  
 regions, and the parameter values outside of them are considered excluded [100]. A  
 95% confidence interval does not mean that there is a 95% chance that the true value  
 of the parameter is inside the interval. Rather, a 95% confidence interval covers the  
 true value 95% of the time (even though we do not know the true value).

To construct a confidence interval for a parameter  $\alpha$ , the Neyman Construction  
 is used to invert a series of hypothesis tests; i.e. for each possible value of  $\alpha$ , the null  
 hypothesis is treated as  $\alpha$ , and we perform a hypothesis test based on a test statistic.  
 To construct a 95% confidence interval, we construct a series of hypothesis tests with  
 size of 5%. The confidence interval  $I(\mathcal{D})$  is constructed by taking the set of parameter  
 values  $\boldsymbol{\alpha}$  where the null hypothesis is accepted:

$$I(\mathcal{D}) = \{\boldsymbol{\alpha} | P(T(\mathcal{D}) > k_\alpha | \boldsymbol{\alpha}) < \alpha\}, \quad (9.10)$$

where  $T(\mathcal{D})$  is the test statistic, and the last  $\alpha$  (not bolded) and the subscript  $k_\alpha$   
 refer to the size of the test. A schematic of the Neyman construction is shown in Fig.  
 9.1. In a more generalized case, the  $x$ -axis is the test statistic  $T$ .

### 9.3.4 Profile likelihood ratio

In this section we describe a frequentist statistical procedure based on the profile  
 likelihood ratio test statistic, which is implemented using asymptotic distributions.

With a multi-parameter likelihood function  $L(\boldsymbol{\alpha})$ , the the maximum likelihood of  
 one specific parameter  $\alpha_p$  with other parameters  $\boldsymbol{\alpha}_o$  fixed, is called the conditional  
 maximum likelihood estimate and is denoted  $\hat{\alpha}_p(\boldsymbol{\alpha}_0)$ . The process of choosing specific  
 values of the nuisance parameters for a given value of  $\mu$ ,  $\mathcal{D}_{\text{simulated}}$ , and value of global

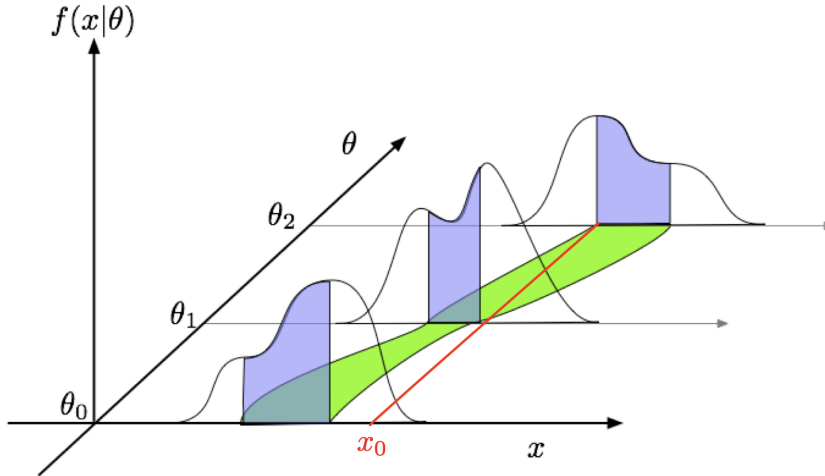


Figure 9.1: Schematic of the Neyman construction for confidence intervals [100]. For each value of  $\theta$ , we find a region in  $x$  where  $\int f(x|\theta)dx$  satisfies the size of the test (blue). These regions form a confidence belt (green). The intersection of the observation  $x_0$  (red) with the confidence belt defines the confidence interval  $[\theta_1, \theta_2]$  [100].

2301 observables  $\mathcal{G}$  is called profiling. From the full list of parameters  $\boldsymbol{\alpha}$ , we denote the  
2302 parameter of interest  $\mu$ , and the nuisance parameters  $\boldsymbol{\theta}$ .

2303 We construct the profile likelihood ratio,

$$\lambda(\mu) = \frac{L(\mu, \hat{\boldsymbol{\theta}}(\mu))}{L(\mu, \hat{\boldsymbol{\theta}})} \quad (9.11)$$

2304 which depends explicitly on the parameter of interest  $\mu$ , implicitly on the data  $\mathcal{D}_{\text{sim}}$   
2305 and global observables  $\mathcal{G}$ , and is independent of the nuisance parameters  $\boldsymbol{\theta}$ , which  
2306 have been eliminated in profiling [100].

2307 The main conceptual reason for constructing the test statistic from the profile  
2308 likelihood ratio is that asymptotically (i.e. for measurements with many events) the  
2309 distribution of the profile likelihood ratio  $\lambda(\mu = \mu_{\text{true}})$  is independent of the values of  
2310 the nuisance parameters [100].

2311 The following  $p$ -value is used to quantify the consistency with the hypothesis of a  
2312 signal strength of  $\mu$ :

$$p_\mu = \int_{\tilde{q}_{\mu,\text{obs}}}^{\infty} f(\tilde{q}_\mu | \mu, \hat{\boldsymbol{\theta}}(\mu, \text{obs})) d\tilde{q}_\mu \quad (9.12)$$

2313 **9.3.5 Modified frequentist method:  $CL_S$**

2314 In the modified frequentist method called  $CL_S$ , to test a hypothesis with signal, we  
2315 define  $p'_\mu$  as a ratio of  $p$ -values [100]:

$$p'_\mu = \frac{p_\mu}{1 - p_b} \quad (9.13)$$

2316 where  $p_b$  is the  $p$ -value derived under the background-only hypothesis:

$$p_b = 1 - p_0 \equiv 1 - \int_{\tilde{q}_{\mu,\text{obs}}}^{\infty} f(\tilde{q}_\mu | 0, \hat{\theta}(\mu = 0, \text{obs})) d\tilde{q}_\mu. \quad (9.14)$$

2317 The  $CL_S$  upper limit on  $\mu$ , denoted  $\mu_{up}$ , is obtained by solving for  $p'_{\mu_{up}} = 5\%$ .  
2318 If testing the compatibility of the data with the background-only hypothesis, we  
2319 consider the  $p_b$  value defined above and conventionally convert it into the quantile  
2320 or “sigma” of a unit Gaussian.  $z$  standard deviations (e.g.  $z = 5$  in “ $5\sigma$ ”) means  
2321 that the probability of falling above these standard deviations, equals  $p_b$  (e.g.  $3\sigma$   
2322 corresponds to  $p_b = 2.7 \times 10^{-3}$  or 95.43%, and  $5\sigma$  corresponds to  $p_b = 5.7 \times 10^{-7}$  or  
2323 99.999943%).

2324 **Chapter 10**

2325 **Results**

2326 In this chapter, Section 10.1 presents the results from the  $h \rightarrow aa \rightarrow bb\tau\tau$  analysis  
2327 performed on  $137 \text{ fb}^{-1}$  of data from the full CMS Run-2 dataset in the years 2016 to  
2328 2018, with interpretations provided for different 2HDM+S scenarios. This analysis  
2329 was combined with a different search in the  $h \rightarrow aa \rightarrow bb\mu\mu$  final state, which was  
2330 also performed on the full Run-2 dataset. The combination procedure and results  
2331 from the combined analyses ( $h \rightarrow aa \rightarrow bb\ell\ell$ , with  $\ell = \mu, \tau$ ) are detailed in 10.2.  
2332 The combined analysis places some of the most stringent limits to date at CMS for  
2333 2HDM+S scenarios in the light scalar mass range  $m_a = 12 \text{ GeV}$  to  $60 \text{ GeV}$ .

2334 **10.1 Results from  $bb\tau\tau$**

2335 In each of the three  $\tau\tau$  channels studied ( $\mu\tau_h$ ,  $e\tau_h$ , and  $e\mu$ ), events are divided based  
2336 on whether they contain exactly 1 or 2 b-tag jets, and further divided into signal  
2337 and control regions (SRs and CRs) using the DNN categorization score as described  
2338 in Section 9.2. The control regions demonstrate good agreement between observed  
2339 events in data, and the sum of the contributions from expected backgrounds that  
2340 are modeled in simulated and embedded samples. The signal regions are defined to  
2341 be sensitive to the  $h \rightarrow aa \rightarrow bb\tau\tau$  signal. The postfit final observed and expected

2342 distributions of the di-tau invariant mass  $m_{\tau\tau}$  reconstructed with SVFit (described  
2343 in Section 5.2) are shown in Fig. 10.1 for the  $\mu\tau_h$  channel, Fig. 10.2 for the  $e\tau_h$   
2344 channel, and Fig. 10.3 for the  $e\mu$  channel. In all figures, the hypothesized yield for  
2345 the  $h \rightarrow aa \rightarrow bb\tau\tau$  signal is shown for the pseudoscalar mass  $m_a = 35$  GeV and  
2346 assuming a branching fraction  $B(H \rightarrow aa \rightarrow bb\tau\tau) = 10\%$ .

2347 The 95% CL expected and observed exclusion limits on the signal strength of the  
2348 branching fraction  $B(h \rightarrow aa \rightarrow bb\tau\tau)$  as a function of the pseudoscalar mass  $m_a$   
2349 ranging from 12 GeV to 60 GeV, are shown for the three  $\tau\tau$  channels and all three  
2350 channels combined in Fig. 10.4. The limits are shown as percentages and normalized  
2351 to the production cross-section of the Standard Model Higgs boson. No excess of  
2352 events above the Standard Model expectations is observed. In the limits for the three  
2353  $\tau\tau$  channels combined, expected (observed) limits range from 1.4 to 5.6% (1.7 to  
2354 7.6%) for pseudoscalar masses between 12 and 60 GeV.

2355 The  $e\mu$  channel is the only channel that has signal sensitivity to the  $m_a = 12$   
2356 GeV pseudoscalar mass hypothesis, because the minimum required spatial separation  
2357  $\Delta R = \sqrt{(\Delta\eta)^2 + (\Delta\phi)^2}$  between the two  $\tau$  legs is smaller than the other two channels  
2358 ( $\Delta R < 0.3$  for  $e\mu$ , compared to  $\Delta R < 0.4$  for the other two channels). This decreased  
2359  $\Delta R$  requirement results in better signal acceptance for low mass signals for the  $e\mu$   
2360 channel. The  $\mu\tau_h$  and  $e\tau_h$  channels are most sensitive to the intermediate mass points  
2361 studied, since the analysis targets a resolved signature: at low mass points, the tau  
2362 legs are boosted, and at high mass points, the  $m_{\tau\tau}$  distributions in signal have larger  
2363 overlap with background distributions. In the combination of the three  $\tau\tau$  channels,  
2364 the limit for  $m_a = 12$  GeV comes only from the  $e\mu$  channel, and the best sensitivity  
2365 is attained at intermediate mass points around  $m_a = 20$  GeV to 45 GeV.

2366 To set limits on the branching fraction of the 125 GeV Higgs to the two pseu-  
2367 doscalars,  $B(h \rightarrow aa)$ , we interpret the results in four types of 2HDM+S, which were  
2368 introduced in Section 1.4. In 2HDM+S, the theorized branching fraction of the pseu-

2369 doscalars depends on the 2HDM+S model type, the pseudoscalar mass  $m_a$ , and the  
2370 ratio of the two Higgs doublets' vacuum expectation values  $\tan \beta$ . In Type I models,  
2371 the branching fraction is independent of  $\tan \beta$ , while in Types II, III, and IV, it is  
2372 a function of  $m_a$  and  $\tan \beta$ . Limits for the  $bb\tau\tau$  final state as a function of  $m_a$  for  
2373 2HDM+S Type I (valid for all  $\tan \beta$  values), Type II with  $\tan \beta = 2.0$ , Type III with  
2374  $\tan \beta = 2.0$ , and Type IV with  $\tan \beta = 0.6$  are overlaid and shown in Fig. 10.5a.

## 2375 **10.2 Combination with $bb\mu\mu$ final state**

2376 Results from this analysis for the  $h \rightarrow aa \rightarrow bb\tau\tau$  final state are combined with the  
2377 analysis for the  $h \rightarrow aa \rightarrow bb\mu\mu$  final state [101]. While the predicted branching ratio  
2378 for  $aa \rightarrow bb\mu\mu$  is comparatively small, the  $bb\mu\mu$  final state has competitive results  
2379 due to the excellent di-muon resolution measured by CMS. The  $bb\mu\mu$  analysis uses  
2380 an unbinned fit to the data using the di-muon mass  $m_{\mu\mu}$  distribution. Details can be  
2381 found in [101].

2382 Combining the results is possible since the  $bb\tau\tau$  analysis explicitly rejects events  
2383 with extra leptons, so there is no overlap between the events studied in the  $bb\tau\tau$   
2384 analysis and the  $bb\mu\mu$  analysis. In the statistical combination, several systematic  
2385 uncertainties are treated as correlated: the integrated luminosity normalization, the  
2386 b-tagging scale factor, the scale factors related to muon reconstruction, identifica-  
2387 tion, and trigger efficiencies, the inefficiency in the ECAL trigger readout, and the  
2388 theoretical uncertainties related to signal modeling.

2389 Since the results in both final states are statistically limited, the combination ben-  
2390 efits from the additional data. For  $m_a = 35$  GeV, all systematic uncertainties amount  
2391 to around 6% of the total uncertainty, with the dominant systematic uncertainties  
2392 coming from jet energy systematics in the  $bb\mu\mu$  final state, theoretical uncertainties  
2393 in the signal, and uncertainties in the QCD multijet backgrounds in the  $e\mu$  channel

2394 of the  $bb\tau\tau$  final state.

2395 The mass distributions of the di-muon and di-tau objects ( $m_{\mu\mu}$  and  $m_{\tau\tau}$ ) are  
2396 compared to the data in a combined maximum likelihood fit to derive upper limits  
2397 on  $B(h \rightarrow aa)$ . The observed limits at 95% CL on  $B(h \rightarrow aa)$  for different 2HDM+S  
2398 scenarios, are shown for the search for  $h \rightarrow aa \rightarrow bb\mu\mu$  in Fig. 10.5b, and the  
2399 combined analyses  $h \rightarrow aa \rightarrow bb\ell\ell$  in Fig. 10.6.

2400 Exclusion limits in a two-dimensional plane as a function of  $\tan\beta$  and  $m_a$  are  
2401 set for 2HDM+S Types II, III, and IV in Fig. 10.7. The most stringent constraints  
2402 are observed for 2HDM+S type III because of large branching fractions predicted in  
2403 theory, with predicted branching fractions between 0.47 and 0.42 for  $\tan\beta = 2.0$  and  
2404 values of  $m_a$  between 15 and 60 GeV, compared to the observed 95% CL upper limits  
2405 which are between 0.08 and 0.03. For 2HDM+S type IV, the predicted branching  
2406 fractions from theory are between 0.26 and 0.20 for  $\tan\beta = 0.6$  for values of  $m_a$   
2407 between 15 and 60 GeV, and the 95% CL observed upper limits are between 0.12 and  
2408 0.05.

2409 The combined results from  $h \rightarrow aa \rightarrow bb\ell\ell$  are compared with CMS results in  
2410 other final states as a function of the pseudoscalar mass  $m_a$ : for 2HDM+S type I in  
2411 Fig. 10.8, type II with  $\tan\beta = 2.0$  in Fig. 10.9, and type III with  $\tan\beta = 2.0$  in Fig.  
2412 10.10. In other scenarios, e.g. type III with  $\tan\beta = 5.0$ , more stringent limits are set  
2413 by analyses in other final states,  $\mu\mu\tau\tau$  in this case. Other summary plots for other  
2414 model types and  $\tan\beta$  values can be found at [102].

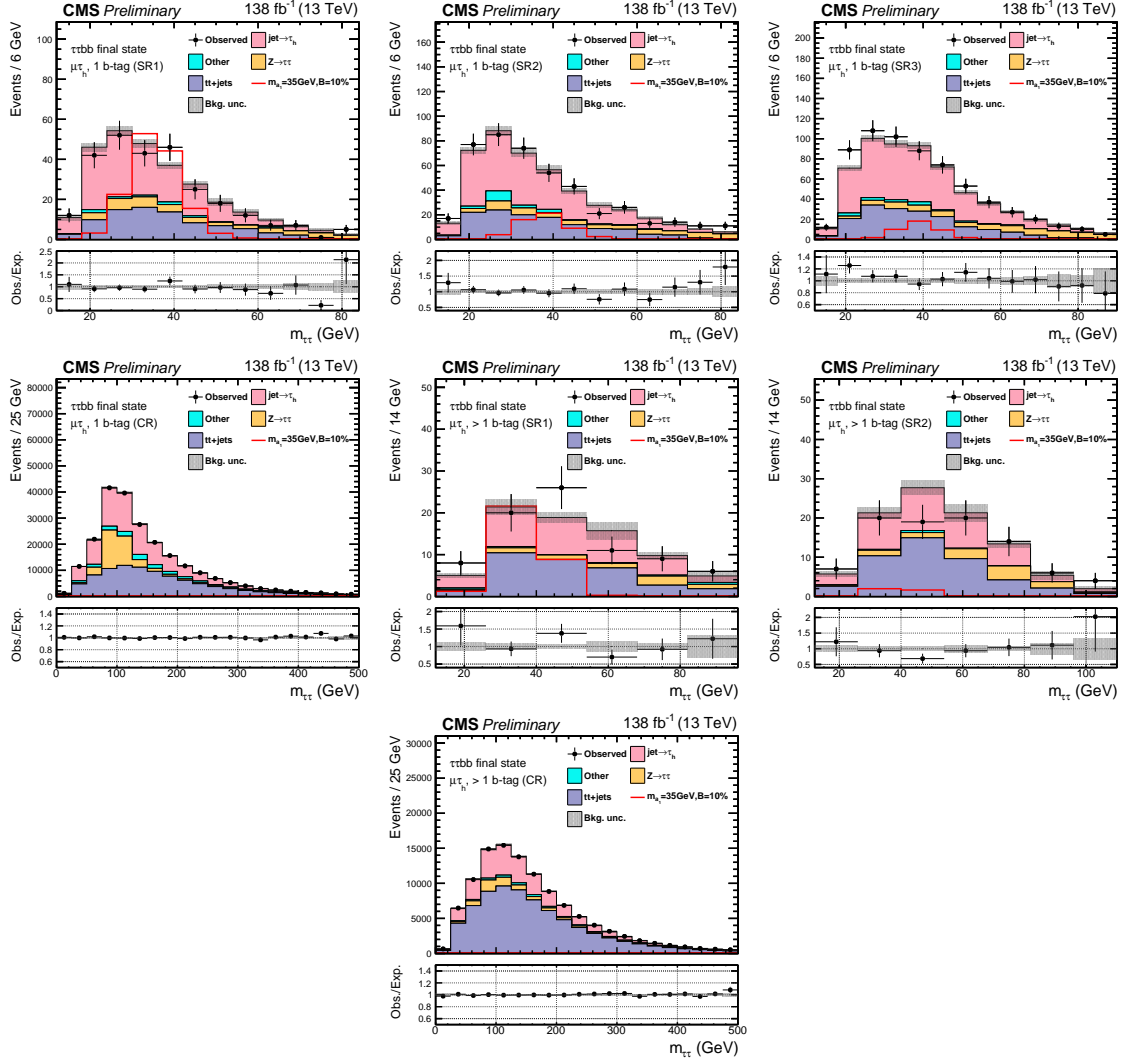


Figure 10.1: Postfit final  $m_{\tau\tau}$  observed and expected distributions, and the observed/expected ratios, in the  $\mu\tau_h$  channel [45]. Events are divided into the 1 b-tag jet signal regions (SR1, SR2, SR3) (*top row*), 1 b-tag jet control region (*middle row*), 2 b-tag jet signal regions (SR1, SR2) (*middle row*), and lastly the 2 b-tag jet control region (CR) (*bottom*). Statistical and systematic sources of uncertainties in the expected events are added in quadrature and labeled “Bkg. unc” (*shaded gray*). The dominant backgrounds in all categories are jets faking the  $\tau_h$  leg (*pink*),  $Z \rightarrow \tau\tau$  (*orange*), and  $t\bar{t}+j$ ets (*purple*). For illustrative purposes, the beyond-Standard Model signal yield from  $h \rightarrow aabb\tau\tau$  is shown for the pseudoscalar mass hypothesis  $m_a = 35$  GeV, assuming a branching fraction  $B(h \rightarrow aa \rightarrow bb\tau\tau) = 10\%$  (*red line*).

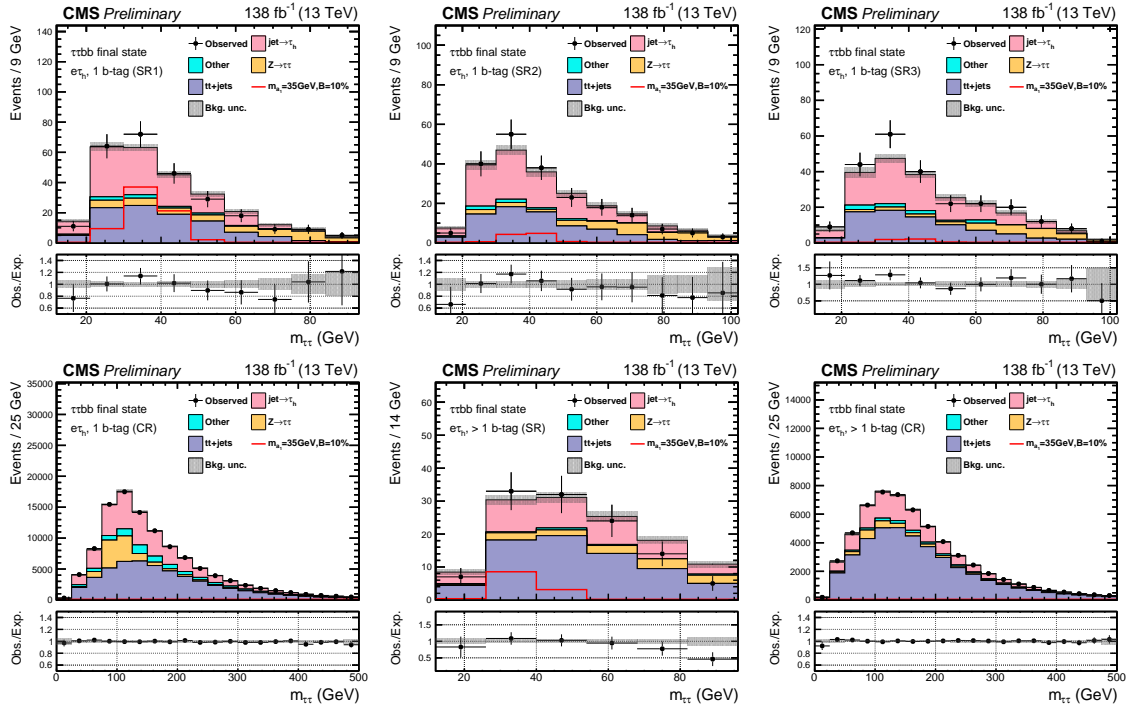


Figure 10.2: Postfit final observed and expected  $m_{\tau\tau}$  distributions, and the observed/expected ratios, in the  $e\tau_h$  channel [45]. Events are divided into the 1 b-tag jet signal regions (SR1, SR2, SR3) (*top row*), the 1 b-tag jet control region (CR) (*bottom row*), and 2 b-tag jet signal region (SR) and control region (CR) (*bottom row*). Statistical and systematic sources of uncertainties in the expected events are added in quadrature and labeled “Bkg. unc” (*shaded gray*). In this channel, the dominant backgrounds are jets faking the  $\tau_h$  leg (*pink*),  $Z \rightarrow \tau\tau$  (*orange*), and  $t\bar{t}+jets$  (*purple*). For illustrative purposes, the beyond-Standard Model signal yield from  $h \rightarrow aabb\tau\tau$  is shown for the pseudoscalar mass hypothesis  $m_a = 35$  GeV, assuming a branching fraction  $B(h \rightarrow aa \rightarrow bb\tau\tau) = 10\%$  (*red line*).

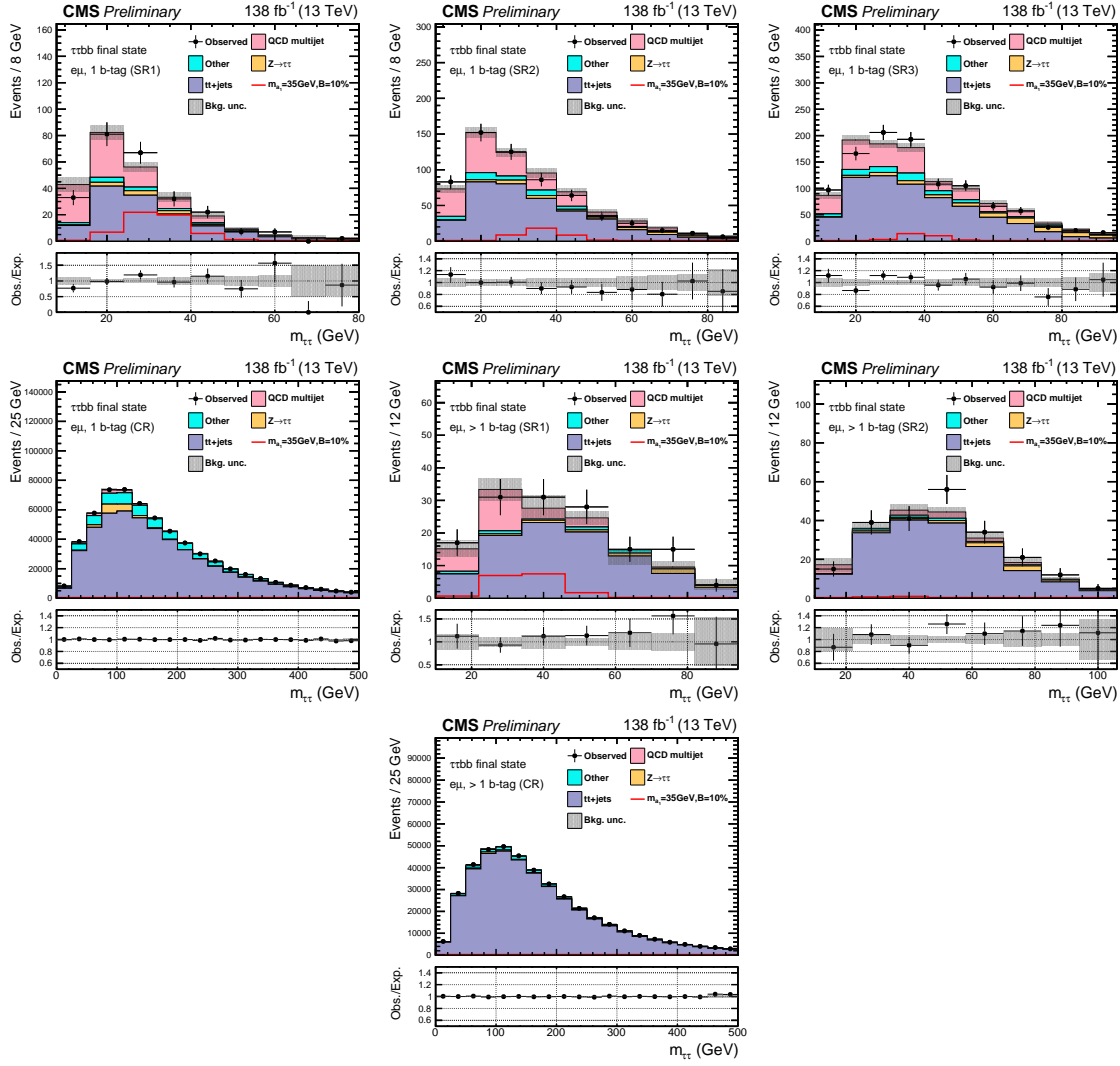


Figure 10.3: Postfit final observed and expected  $m_{\tau\tau}$  distributions, and the observed/expected ratios, in the  $e\mu$  channel [45]. Events are divided into the 1 b-tag jet signal regions (SR1, SR2, and SR3) (*top row*), 1 b-tag jet control region (CR) (*middle row*), 2 b-tag jet signal regions (SR1 and SR2) (*middle row*), and 2 b-tag jet control region (CR) (*bottom row*). Statistical and systematic sources of uncertainties in the expected events are added in quadrature and labeled “Bkg. unc” (*shaded gray*). The  $t\bar{t}+j$  process (*purple*) is a major background, and in the signal regions the QCD multijet (*pink*) is also a major background. TFor illustrative purposes, the beyond-Standard Model signal yield from  $h \rightarrow aabb\tau\tau$  is shown for the pseudoscalar mass hypothesis  $m_a = 35$  GeV, assuming a branching fraction  $B(h \rightarrow aa \rightarrow bb\tau\tau) = 10\%$  (*red line*).

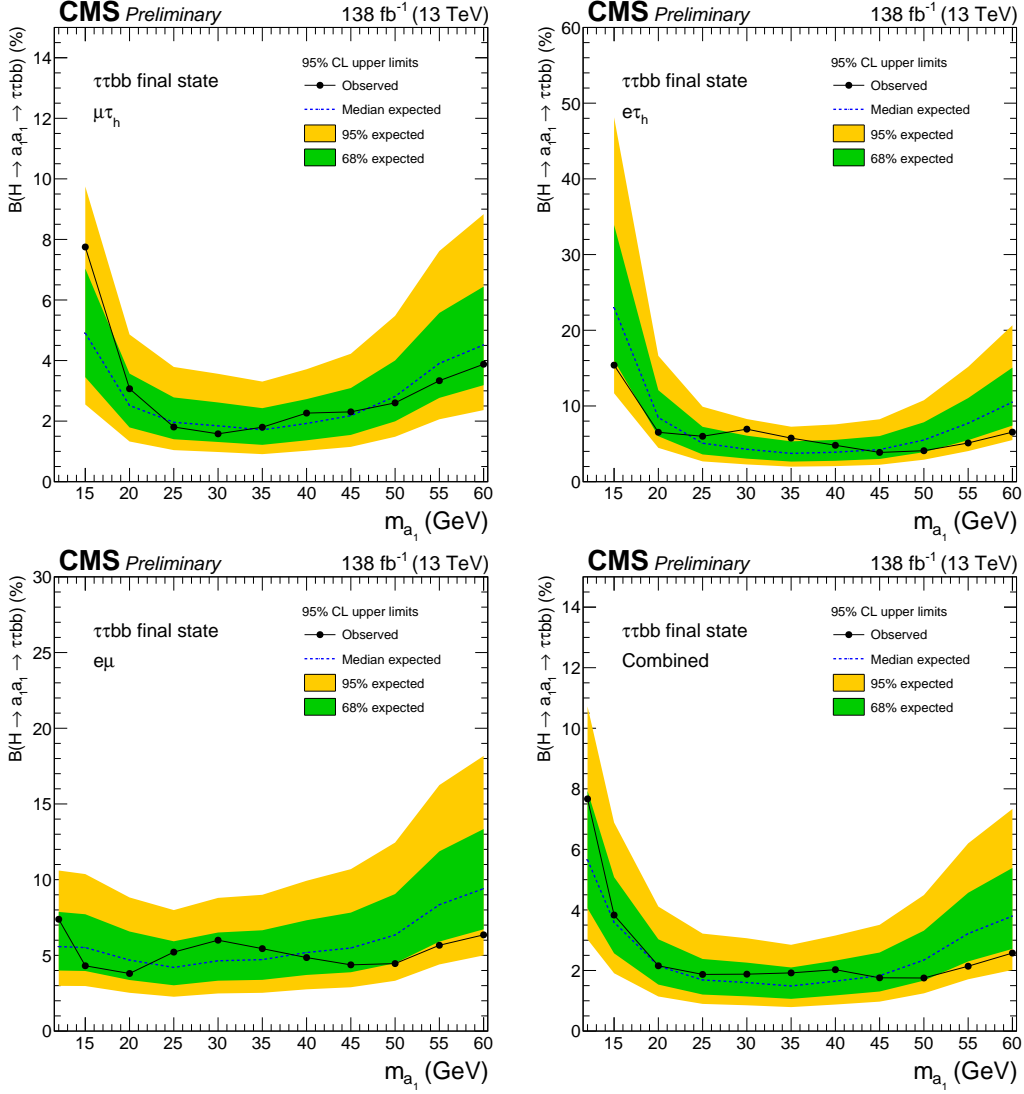
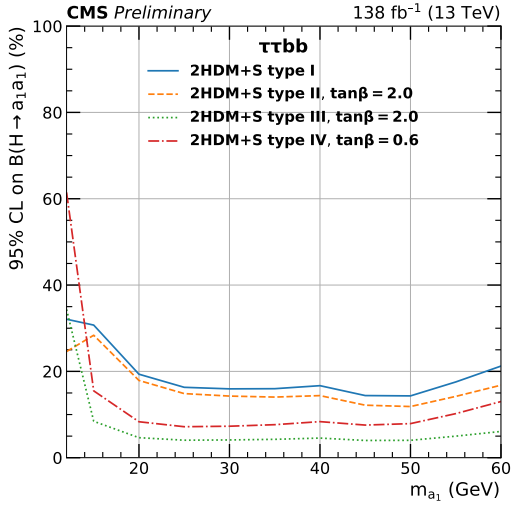
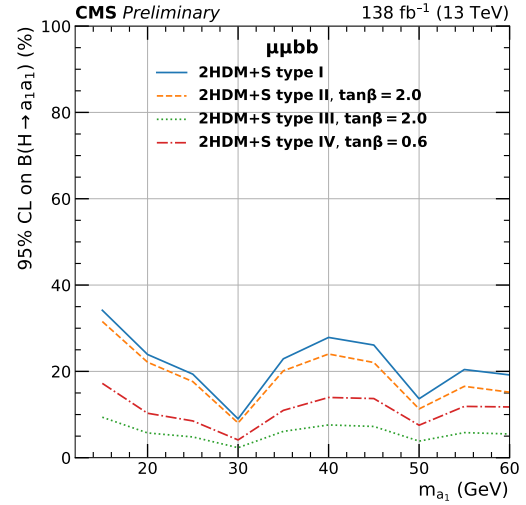


Figure 10.4: Observed 95% CL exclusion limits (*black, solid lines*) and expected 95% CL and 68% CL limits (*shaded yellow and green*) on the branching fraction  $B(h \rightarrow aa \rightarrow bb\tau\tau)$  in percentages, assuming the Standard Model production for the 125 GeV Higgs ( $h$ ). Limits are shown for the  $\mu\tau_h$  channel (*top left*), the  $e\tau_h$  channel (*top right*), and the  $e\mu$  channel (*bottom left*), and lastly the combination of all three channels (*bottom right*) [45]. The dataset corresponds to 138  $\text{fb}^{-1}$  of data collected in the years 2016-2018 at a center-of-mass energy 13 TeV. Only the  $e\mu$  channel has sensitivity to the mass hypothesis  $m_a = 12$  GeV. The best sensitivity is attained at intermediate mass points.



(a)  $bb\tau\tau$  final state.



(b)  $bb\mu\mu$  final state.

Figure 10.5: Observed 95% CL upper limits on  $B(h \rightarrow aa)$  in %, for the  $bb\tau\tau$  final state (*left*) and  $bb\mu\mu$  final state (*right*) using the full Run 2 integrated luminosity of  $138 \text{ fb}^{-1}$  in 2HDM+S type I (blue), type II with  $\tan\beta = 2.0$  (orange dashed), type III with  $\tan\beta = 2.0$  (dotted green), and type IV with  $\tan\beta = 0.6$  (red dashed) [45]. Linear interpolation is used between points in the graphs. The  $\tan\beta$  values chosen here correspond to the most stringent limits in each model.

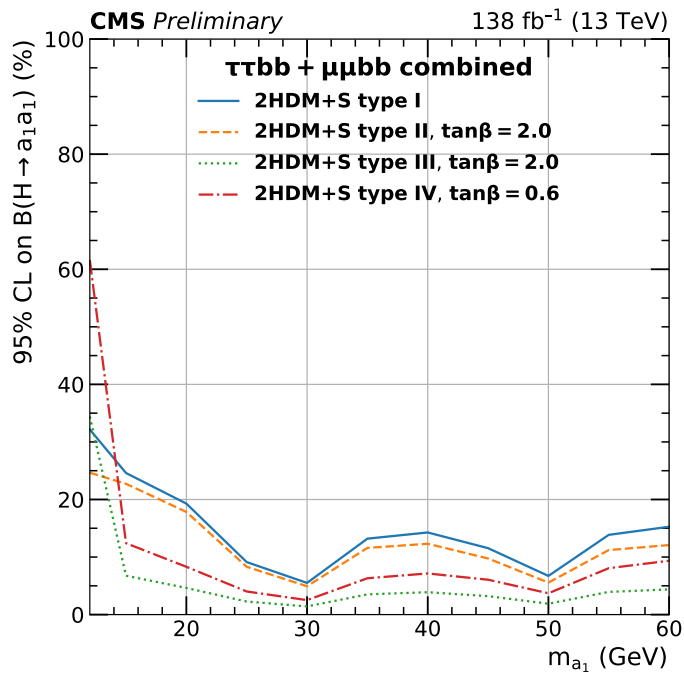


Figure 10.6: Observed 95% CL upper limits on the branching fraction of the 125 GeV Higgs boson to two pseudoscalars,  $B(h \rightarrow aa)$ , in percentages, as a function of the pseudoscalar mass  $m_a$ , in 2HDM+S type I (blue), type II with  $\tan\beta = 2.0$  (orange dashed), type III with  $\tan\beta = 2.0$  (dotted green), and type IV with  $\tan\beta = 0.6$  (red dashed), for the combination of  $bb\mu\mu$  and  $bb\tau\tau$  channels using the full Run 2 integrated luminosity of  $138 \text{ fb}^{-1}$  [45].

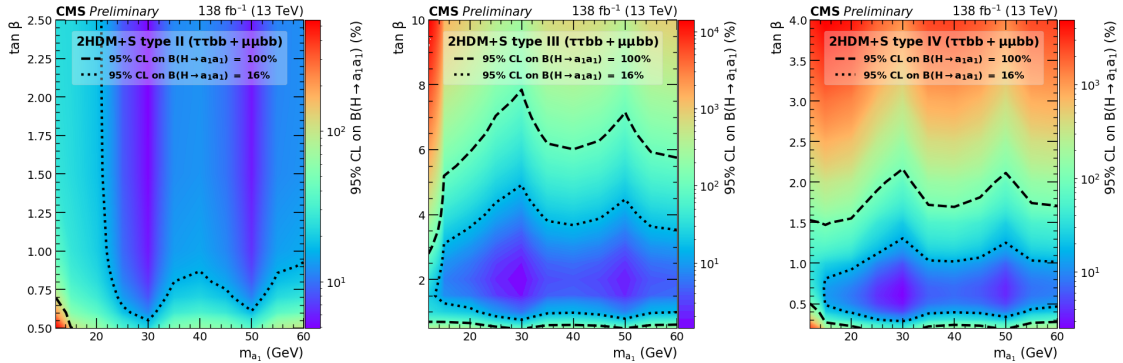


Figure 10.7: Observed 95% CL upper limits on  $\mathcal{B}(h \rightarrow aa)$  in %, for the combination of  $bb\mu\mu$  and  $bb\tau\tau$  channels using the full Run 2 integrated luminosity of  $138 \text{ fb}^{-1}$  for Type II (*left*), Type III (*middle*), and Type IV (*right*) 2HDM+S in the  $\tan \beta$  vs.  $m_a$  phase space. The contours (*dashed black*) correspond to branching fractions of 100% and 16%, where 16% is the combined upper limit on Higgs boson to undetected particle decays from previous Run-2 results. All points inside the contour are allowed within that upper limit. Linear extrapolation has been used between different points on the figures [45].

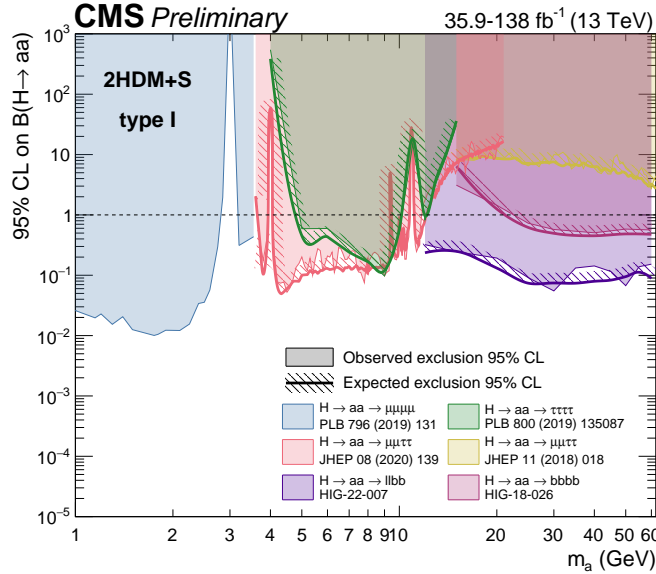


Figure 10.8: Summary plot of current 95% limits on the branching ratio of the 125 GeV Higgs boson to two pseudoscalars, normalized to the Standard Model Higgs production cross-section,  $\frac{\sigma(h)}{\sigma_{SM}} \times B(h \rightarrow aa)$  in the 2HDM+S type I scenario performed with data collected at 13 TeV [102]. Results from different final states studied at CMS are overlaid on this figure:  $\mu\mu\mu\mu$  (blue),  $\tau\tau\tau\tau$  (green), boosted  $2\mu 2\tau$  (red), resolved  $2\mu 2\tau$  (yellow),  $bbbb$  (magenta), and the combined result for  $\ell\ell bb$  ( $\ell = \mu, \tau$ ) (purple).

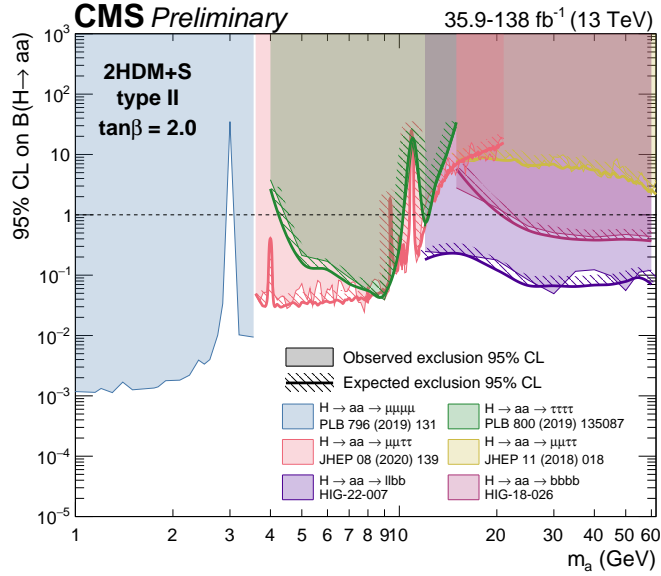


Figure 10.9: Summary plot of current observed and expected 95% CL limits on the branching ratio of the 125 GeV Higgs boson to two pseudoscalars, normalized to the Standard Model Higgs production cross-section,  $\frac{\sigma(h)}{\sigma_{SM}} \times B(h \rightarrow aa)$ , in the 2HDM+S type II scenario with  $\tan \beta = 2.0$ , obtained at CMS with data collected at 13 TeV [102]. Results from different final states studied at CMS are overlaid on this figure:  $\mu\mu\mu\mu$  (blue),  $\tau\tau\tau\tau$  (green), boosted  $2\mu 2\tau$  (red), resolved  $2\mu 2\tau$  (yellow),  $bbbb$  (magenta), and the combined result for  $\ell\ell bb$  ( $\ell = \mu, \tau$ ) (purple).

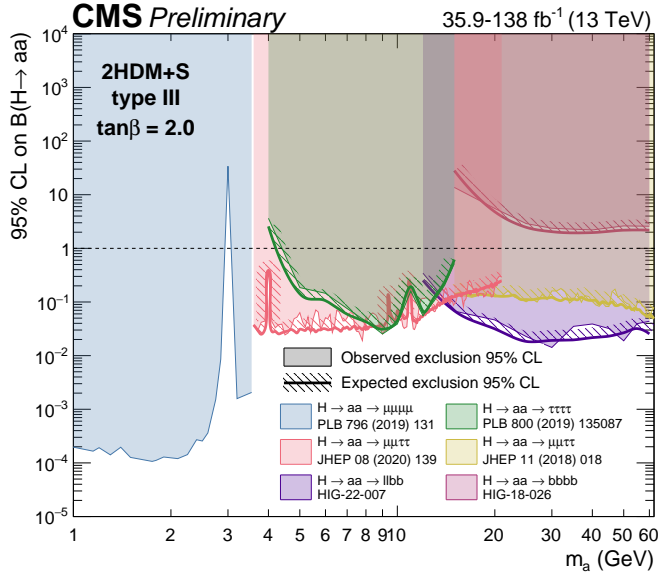


Figure 10.10: Summary plot of current observed and expected 95% CL limits on the branching ratio of the 125 GeV Higgs boson to two pseudoscalars, normalized to the Standard Model Higgs production cross section,  $\frac{\sigma(h)}{\sigma_{SM}} \times B(h \rightarrow aa)$  in the 2HDM+S type-III scenario with  $\tan \beta = 2.0$ , obtained at CMS with data collected at 13 TeV [102]. Results from different final states studied at CMS are overlaid on this figure:  $\mu\mu\mu\mu$  (blue),  $\tau\tau\tau\tau$  (green), boosted  $2\mu 2\tau$  (red), resolved  $2\mu 2\tau$  (yellow),  $bbbb$  (magenta), and the combined result for  $\ell\ell bb$  ( $\ell = \mu, \tau$ ) (purple).

<sup>2415</sup> **Chapter 11**

<sup>2416</sup> **Asymmetric exotic Higgs decays**

<sup>2417</sup> This chapter presents progress towards a search for exotic Higgs decays to two light  
<sup>2418</sup> scalars with unequal mass ( $h \rightarrow a_1 a_2$ ) final states with bottom quarks and  $\tau$  leptons,  
<sup>2419</sup> with plans to interpret the results in the context of Two Real Singlet Models (TRSMs),  
<sup>2420</sup> described in Section 1.5. Compared to the symmetric decay scenario  $h \rightarrow aa$  which  
<sup>2421</sup> has been studied in multiple final states at CMS with stringent limits set on the  
<sup>2422</sup> various 2HDM+S scenarios, this asymmetric decay scenario has not been directly  
<sup>2423</sup> searched for at the CMS experiment. Section 11.1 lists the mass hypotheses of the  
<sup>2424</sup> new particles  $a_1$  and  $a_2$  that will be studied. Section 11.2 describes the studies on  
<sup>2425</sup> which channels the analysis will be carried out in. Section 11.3 shows the control  
<sup>2426</sup> plots produced using the analysis framework that will be used for this analysis.

<sup>2427</sup> **11.1 Signal masses**

<sup>2428</sup> As discussed in Section 1.5,  $h \rightarrow a_1 a_2$  can result in a “cascade” decay if one of the  
<sup>2429</sup> scalars,  $a_2$  is sufficiently heavy ( $m_{a_2} > 2m_{a_1}$ ). The “non-cascade” case is where the  
<sup>2430</sup> light scalars decay directly to Standard Model particles.

<sup>2431</sup> The mass hypotheses (mass points) ( $m_{a_1}, m_{a_2}$ ) studied here are:

- *Cascade mass points:* (15, 30), (15, 40), (15, 50), (15, 60), (15, 70), (15, 80), (15, 90), (15, 100), (15, 110), (20, 40), (20, 50), (20, 60), (20, 70), (20, 80), (20, 90), (20, 100), (30, 60), (30, 70), (30, 80), and (30, 90) GeV
- *Non-cascade mass points:* (15, 20), (15, 30), (20, 30), (20, 40), (30, 40), (30, 50), (30, 60), (40, 50), (40, 60), (40, 70), (40, 80), (50, 60), and (50, 70) GeV

Samples were produced using the MadGraph5\_aMCatNLO event generator, for each signal mass point in the gluon-gluon fusion (ggF) and vector boson fusion (VBF) production modes of the 125 GeV Higgs boson. In the sample generation, the decays of  $a$  to Standard Model particles were specified to be decays to bottom quarks or  $\tau$  leptons.

## 11.2 Cascade scenario signal studies

Studies of the signal phenomenology in the cascade scenario were performed to determine the viability of the  $4b2\tau$  and/or  $2b4\tau$  channels.

Cross sections and branching fractions of the  $4b2\tau$  and  $2b4\tau$  final states were compared using cross-section predictions provided by the authors of [7]. For an example mass point  $m_{a_2} = 80$  GeV,  $m_{a_1} = 30$  GeV, the branching fractions to  $4b2\tau$  is ten times larger than  $2b4\tau$ :  $B(h \rightarrow a_1 a_2 \rightarrow 3a_1 \rightarrow 4b2\tau) = 0.00857$ , vs.  $B(h \rightarrow a_1 a_2 \rightarrow 3a_1 \rightarrow 2b4\tau) = 0.00068$ . The  $4b2\tau$  final state is chosen for this analysis.

In general the four b-flavor jets have low  $p_T$  at generator level, as illustrated for example mass points (100, 15) GeV and (40, 20) GeV in Fig. 11.1. The  $p_T$  distribution of the sub-leading jet peaks at an energy below 20 GeV, with the third and fourth jets tending to have even softer energies.

An event category with three or more b-tag jets was determined to be infeasible due to low statistics in this category, due to the difficulties in reconstructing the third

2457 and fourth b-flavor jets which have very low transverse momenta  $p_T$ . Event categories  
 2458 with exactly 1 b-tag jet and  $\geq 2$  b-tag jets will be used.

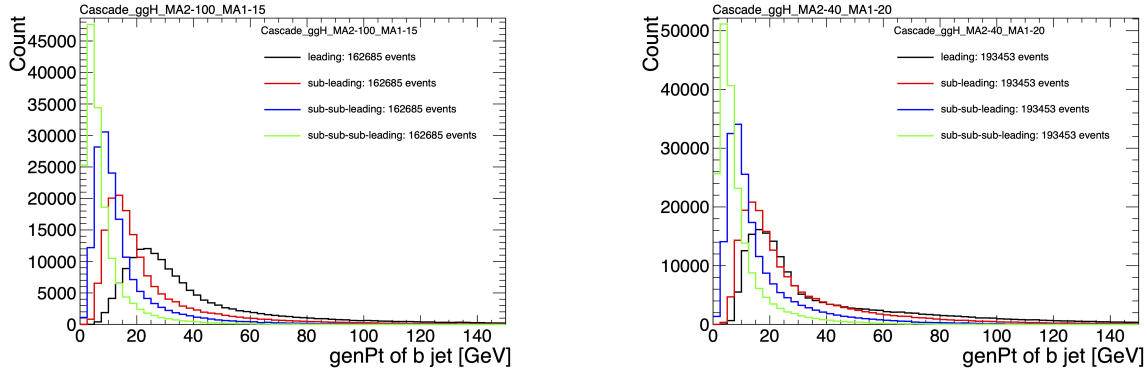


Figure 11.1: Generator-level b-flavor jet transverse momenta  $p_T$ , for  $h \rightarrow a_1 a_2$  cascade scenario in the  $4b2\tau$  final state, for mass hypotheses  $(m_{a_1}, m_{a_2}) = (100, 15)$  GeV (*left*) and  $(40, 20)$  GeV (*right*). In each plot the generator-level  $p_T$  of the leading (*black*), sub-leading (*red*), third (*blue*), and fourth (*light green*) are overlaid.

2459 In the  $4b2\tau$  final state, the possibility of the leading and sub-leading b-tag jets  
 2460 being sufficiently close in  $\Delta R$  to require boosted jet reconstruction techniques was  
 2461 explored. In the  $4b2\tau$  case, the two b-flavor-jets in the generated event that were  
 2462 spatially closest in  $\Delta R$  were considered as one object. This two b-flavor jet object was  
 2463 spatially matched in  $\Delta R$  to the jets reconstructed with the standard AK4 algorithm  
 2464 which uses a cone size of  $\Delta R = 0.4$ . The quality of the  $p_T$  resolution (computed as  
 2465  $(p_{T,\text{reconstructed}} - p_{T,\text{gen}})/p_{T,\text{gen}}$ ) and closeness in distance  $\Delta R$  of the reconstructed jet  
 2466 to the nearest generator-level jets, was seen to depend on the absolute and relative  
 2467 masses of the light scalars. The best (worst) performance occurred in samples with  
 2468 large (small) mass differences between the heavier scalar  $a_2$  and the lighter scalar  $a_1$ ,  
 2469 as illustrated for the mass hypotheses  $(m_{a_1}, m_{a_2})$  (100, 15) GeV and (40, 20) GeV in  
 2470 Fig. 11.2.

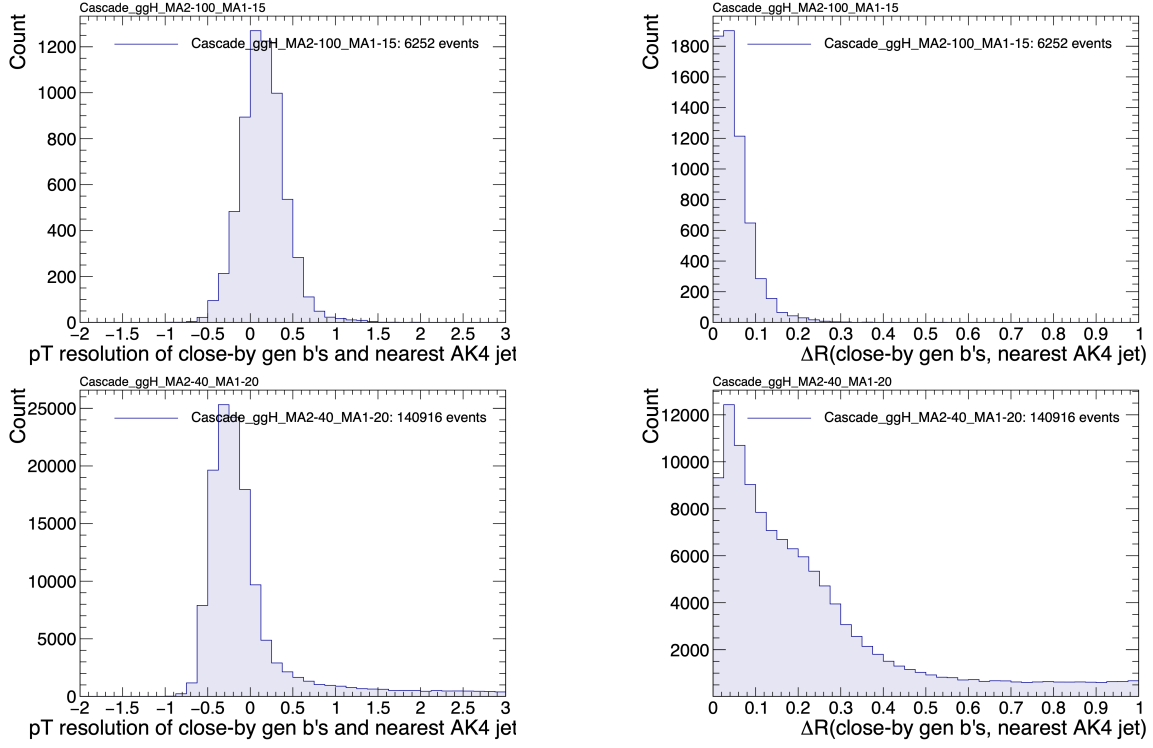


Figure 11.2: Distributions (arbitrary units) of transverse momentum  $p_T$  resolution and  $\Delta R$  between the two closest generator-level  $b$  jets, treated as one object, and the nearest reconstructed AK4 jet, for two different  $h \rightarrow a_1 a_2$  mass hypotheses ( $m_{a_1}, m_{a_2}$ ) = (100, 15) GeV (top left, top right) and (40, 20) GeV (bottom left, bottom right) in the ggH production of the 125 GeV  $h$ . In the (40, 20) GeV mass point, the longer  $p_T$  resolution tail (bottom left) indicates that the reconstructed jet underestimates the generator  $b$ -flavor jets' energy, and the significant fraction of events with larger  $\Delta R$  values (bottom right) indicate worse matching.

### 11.3 Current control plots for $\mu\tau_h$ channel

The  $\tau\tau$  states for the  $h \rightarrow a_1 a_2$  to  $4b2\tau$  analysis will be similar to those studied in  $h \rightarrow aa \rightarrow bb\tau\tau$ . For the  $\mu\tau_h$  channel, histograms of the key kinematic variables are made for data and the sum of the expected backgrounds, which are estimated from Monte Carlo samples, embedded samples, and the data-driven method for estimating jets faking  $\tau_h$  as described in Chapter 7. Nominal values of the scale factors and event reweighting are applied, as described in Chapter ???. The errors shown in the figures only include statistical errors and only several of the full set of systematic errors (only those associated with the lepton energy scales and  $\tau_h$  identification efficiency,

2480 described in Sections 5.3.1, 5.3.2, and 5.3.4).

2481 The  $p_T$ ,  $\eta$ , and  $\phi$  of the leading muon and hadronic tau  $\tau_h$ , and the di-tau visible  
2482 mass  $m_{\text{vis}}$  and momentum  $p_{T,\text{vis}}$ , are shown in Fig. 11.3. The  $p_T$ ,  $\eta$ , and  $\phi$  of the the  
2483 leading and sub-leading b-tag jets, and the missing transverse energy magnitude and  
2484 azimuthal direction, are shown in Fig. 11.4.

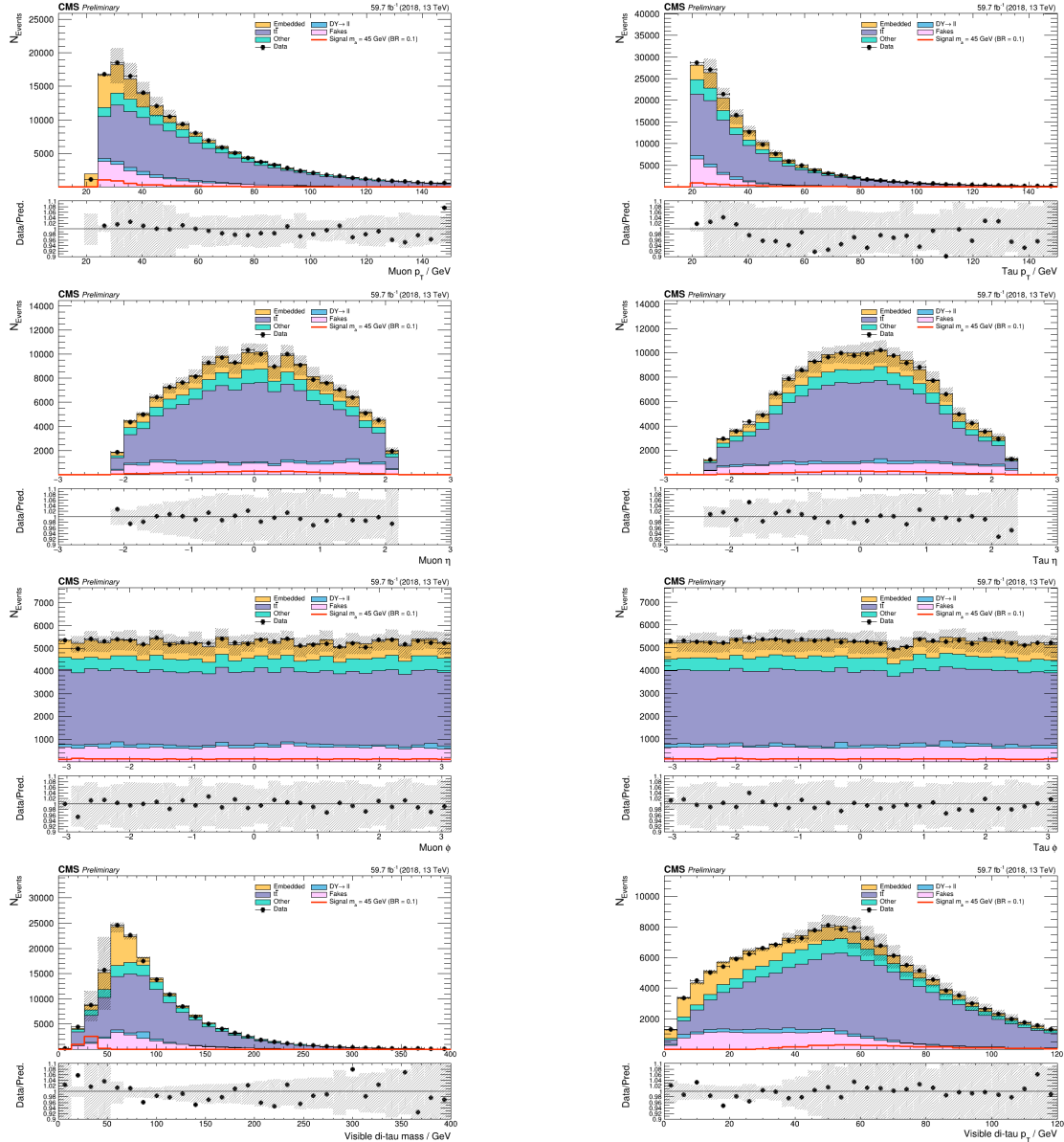


Figure 11.3: Kinematic properties of the leading muon and  $\tau_h$  in the  $\mu\tau_h$  channel:  $p_T$  (top row),  $\eta$  (second row), and  $\phi$  (third row). The visible 4-momenta of the muon and  $\tau_h$  are summed, giving the visible di-tau mass  $m_{\text{vis}}$  and transverse momentum  $p_{T,\text{vis}}$ . The errors shown in the figures only include statistical errors and only several of the full set of systematic errors (only those associated with the lepton energy scales and  $\tau_h$  identification efficiency).

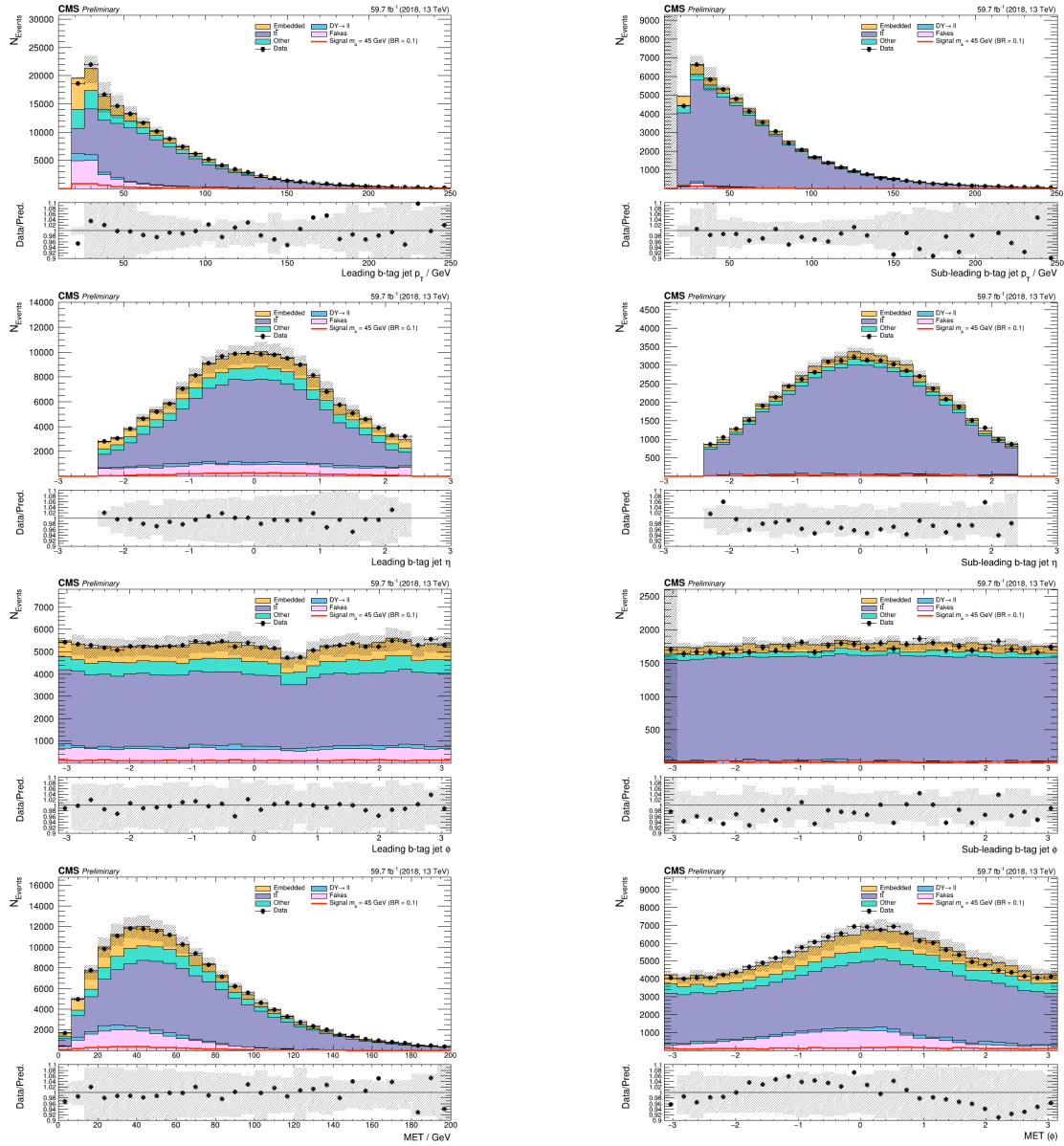


Figure 11.4: Kinematic properties of the leading and sub-leading b-tag jets in the  $\mu\tau_h$  final state: jet  $p_T$  (*top row*),  $\eta$  (*second row*),  $\phi$  (*third row*), as well as the missing transverse energy magnitude and azimuthal direction (*bottom row*). The errors shown in the figures only include statistical errors and only several of the full set of systematic errors (only those associated with the lepton energy scales and  $\tau_h$  identification efficiency).

2485

# Chapter 12

2486

## Conclusion and outlook

2487 With the discovery of a Higgs boson with mass 125 GeV at the LHC in 2012, the LHC  
2488 and CMS physics program has evolved to include the precise characterization of the  
2489 125 GeV Higgs boson and searching for evidence of additional Higgs particles in an  
2490 extended Higgs sector. This thesis presents a direct search at CMS for exotic decays  
2491 of the Higgs boson with mass 125 GeV in data collected in the years 2016-2018 in  
2492 proton-proton collisions at center-of-mass energy 13 TeV, to two light neutral scalar  
2493 particles that decay to two bottom quarks and two tau leptons ( $h \rightarrow aa \rightarrow bb\tau\tau$ ). The  
2494 results are combined with another search that was performed in the  $h \rightarrow aa \rightarrow bb\mu\mu$   
2495 final state, giving the most stringent limits to date for theories with Two Higgs  
2496 Doublet Models extended with a singlet scalar (2HDM+S), for pseudoscalar masses  
2497  $m_a$  ranging from 15 GeV to 60 GeV, in a number of 2HDM+S scenarios such as type  
2498 II and III with  $\tan\beta = 2.0$ .

2499 As the rich physics program of CMS has set stringent limits on the exotic decay  
2500  $h \rightarrow aa$ , we turn our attention to direct searches for decays to light neutral scalars  
2501 with potentially unequal mass,  $h \rightarrow a_1a_2$ , which has not been performed at CMS  
2502 to date. Preliminary studies on  $h \rightarrow a_1a_2$  signals in the Two Real Singlet Model  
2503 (TRSM) are shown, and work is ongoing to develop the analysis for  $h \rightarrow a_1a_2$  in final

2504 states with bottom quarks and tau leptons.

2505 To ensure the continued performance of the CMS detector and to enhance its  
2506 data-taking capabilities in the intense pile-up conditions of the Phase-2 upgrade of  
2507 the High-Luminosity LHC, upgrades of the Level-1 Trigger are paramount for filtering  
2508 the increased data rate of the HL-LHC. This thesis presents work on the standalone  
2509 barrel calorimeter algorithm for reconstructing and identifying electron and photon  
2510 candidates, using high granularity crystal-level information from the ECAL subdetec-  
2511 tor. For Phase-2, the increase in the granularity of information sent from the electro-  
2512 magnetic calorimeter to the Level-1 trigger, from energy sums over towers (which are  
2513  $5 \times 5$  in crystals) to crystal-level information, allows for the implementation of a more  
2514 sophisticated clustering algorithm that can exploit the fact that genuine electrons  
2515 and photons tend to leave energies concentrated a  $3 \times 5$  window in crystals, and use  
2516 shape and isolation information to distinguish genuine electrons and photons from  
2517 noise. Electrons and photons are key to characterizing Standard Model processes and  
2518 performing searches for new physics, and this represents one of the many upgrades of  
2519 the CMS detector in preparation for Phase-2. With the ongoing Run-3 data collecting  
2520 period, and wealth of ongoing and scheduled upgrades, there remains an abundance  
2521 of directions for detector development and physics at CMS heading into Phase-2 of  
2522 the LHC.

2523

# Bibliography

- 2524 [1] Paul H. Frampton. Journeys Beyond the Standard Model. 54(1):52–  
2525 52. ISSN 0031-9228. doi: 10.1063/1.1349615. URL <https://doi.org/10.1063/1.1349615>. eprint: [https://pubs.aip.org/physicstoday/article-pdf/54/1/52/11109432/52\\_1\\_online.pdf](https://pubs.aip.org/physicstoday/article-pdf/54/1/52/11109432/52_1_online.pdf).
- 2526
- 2527
- 2528 [2] Meinard Kuhlmann. Quantum Field Theory. In Edward N. Zalta and Uri Nodelman, editors, *The Stanford Encyclopedia of Philosophy*. Metaphysics Research  
2529 Lab, Stanford University, Summer 2023 edition, 2023.
- 2530
- 2531 [3] Steven Weinberg. The Making of the Standard Model. *Eur. Phys. J. C*, 34:  
2532 5–13, 2004. URL <https://cds.cern.ch/record/799984>.
- 2533
- 2534 [4] Christopher G. Tully. *Elementary Particle Physics in a Nutshell*. Princeton  
2535 University Press, Princeton, 2012. ISBN 9781400839353. doi: doi:10.1515/9781400839353. URL <https://doi.org/10.1515/9781400839353>.
- 2536
- 2537 [5] John Ellis. Higgs Physics. In *2013 European School of High-Energy Physics*,  
pages 117–168, 2015. doi: 10.5170/CERN-2015-004.117.
- 2538
- 2539 [6] David Curtin, Rouven Essig, Stefania Gori, and Others. Exotic decays of the 125  
GeV Higgs boson. *Phys. Rev. D*, 90:075004, Oct 2014. doi: 10.1103/PhysRevD.90.075004. URL <https://link.aps.org/doi/10.1103/PhysRevD.90.075004>.
- 2540
- 2541 [7] Tania Robens, Tim Stefański, and Jonas Wittbrodt. Two-real-scalar-singlet

- extension of the SM: LHC phenomenology and benchmark scenarios. *Eur. Phys. J. C*, 80(2):151, 2020. doi: 10.1140/epjc/s10052-020-7655-x.
- [8] CERN. The history of CERN, 2024. URL <https://timeline.web.cern.ch/timeline-header/89>.
- [9] R. Schmidt. Accelerator physics and technology of the LHC. In *ROXIE: Routine for the Optimizazation of Magnet X-Sections, Inverse Field Calculation and Coil End Design*, pages 7–17, 1998.
- [10] J. Vollaire et al. *Linac4 design report*, volume 6/2020 of *CERN Yellow Reports: Monographs*. CERN, Geneva, 9 2020. ISBN 978-92-9083-579-0, 978-92-9083-580-6. doi: 10.23731/CYRM-2020-006.
- [11] Antonella Del Rosso. Aerial view of the LHC and the four major experiments. 2017. URL <https://cds.cern.ch/record/2253966>. General Photo.
- [12] ATLAS Collaboration. ATLAS: Detector and physics performance technical design report. Volume 1. 5 1999.
- [13] CMS Collaboration. CMS Physics: Technical Design Report Volume 1: Detector Performance and Software. 2006.
- [14] L Musa. Conceptual Design Report for the Upgrade of the ALICE ITS. Technical report, CERN, Geneva, 2012. URL <https://cds.cern.ch/record/1431539>.
- [15] S. Amato et al. LHCb technical proposal: A Large Hadron Collider Beauty Experiment for Precision Measurements of CP Violation and Rare Decays. 2 1998.
- [16] Werner Herr and B Muratori. Concept of luminosity. 2006. doi: 10.5170/CERN-2006-002.361. URL <https://cds.cern.ch/record/941318>.

- 2566 [17] Olivier S. Brning and Frank Zimmerman. Parameter space for the LHC lu-  
2567 minosity upgrade. ISBN 978-3-95450-115-1. URL <https://accelconf.web.cern.ch/IPAC2012/papers/moppc005.pdf>.
- 2568
- 2569 [18] CMS Collaboration. Pileup mitigation at CMS in 13 TeV data. *JINST*, 15(09):  
2570 P09018, 2020. doi: 10.1088/1748-0221/15/09/P09018.
- 2571 [19] CMS Collaboration. Measurement of the inelastic proton-proton cross section  
2572 at  $\sqrt{s} = 13$  TeV. *JHEP*, 07:161, 2018. doi: 10.1007/JHEP07(2018)161.
- 2573 [20] CMS Collaboration. High-Luminosity Large Hadron Collider (HL-LHC): Tech-  
2574 nical design report. 10/2020, 12 2020. doi: 10.23731/CYRM-2020-0010.
- 2575 [21] CMS Collaboration. The CMS Experiment at the CERN LHC. *JINST*, 3:  
2576 S08004, 2008. doi: 10.1088/1748-0221/3/08/S08004.
- 2577 [22] CMS Collaboration. Particle-flow reconstruction and global event description  
2578 with the CMS detector. *JINST*, 12(10):P10003, 2017. doi: 10.1088/1748-0221/  
2579 12/10/P10003.
- 2580 [23] V Karimki, M Mannelli, P Siegrist, H Breuker, A Caner, R Castaldi, K Freudens-  
2581 reich, G Hall, R Horisberger, M Huhtinen, and A Cattai. *The CMS tracker sys-  
2582 tem project: Technical Design Report*. Technical design report. CMS. CERN,  
2583 Geneva, 1997. URL <https://cds.cern.ch/record/368412>.
- 2584 [24] The Phase-2 Upgrade of the CMS Tracker. Technical report, CERN, Geneva,  
2585 2017. URL <https://cds.cern.ch/record/2272264>.
- 2586 [25] CMS Collaboration. CMS Technical Design Report for the Pixel Detector Up-  
2587 grade. 9 2012. doi: 10.2172/1151650.
- 2588 [26] R. L. Workman and Others. Review of particle physics. 2022:083C01. doi:  
2589 10.1093/ptep/ptac097.

- 2590 [27] CMS Technical Design Report for the Phase 1 Upgrade of the Hadron Calorimeter. 9 2012. doi: 10.2172/1151651.
- 2591
- 2592 [28] CMS Technical Design Report for the Level-1 Trigger Upgrade. 6 2013.
- 2593
- 2594 [29] S. Dasu et al. CMS. The TriDAS project. Technical design report, vol. 1: The trigger systems. 12 2000.
- 2595
- 2596 [30] Alex Tapper. The CMS Level-1 Trigger for LHC Run II. *PoS*, ICHEP2016:242, 2016. doi: 10.22323/1.282.0242.
- 2597
- 2598 [31] A. Zabi, F. Beaudette, L. Cadamuro, O. Davignon, T. Romantneau, T. Strebler, M. Cepeda, J.B. Sauvan, N. Wardle, R. Aggleton, F. Ball, J. Brooke, D. Newbold, S. Paramesvaran, D. Smith, J. Taylor, C. Foudas, M. Baber, A. Bundred, S. Breeze, M. Citron, A. Elwood, G. Hall, G. Iles, C. Laner, B. Penning, A. Rose, A. Shtiplityski, A. Tapper, I. Ojalvo, T. Durkin, K. Harder, S. Harper, C. Shepherd-Themistocleous, A. Thea, T. Williams, S. Dasu, L. Dodd, R. Forbes, T. Gorski, P. Klabbers, A. Levine, T. Ruggles, N. Smith, W. Smith, A. Svetek, J. Tikalsky, and M. Vicente. The cms level-1 calorimeter trigger for the lhc run ii. *Journal of Instrumentation*, 12(01):C01065, jan 2017. doi: 10.1088/1748-0221/12/01/C01065. URL <https://dx.doi.org/10.1088/1748-0221/12/01/C01065>.
- 2601
- 2602
- 2603
- 2604
- 2605
- 2606
- 2607
- 2608 [32] P. Klabbers et al. CMS level-1 upgrade calorimeter trigger prototype development. *JINST*, 8:C02013, 2013. doi: 10.1088/1748-0221/8/02/C02013.
- 2609
- 2610 [33] CMS Collaboration. The Phase-2 Upgrade of the CMS Data Acquisition and High Level Trigger. Technical report, CERN, Geneva, 2021. URL <https://cds.cern.ch/record/2759072>. This is the final version of the document, approved by the LHCC.
- 2611
- 2612
- 2613

- 2614 [34] C. Foudas. The CMS Level-1 Trigger at LHC and Super-LHC. In *34th Inter-*  
2615 *national Conference on High Energy Physics*, 10 2008.
- 2616 [35] CMS Software Guide. High Level Trigger (TWiki), 2024. URL <https://twiki.cern.ch/twiki/bin/view/CMSPublic/SWGuideHighLevelTrigger>.
- 2617  
2618 [36] The Worldwide LHC Computing Grid. 2012. URL <https://cds.cern.ch/record/1997398>.
- 2619  
2620 [37] Douglas Thain, Todd Tannenbaum, and Miron Livny. Distributed computing  
2621 in practice: the Condor experience. *Concurrency and Computation: Practice*  
2622 and *Experience*, 17(2-4):323–356, 2005. doi: <https://doi.org/10.1002/cpe.938>.  
2623 URL <https://onlinelibrary.wiley.com/doi/abs/10.1002/cpe.938>.
- 2624 [38] Alexandre Zabi, Jeffrey Wayne Berryhill, Emmanuelle Perez, and Alexander D.  
2625 Tapper. The Phase-2 Upgrade of the CMS Level-1 Trigger. 2020.
- 2626 [39] Technical proposal for a MIP timing detector in the CMS experiment Phase 2  
2627 upgrade. Technical report, CERN, Geneva, 2017. URL <https://cds.cern.ch/record/2296612>.
- 2628  
2629 [40] CMS Collaboration. Search for exotic decays of the Higgs boson to a pair of  
2630 pseudoscalars in the  $\mu\mu bb$  and  $\tau\tau bb$  final states. *European Physical Journal C*,  
2631 2 2024.
- 2632 [41] CMS Collaboration. CMS luminosity measurement for the 2016 data-taking  
2633 period. CMS Physics Analysis Summary CMS-PAS-LUM-17-001, 2017. URL  
2634 <https://cds.cern.ch/record/2257069>.
- 2635 [42] CMS Collaboration. CMS luminosity measurement for the 2017 data-taking  
2636 period at  $\sqrt{s} = 13$  TeV. CMS Physics Analysis Summary CMS-PAS-LUM-17-  
2637 004, 2018. URL <https://cds.cern.ch/record/2621960>.

- 2638 [43] CMS Collaboration. CMS luminosity measurement for the 2018 data-taking  
2639 period at  $\sqrt{s} = 13$  TeV. CMS Physics Analysis Summary CMS-PAS-LUM-18-  
2640 002, 2019. URL <https://cds.cern.ch/record/2676164>.
- 2641 [44] CMS LUMI Group. CMS Luminosity Public Results (TWiki), 2024. URL  
2642 <https://twiki.cern.ch/twiki/bin/view/CMSPublic/LumiPublicResults>.
- 2643 [45] Cécile Caillol, Pallabi Das, Sridhara Dasu, Pieter Everaerts, Stephanie Kwan,  
2644 Isobel Ojalvo, and Ho-Fung Tsoi. CMS AN-20-213 (internal): Search for an  
2645 exotic decay of the 125 GeV Higgs boson to light pseudoscalars, with a pair of  
2646 b jets and a pair of tau leptons in the final state, 2020.
- 2647 [46] J. Alwall, R. Frederix, S. Frixione, et al. The automated computation of tree-  
2648 level and next-to-leading order differential cross sections, and their matching  
2649 to parton shower simulations. *Journal of High Energy Physics*, 2014(7), July  
2650 2014. ISSN 1029-8479. doi: 10.1007/jhep07(2014)079. URL [http://dx.doi.org/10.1007/JHEP07\(2014\)079](http://dx.doi.org/10.1007/JHEP07(2014)079).
- 2652 [47] R. Frederix, S. Frixione, V. Hirschi, et al. The automation of next-to-leading  
2653 order electroweak calculations. *Journal of High Energy Physics*, 2018(7), July  
2654 2018. ISSN 1029-8479. doi: 10.1007/jhep07(2018)185. URL [http://dx.doi.org/10.1007/JHEP07\(2018\)185](http://dx.doi.org/10.1007/JHEP07(2018)185).
- 2656 [48] S. Agostinelli, J. Allison, K. Amako, et al. Geant4 - a simulation toolkit. 506(3):  
2657 250–303. ISSN 0168-9002. doi: 10.1016/S0168-9002(03)01368-8. URL <https://www.sciencedirect.com/science/article/pii/S0168900203013688>.
- 2659 [49] CMS Collaboration. An embedding technique to determine  $\tau\tau$  backgrounds  
2660 in proton-proton collision data. *JINST*, 14(06):P06032, 2019. doi: 10.1088/  
2661 1748-0221/14/06/P06032.

- 2662 [50] CMS Collaboration. Search for neutral MSSM Higgs bosons decaying to a pair  
2663 of tau leptons in pp collisions. *JHEP*, 10:160, 2014. doi: 10.1007/JHEP10(2014)  
2664 160.
- 2665 [51] CMS Collaboration. Measurements of Higgs boson production in the decay  
2666 channel with a pair of  $\tau$  leptons in proton-proton collisions at  $\sqrt{s} = 13$  TeV.  
2667 *Eur. Phys. J. C*, 83(7):562, 2023. doi: 10.1140/epjc/s10052-023-11452-8.
- 2668 [52] CMS Collaboration. Reconstruction and identification of tau lepton decays to  
2669 hadrons and tau neutrinos at CMS. *Journal of Instrumentation*, 11(01):P01019–  
2670 P01019, January 2016. ISSN 1748-0221. doi: 10.1088/1748-0221/11/01/p01019.  
2671 URL <http://dx.doi.org/10.1088/1748-0221/11/01/P01019>.
- 2672 [53] CMS Collaboration. Performance of  $\tau$ -lepton reconstruction and identification  
2673 in CMS. *Journal of Instrumentation*, 7(01):P01001, jan 2012. doi: 10.1088/  
2674 1748-0221/7/01/P01001. URL <https://dx.doi.org/10.1088/1748-0221/7/01/P01001>.
- 2676 [54] CMS Collaboration. Performance of reconstruction and identification of  $\tau$  lep-  
2677 tons decaying to hadrons and  $\nu_\tau$  in pp collisions at  $\sqrt{s} = 13$  TeV. *JINST*, 13  
2678 (10):P10005, 2018. doi: 10.1088/1748-0221/13/10/P10005.
- 2679 [55] CMS Collaboration. Identification of hadronic tau lepton decays using a deep  
2680 neural network. *JINST*, 17:P07023, 2022. doi: 10.1088/1748-0221/17/07/  
2681 P07023.
- 2682 [56] CMS Collaboration. Performance of CMS muon reconstruction in pp collision  
2683 events at  $\sqrt{s} = 7$  TeV. *Journal of Instrumentation*, 7(10):P10002–P10002,  
2684 October 2012. ISSN 1748-0221. doi: 10.1088/1748-0221/7/10/p10002. URL  
2685 <http://dx.doi.org/10.1088/1748-0221/7/10/P10002>.

- 2686 [57] CMS Collaboration. Performance of electron reconstruction and selection with  
2687 the CMS detector in proton-proton collisions at  $\sqrt{s} = 8$  TeV. *Journal of Instru-*  
2688 *mentation*, 10(06):P06005, 2015. doi: 10.1088/1748-0221/10/06/P06005. URL  
2689 <https://dx.doi.org/10.1088/1748-0221/10/06/P06005>.
- 2690 [58] CMS Collaboration. Identification of b-quark jets with the CMS experiment.  
2691 *Journal of Instrumentation*, 8(04):P04013–P04013, April 2013. ISSN 1748-  
2692 0221. doi: 10.1088/1748-0221/8/04/p04013. URL <http://dx.doi.org/10.1088/1748-0221/8/04/P04013>.
- 2694 [59] CMS Collaboration. Pileup Removal Algorithms. Technical report, CERN,  
2695 Geneva, 2014. URL <https://cds.cern.ch/record/1751454>.
- 2696 [60] CMS Collaboration. CMS Phase 1 heavy flavour identification performance and  
2697 developments. 2017. URL <https://cds.cern.ch/record/2263802>.
- 2698 [61] CMS Collaboration. Performance of the DeepJet b tagging algorithm using  
2699  $41.9 \text{ fb}^{-1}$  of data from proton-proton collisions at 13 TeV with Phase 1 CMS  
2700 detector. 2018. URL <https://cds.cern.ch/record/2646773>.
- 2701 [62] Lorenzo Bianchini, John Conway, Evan Klose Friis, and Christian Veelken. Re-  
2702 construction of the Higgs mass in  $H \rightarrow \tau\tau$  Events by Dynamical Likelihood  
2703 techniques. *Journal of Physics: Conference Series*, 513(2):022035, jun 2014.  
2704 doi: 10.1088/1742-6596/513/2/022035. URL <https://dx.doi.org/10.1088/1742-6596/513/2/022035>.
- 2706 [63] CMS Collaboration. Evidence for the 125 GeV Higgs boson decaying to a pair  
2707 of  $\tau$  leptons. *JHEP*, 05:104, 2014. doi: 10.1007/JHEP05(2014)104.
- 2708 [64] CMS Collaboration. Missing transverse energy performance of the CMS detec-  
2709 tor. *JINST*, 6:P09001, 2011. doi: 10.1088/1748-0221/6/09/P09001.

- 2710 [65] Artur Kalinowski. CMS AN-19-032 (internal): Reconstruction of a  $\tau$  pair in-  
2711 variant mass with a simplified likelihood scan, 2019.
- 2712 [66] CMS TAU POG. Tau Physics Object Group: Tau ID Recommendation  
2713 For Run 2, 2024. URL <https://twiki.cern.ch/twiki/bin/view/CMS/TauIDRecommendationForRun2>.
- 2715 [67] CMS MUO POG. Muon Physics Object Group: Recommendations, 2024. URL  
2716 <https://twiki.cern.ch/twiki/bin/view/CMS/MuonPOG>.
- 2717 [68] CMS MUO POG. Muon Physics Object Group: Reference guidelines and results  
2718 for muon momentum scale and resolution in Run II, 2024. URL <https://twiki.cern.ch/twiki/bin/view/CMS/MuonReferenceScaleResolRun2>.
- 2720 [69] CMS HTT working group. Higgs To Tau Tau Working TWiki for the full Run-  
2721 2 legacy analysis, 2024. URL <https://twiki.cern.ch/twiki/bin/view/CMS/HiggsToTauTauWorkingLegacyRun2>.
- 2723 [70] CMS ELE POG. Electron Physics Object Group: Recommenda-  
2724 tions, 2024. URL <https://twiki.cern.ch/twiki/bin/view/CMS/EgammaRunIIRecommendations>.
- 2726 [71] CMS ELE POG. Electron Physics Object Group: Recommendations for  
2727 2016 to 2018 UL, 2024. URL <https://twiki.cern.ch/twiki/bin/view/CMS/EgammaUL2016To2018>.
- 2729 [72] CMS TAU Embedding Group. Tau embedded samples using 2016  
2730 data, 2024. URL <https://twiki.cern.ch/twiki/bin/view/CMS/TauTauEmbeddingSamples2016Legacy>.
- 2732 [73] CMS TAU Embedding Group. Tau embedded samples using 2017

- 2733 data, 2024. URL <https://twiki.cern.ch/twiki/bin/viewauth/CMS/TauTauEmbeddingSamples2017>.
- 2735 [74] CMS TAU Embedding Group. Tau embedded samples using 2018  
2736 data, 2024. URL <https://twiki.cern.ch/twiki/bin/viewauth/CMS/TauTauEmbeddingSamples2018>.
- 2738 [75] Tau Lepton Run 2 Trigger Performance. 2019. URL <https://cds.cern.ch/record/2678958>.
- 2740 [76] CMS Taus High Level Trigger Studies. Tau Lepton Run 2 Trigger Performance  
2741 (CMS DP-2019/012), 2024. URL <https://twiki.cern.ch/twiki/bin/view/CMSPublic/HLTTauAllRun2>.
- 2743 [77] Muon HLT Performance with 2018 Data. 2018. URL <https://cds.cern.ch/record/2627469>.
- 2745 [78] Single and Double Electron Trigger Efficiencies using the full Run 2 dataset.  
2746 2020. URL <https://cds.cern.ch/record/2888577>.
- 2747 [79] Run II Trigger Performance For  $e\mu$  Triggers. 2019. URL <https://cds.cern.ch/record/2687013>.
- 2749 [80] Performance of electron and photon reconstruction in Run 2 with the CMS  
2750 experiment. 2020. URL <https://cds.cern.ch/record/2725004>.
- 2751 [81] CMS Collaboration. Performance of the CMS muon detector and muon recon-  
2752 struction with proton-proton collisions at  $\sqrt{s} = 13$  TeV. *JINST*, 13(06):P06015,  
2753 2018. doi: 10.1088/1748-0221/13/06/P06015.
- 2754 [82] Piet Verwilligen. Muons in the cms high level trigger system. *Nuclear  
2755 and Particle Physics Proceedings*, 273-275:2509–2511, 2016. ISSN 2405-6014.  
2756 doi: <https://doi.org/10.1016/j.nuclphysbps.2015.09.441>. URL <https://www>.

- 2757        [sciencedirect.com/science/article/pii/S240560141500930X](https://www.sciencedirect.com/science/article/pii/S240560141500930X). 37th Inter-  
2758        national Conference on High Energy Physics (ICHEP).
- 2759        [83] Muon tracking performance in the CMS Run-2 Legacy data using the tag-and-  
2760        probe technique. 2020. URL <https://cds.cern.ch/record/2724492>.
- 2761        [84] V.M. Abazov, B. Abbott, M. Abolins, et al. A novel method for modeling  
2762        the recoil in W boson events at hadron colliders. *Nuclear Instruments and*  
2763        *Methods in Physics Research Section A: Accelerators, Spectrometers, Detectors*  
2764        *and Associated Equipment*, 609(2):250–262, 2009. ISSN 0168-9002. doi: <https://doi.org/10.1016/j.nima.2009.08.056>. URL <https://www.sciencedirect.com/science/article/pii/S0168900209016623>.
- 2765        [85] CMS Collaboration. Search for an exotic decay of the Higgs boson to a pair of  
2766        light pseudoscalars in the final state with two b quarks and two  $\tau$  leptons in  
2767        proton-proton collisions at  $\sqrt{s} = 13$  TeV. *Phys. Lett. B*, 785:462, 2018. doi:  
2768        [10.1016/j.physletb.2018.08.057](https://doi.org/10.1016/j.physletb.2018.08.057).
- 2769        [86] CMS LUMI POG. Luminosity Physics Object Group: Recommendations, 2024.  
2770        URL <https://twiki.cern.ch/twiki/bin/view/CMS/TWikiLUM>.
- 2771        [87] The modeling of the top quark  $p_T$  (TWiki), 2024. URL <https://twiki.cern.ch/twiki/bin/view/CMS/TopPtReweighting>.
- 2772        [88] CMS BTV group. Methods to apply b-tagging efficiency scale fac-  
2773        tors (TWiki), 2024. URL <https://twiki.cern.ch/twiki/bin/view/CMS/BTagShapeCalibration>.
- 2774        [89] CMS Collaboration. Jet energy scale and resolution in the CMS experiment in  
2775        pp collisions at 8 TeV. *JINST*, 12(02):P02014, 2017. doi: [10.1088/1748-0221/12/02/P02014](https://doi.org/10.1088/1748-0221/12/02/P02014).

- 2781 [90] Garvita Agarwal. Jet Energy Scale and Resolution Measurements in CMS. *PoS*,  
2782 ICHEP2022:652, 2022. doi: 10.22323/1.414.0652.
- 2783 [91] CMS JERC group. Jet Energy Corrections (TWiki), 2024. URL <https://twiki.cern.ch/twiki/bin/view/CMS/JECDataMC>.
- 2785 [92] CMS JERC group. Jet Energy Resolution (TWiki), 2024. URL <https://twiki.cern.ch/twiki/bin/view/CMS/JetResolution>.
- 2787 [93] CMS MUO POG. Muon Physics Object Group: Baseline muon selections for Run-II, 2024. URL <https://twiki.cern.ch/twiki/bin/view/CMS/SWGuideMuonIdRun2>.
- 2790 [94] CMS ELE POG. Electron Identification Based on Simple Cuts, 2024. URL  
2791 <https://twiki.cern.ch/twiki/bin/view/CMSPublic/EgammaPublicData>.
- 2792 [95] Jose Enrique Palencia Cortezon. Single top quark production at CMS. Technical  
2793 report, CERN, Geneva, 2018. URL <https://cds.cern.ch/record/2640578>.
- 2794 [96] CMS Collaboration. Measurements of the electroweak diboson production cross  
2795 sections in proton-proton collisions at  $\sqrt{s} = 5.02$  TeV using leptonic decays.  
2796 *Phys. Rev. Lett.*, 127(19):191801, 2021. doi: 10.1103/PhysRevLett.127.191801.
- 2797 [97] CMS Collaboration. A portrait of the Higgs boson by the CMS experiment  
2798 ten years after the discovery. *Nature*, 607(7917):60–68, 2022. doi: 10.1038/  
2799 s41586-022-04892-x.
- 2800 [98] CMS JERC group. Jet energy scale uncertainty sources (TWiki), 2024. URL  
2801 <https://twiki.cern.ch/twiki/bin/view/CMS/JECUncertaintySources>.
- 2802 [99] TOP Systematic Uncertainties (Run 2) (TWiki), 2024. URL <https://twiki.cern.ch/twiki/bin/viewauth/CMS/TopSystematics>.

- 2804 [100] Kyle Cranmer. Practical Statistics for the LHC. In *2011 European School of*  
2805 *High-Energy Physics*, pages 267–308, 2014. doi: 10.5170/CERN-2014-003.267.
- 2806 [101] Elham Khazaie, Maryam Zeinali, Hamed Bakhshiansohi, and Abideh Jafari.  
2807 CMS AN-21-058 (internal): Search for exotic decays of the Higgs boson to a  
2808 pair of new light bosons with two muons and two b jets in the final states at  
2809  $\sqrt{s} = 13$  TeV, 2021.
- 2810 [102] CMS Higgs Physics Analysis Group. Summary of 2HDM+S searches at 13 TeV  
2811 (Run 2), 2024. URL <https://twiki.cern.ch/twiki/bin/view/CMSPublic/Summary2HDMSRun2>.